Investigating Corrosion Processes in Ag-Cu Alloys

Written By

Erik Lübke, BSc

Supervised by

Associate Prof. Dipl.-Ing. Dr.techn. Christian Gierl-Mayer

Dipl.-Min. Dr.rer.nat Klaudia Hradil

Perfomed at

X-Ray Center

TU Wien

and

Institute of Chemical Technologies and Analytics

Faculty of Technical Chemistry

TU Wien

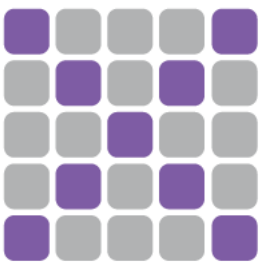

x-ray center

_____ _____

Date Signature

Gewidmet in Gedenken an Siegfried Lübke und Franz Beham

Danksagung

An dieser Stelle möchte ich mich zuerst bei Klaudia Hradil für die Möglichkeit, die letzten 3 Jahre im Röntgenzentrum mitzuarbeiten, bedanken. In dieser Zeit konnte ich nicht nur meine Kompetenzen im Bereich der Röntgenkristallographie aufbauen und die Grundsteine meiner wissenschaftlichen Karriere legen, sondern durfte auch Teil dieser einzigartigen Gemeinschaft sein. Ohne die vielen Ratschläge, genauen Erklärungen und breite Liste an Aufgaben, die ich von Klaudia bekommen habe, wäre ich nicht die Person mit den Fähigkeiten und Möglichkeiten, die ich jetzt bin.

Weiters möchte ich mich bei Werner Artner bedanken, der mich stets bei jeglicher Messaufgabe unterstützt hat und mir die technisch-praktischen Aspekte der Arbeit mit Röntgenstrahlung beigebracht hat. Ohne Werner wäre das Röntgenzentrum und vermutlich die gesamte Forschung mit Röntgenmethode der Fakultät in der jetzigen Form nicht möglich. Jeder, der im XRC messen durfte, sagt das gleiche: „Werner ist der beste auf dieser Uni".

Ich möchte mich auch bei Berthold, Erich und Camilla und allen anderen XRC-Mitarbeiter_innen für die schönen Gespräche im Alltag des Röntgenzentrums, die gemeinsamen Mittagessen und die stets sehr gute Zusammenarbeit bedanken.

Weiters möchte ich mich bei Christian Gierl-Mayer bedanken, der meine Diplomarbeit gemeinsam mit Klaudia betreut hat und mir die Möglichkeit gegeben hat meine Arbeit so schnell wie möglich abzuschließen.

Besonderer Dank gebührt auch Michi, Stefi, und meinen anderen Kommiliton_innen, sowie der Fachschaft Chemie, mit denen das gemeinsame Leid des Studiums in vielen Stunden und Litern an Fermentationsprodukten bestritten und zu der Zeit gemacht wurde, an die man sich als „die gute Zeit" erinnern kann.

Zuletzt möchte ich mich auch bei all denen bedanken die mir mein Studium ermöglicht haben. Meinen Eltern Klaus und Dorothea, bei meinen Großeltern Franz, Edeltraud und Uta, bei meinen "alten" Geschwistern Jolanda, Lina, und denen die im Laufe des Studiums dazu gekommen sind, Raphael, Theodor und Allegra. Die Unterstützung durch meine Familie hat mich immer vorangetrieben, alle Tiefpunkte zu überstehen und nicht aufzugeben.

Ohne die Unterstützung all dieser - und noch viel mehr als hier genannt werden könnten - hätte ich es nicht geschafft an diesen Punkt zu kommen.

Danke!

Abstract

The Vienna Genesis, an artifact produced in the 6th century, is a manuscript written on parchment using silver ink and it has survived to this day. This silver ink corroded and partly damaged the parchment it was written on, threatening to destroy the manuscript. To understand the processes causing this damage, investigations using non-destructive X-ray methods were carried out.

It was attempted to reproduce the observed corrosion while measuring the reactions happening with in-situ powder X-ray diffraction using laboratory instruments. Silver-copper alloys matching the composition of the original inks were prepared in-situ by reducing an oxide-based precursor mixture with hydrogen gas. These alloys were corroded using pressurized air and brine spray at nonambient temperatures and the resulting diffraction patterns were refined using the Rietveld method.

While the corrosion products found did not match with the Vienna Genesis, oxygen induced segregation of the alloys above 200 °C was observed. This effect was investigated further by varying the composition of the alloy and corrosive agents as well as including an internal standard to obtain precise data on the lattice parameter of the segregated species.

It was found that in silver-copper alloys, the lattice parameter *a* of the fcc-silver phase increases during the segregation process to a larger value than pure silver. This result was confirmed by the addition of a standard reference material and measurements using parallel beam optics to circumvent the specimen displacement error.

No conclusive explanation for this effect was found, but a higher than predicted oxygen content was measured in segregated samples, which implies oxygen causing the observed lattice change. More research is required to fully explain the observed behaviour and its effects on the physical properties of the segregated material. This might offer new insights into the effects of oxygen induced segregation, which currently limit the application of Ag-Cu alloys as conductors, solders, etc.

Table of Contents

Abstract 7

List of Abbreviations 11

1 Introduction 12

2 Theoretical Background 13

2.1 The Vienna Genesis 13

2.2 Artificially Aged Samples 15

2.2.1 Samples and Measurements 15

2.2.2 Results 16

2.3 Ag-Cu System 18

2.3.1 Phase Diagram 18

2.3.2 Vegard's Law 18

2.3.3 Oxygen Induced Segregation 20

2.4 Non-Ambient Powder XRD 21

2.4.1 X-ray source and beam optics 21

2.4.2 High Temperature / Non-Ambient X-Ray Diffraction 22

2.5 Rietveld Refinement 23

2.5.1 General Information 23

2.5.2 Principle of the Rietveld Method 23

2.5.3 Scattering intensity term 24

2.5.4 Peak profile function 25

2.5.5 Relevance of the Refinements 25

3 Measurement Setup 27

3.1 XRD-Setup 27

3.2 Non-Ambient Setup 28

3.2.1 Reaction Chamber 28

3.2.2 Atmosphere Control 29

3.2.3 Brine spray 29

3.3 Alloy Preparation Route 30
3.4 Corrosion Measurement 32
4 Samples and Measurements 34
4.1 Overview of Measurement Series 34
4.2 Synthesis of Ag_2O 35
4.3 Calibration of Lattice Parameters 35
4.4 Temperature Variation Series 36
4.5 10 w% Copper Alloy 36
4.5.1 Pure Alloy / 10wCu series 36
4.5.2 Oxygen Content Analysis / 10wCu_LECO 37
4.5.3 Samples containing an Internal Standard / 10wCu+Al_2O_3 series 38
4.5.4 Long-Term Experiment /10wCu_Long 39
4.6 1.5 w% Copper Alloy 40
4.6.1 With internal Standard / 1.5wCu+Al_2O_3 Air 40
4.7 Scanning Electron Microscopy (SEM) 41
5 Refinement 42
5.1 Configuration and Refined Parameters 42
5.2 Automation 43
6 Data Analysis 45
6.1 General Information 45
6.2 Calibration 47
6.2.1 Prepared Ag_2O 47
6.2.2 Non-ambient Temperatures 48
6.2.3 Starting Values for Rietveld Refinement 51
6.3 Scanning Electron Microscopy Images 52
6.3.1 Pure Silver Metal 52
6.3.2 Silver Metal with added Alumina 58
6.4 Temperature Variation Series 60

6.5 10 w% Copper Alloys / 10wCu Series 64
6.5.1 10 w% Cu Alloy corroded with Air / 10wCu_Air 64
6.5.2 10 w% Cu Alloy corroded with Air and Brine Spray / 10wCu_NaCl 66
6.5.3 10 w% Cu Alloy corroded with Air after Homogenisation / 10wCu_LECO 69
6.5.4 Sample with added internal Standard corroded with Air / 10wCuAl_2O_3_Air 73
6.5.5 Sample with added internal Standard, Blind Experiment / 10wCuAl_2O_3_Blind 76
6.5.6 Long-Term Experiment / 10wCu_Long 78
6.6 1.5 w% Copper Alloy 80
6.7 Oxygen induced segregation 83
7 Summary 90
8 Conclusion 92
9 Outlook 93
9.1 Reproducing Corrosion Phenomena Observed on the Vienna Genesis 93
9.2 Analysis of the segregated silver species 93
10 List of Figures 95
11 Table of Tables 98
12 References 99

List of Abbreviations

XRD	X-ray diffraction
PXRD	Powder X-ray diffraction
w%	Weight percent
ESD	Estimated Standard Deviation
BBHD	Bragg-Brentano High Definition
DBN	Database number
SEM	Scanning Electron Microscopy
GOF	Goodness of Fit
ppm	parts per million

1 Introduction

Silver-Copper alloys are among the most ancient alloys and have been used by humans since prehistoric times. Thus, they can sometimes be found in ancient artifacts. Depending on the storage conditions and composition, interesting corrosion phenomena can occur in these artifacts. Artifacts of this kind offer incredible insight into the properties and long-term stability of materials produced by humans. The Vienna Genesis, a manuscript produced in the 6th Century, is one of those cases [1].

This book of genesis, which was written with silver ink on dyed parchment, has suffered corrosion damage from the ink. To preserve and restore this artifact a project was started to analyse and restore the parchment as close to its original state as possible. During this project multiple analytic techniques were performed on the Vienna Genesis. Furthermore, experiments were carried out to understand the corrosion processes happening, which is required to prevent them from happening again.

Artificial samples using preparation methods of this period were prepared. These samples were then artificially aged and analysed using modern techniques [2]. To further understand these results, detailed analyses of the Ag-Cu system were needed to understand the corrosion processes happening.

This thesis attempted to reproduce the corrosion processes observed on the original parchment, using understandings acquired from the analyses performed during the restorations of the Vienna Genesis. In order to reproduce the corrosion, in-situ X-ray diffraction experiments were performed with multiple corrosive agents.

During the research performed in this thesis, unexpected phenomena were observed during the corrosion of silver copper alloys. These were investigated methodically to explain the effect observed and its applications in other areas dependant on silver-copper alloys.

2 Theoretical Background

2.1 The Vienna Genesis

This research concerns an artifact called “Vienna Genesis”, which is a manuscript of the biblical book of Genesis, written on purple parchment with silver ink. Its creation was dated to the first half of the 6th century, and it is considered to be the oldest and best-preserved biblical text. In recent years a project to restore the manuscript and improve its longevity was completed, where the original artifact was analysed using modern non-destructive methods [1].

One of the most alarming degradation processes stems from the corrosion of the silver ink used to write the text. In some unknown process the ink slowly destroys the parchment it was written on, which needs to be prevented to preserve the artifact for future generations. This thesis started as part of the project investigating the Vienna Genesis during this restoration and was intended to replicate the corrosion effects observed on the parchment.

Figure 1 shows a scanned sample page of the original parchment. The damage caused by the silver ink is clearly visible. Some areas have holes shaped like the originally written letters, while other areas were lost completely. Interestingly, the illustrations in the genesis did not corrode whatsoever. The damage to the parchment is only observed with the silver ink used to write the text.

During the analysis and restoration of the Vienna Genesis, X-ray diffraction and X-ray fluorescence measurements were performed on the original parchment. This elemental- and phase analysis detected silver chloride AgCl as the main corrosion product of the silver metal in the ink. Additionally, XRF showed a copper impurity in the silver, with a varying copper content of up to 10 w%.

It is assumed that the genesis was originally written in what is Syria today. The routes used for traveling from there to continental Europe in the 6th century involved crossing the sea at some point, where the parchment might have had contact with sea water. For this reason, brine was investigated as a factor in the corrosion.

These preliminary results were used to prepare and age artificial samples of different silver inks and are the topic of chapter 2.2 “Artificially Aged Samples”. The combined results of these studies were used as starting points for this thesis, where further attempts to reproduce the observed corrosion were performed.

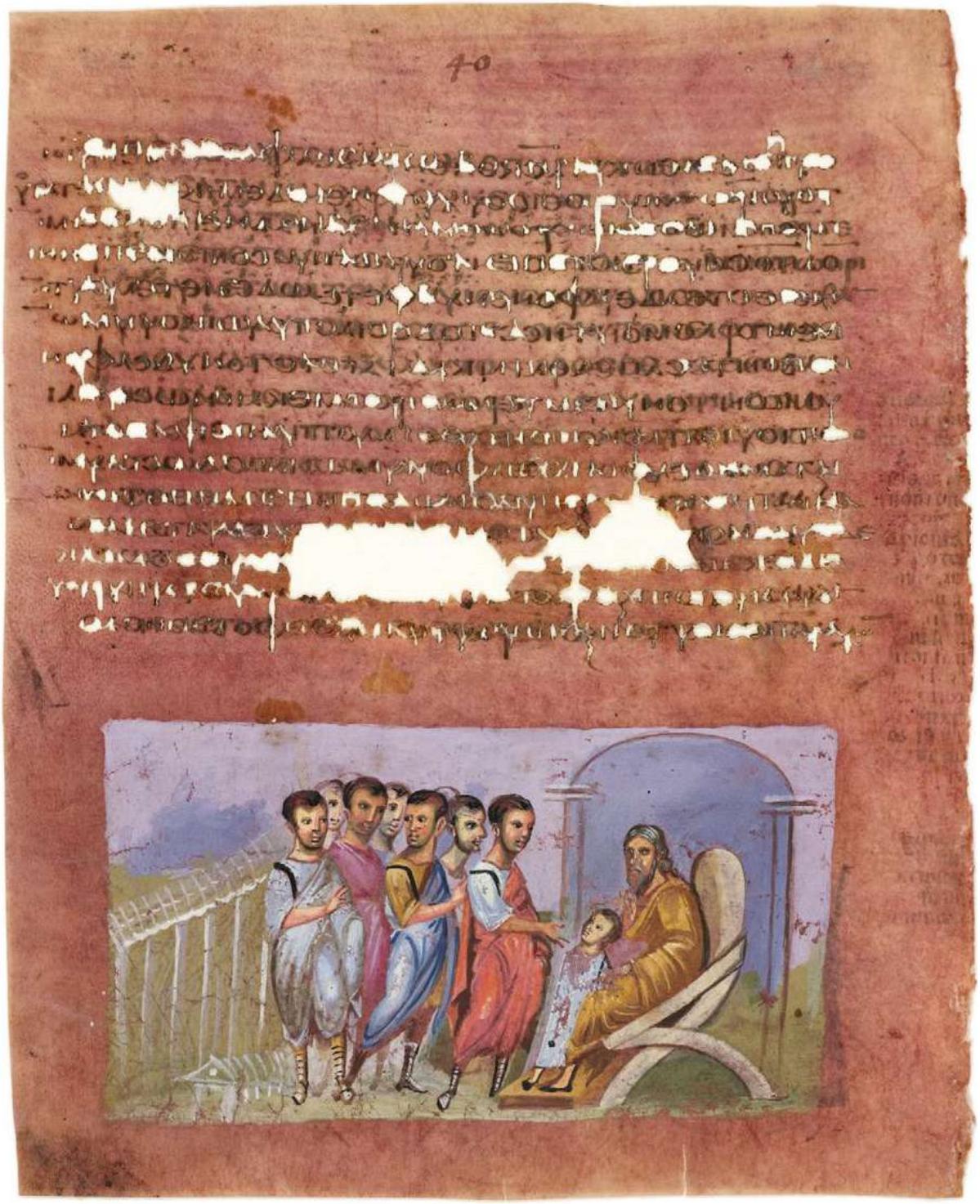

Figure 1: Scan of the original parchment. Folio 20, page 40, which suffered heavy corrosion damage from the silver ink. [1]

Further information about the Vienna Genesis can be found in the open-access publication written about the restoration [1].

2.2 Artificially Aged Samples

2.2.1 Samples and Measurements

In the aforementioned project, one of the main paths of research was the reproduction of ancient silver inks by following recipes of the era. These inks were then written on parchment, which was also prepared and dyed following ancient recipes, and artificially aged by repeated exposure to temperature and humidity over a certain timeframe. More information about the sample preparation and ageing process can be found in the master thesis by Antonia Malissa [2].

The aged samples of the second series of prepared and artificially aged samples were delivered to the X-Ray Center to be analysed by X-Ray Diffraction. An overview of the inks and their ingredients are depicted in Table 1.

Table 1: Ingredients of the silver inks prepared following historic recipes.

Ink name	Ingredients
ST10	Silver shavings, Mercury, Copper(2)acetate, Water
ST11	Leaf silver, Copper(2)acetate, Water
ST12	Leaf silver, Copper(2)acetate, Water, Acacia Gum
ST13	Silver shavings, Vinegar, Sturgeon glue
ST14	Silver shavings, Water, Salpeter, Sturgeon glue

The treatment applied before the ageing process is denoted by the letter on the end of the sample name. Table 2 shows the corresponding processes used.

Table 2: Nomenclature for the treatment applied before the ageing process.

Ink Series	Treatment before ageing
A	unaged
B	untreated
C	Sprayed with saltwater
D	Sprayed with parchment glue containing vinegar

The XRD measurements were performed on a Malvern PANalytical Empyrean diffractometer using a standard Empyrean X-ray tube producing copper-K_α radiation and a standard Bragg-Brentano High-Definition (BBHD) monochromator produced by PANalytical. This was combined with a 10 mm mask, a 1/4 ° divergence slit, a 1 ° anti-scatter slit and a 0.04 rad Soller slit. Single crystal silicon oriented and cut into wafers in the 7 1 1 plane were used as a base on which the parchment samples could be attached while providing low background scattering.

Figure 2 shows the samples after the accelerated ageing process [1]. The samples were mounted on the board in two columns with three samples per column. Every sample was prepared twofold. Starting in the top left, the first three samples are samples ST10B, ST10C and ST10D, with the duplicates mounted directly below. Then the samples of ST11 are mounted in the next row. This pattern was continued over the entire board.

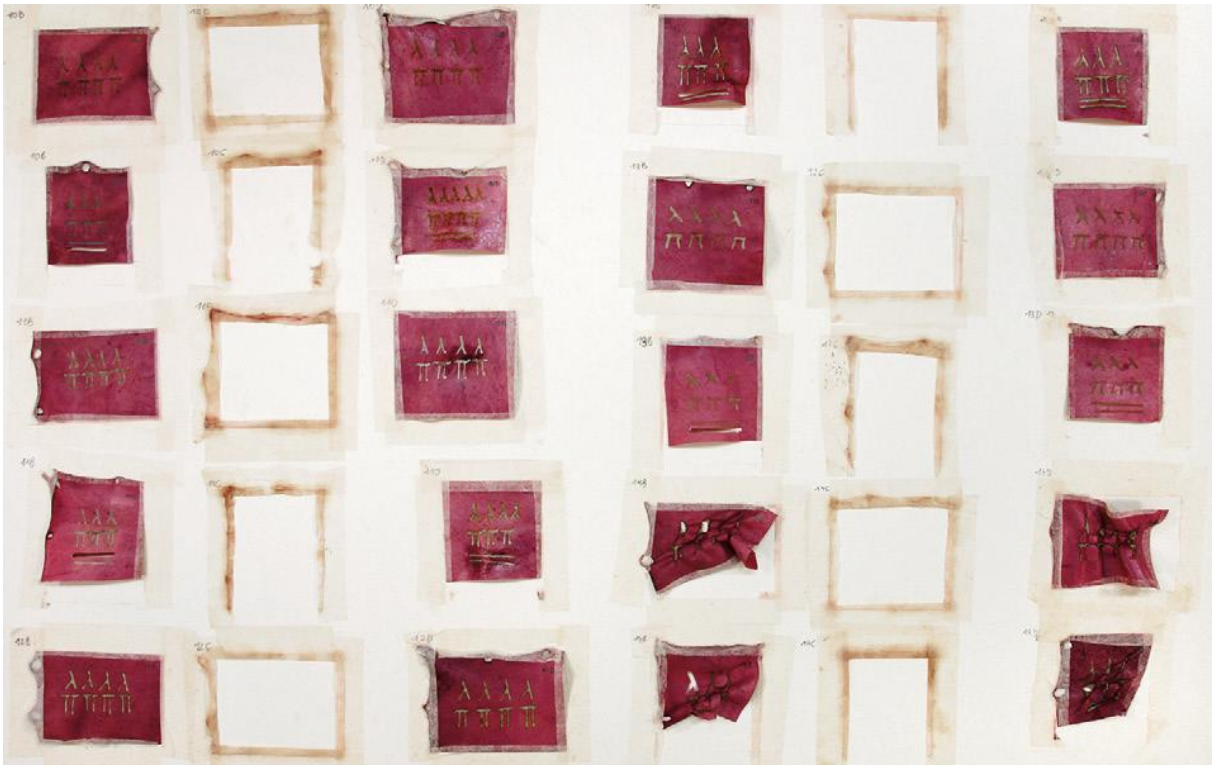

Figure 2: Mounted artificial parchment samples after the artificial ageing process. Ordered from left to right in B, C, D in two columns, starting with ST10 in the top left. Every sample was prepared twice. Samples of series C detached during ageing. [1]

2.2.2 Results

The phase analysis of the samples was performed by matching the resulting diffraction patterns with the diffraction data available in the PDF4+-database. An example of a diffraction Pattern with all phases identified is drawn in Figure 3. In this figure the uneven background caused by the amorphous parchment the ink was written on is visible.

All phases that were identified on the parchment samples of this series are depicted in Table 3.

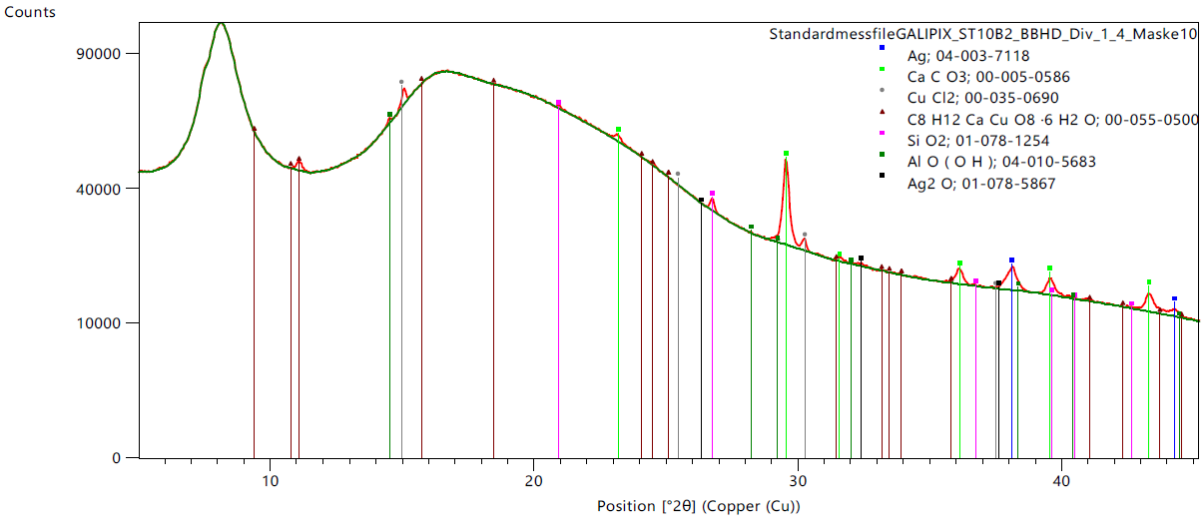

Figure 3: XRD data of the ST10B sample with identified phases

Table 3: Phases present in artificially aged ink on parchment samples

Present in most samples		Sometimes present	
DBN (PDF-4+)	Phase	DBN (PDF-4+)	Phase
04-003-7118	Ag	00-006-0464	CuS
00-005-0586	$CaCO_3$	04-012-4420	KNO_3
00-035-0690	$CuCl_2$	00-006-0480	AgCl
00-055-0500	CuCa-Acetate	01-078-5867	Ag_2O
01-075-0639	AlO(OH)		
01-078-1254	SiO_2		

The phases that were only present in some samples are depicted on the right side of Table 3. Both copper sulfide CuS and silver(1) oxide Ag_2O were not found on every sample and there was no obvious pattern to the appearance. Silver chloride AgCl and potassium nitrate / Salpeter KNO_3 usually appear together. The samples prepared with silver ink ST14 exhibited the worst damage to the parchment, with most samples being either destroyed completely or beyond the point of measurability. This hints at nitrate having a detrimental effect on the parchment during ageing.

All samples of treatment series C were also damaged very badly during the ageing process. In this case the samples detached from the mounting board. The samples of this series could not be measured using X-ray diffraction due to the damage that was sustained during ageing. In the bottom right the samples prepared using ST14, which includes KNO_3, deformed badly. Here the ink disintegrated the parts of the parchment it was written on, similar to the damage observed in the original Vienna Genesis (Figure 1).

It was concluded that the addition of nitrates to the ink, and/or contact with saltwater could be responsible for the damage observed on the original Vienna Genesis. These results offer directions to investigate the corrosion that destroyed the parchment, some of which were explored in this thesis.

2.3 Ag-Cu System

2.3.1 Phase Diagram

The silver-copper system is described by a simple phase diagram pictured in Figure 4 [3]. It consists of two solid solutions of silver in copper and vice versa, with a eutectic composition at 28.2 w% Cu and a eutectic temperature of 780 °C, which contains a maximum of 8.5 w% Copper dissolved in silver. The solubility of copper in silver drops with lower temperatures, with only 2 w% copper dissolved at 500 °C. The solubility of silver in the metallic copper phase is generally lower than that of copper in the metallic silver phase. At 500 °C only 1.2 w% silver is stable as a solid solution in copper.

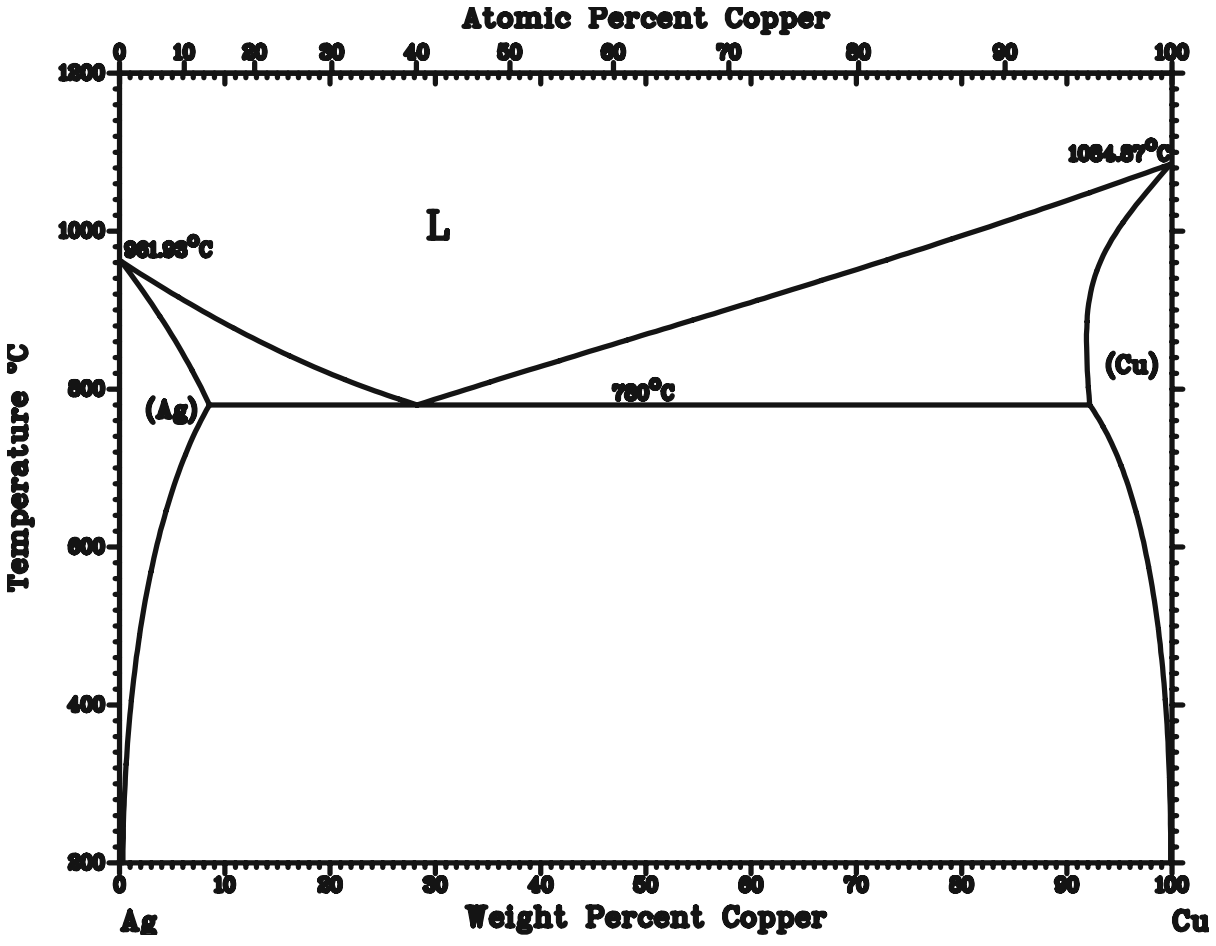

Figure 4: Phase diagram of the Silver-Copper-System. [3]

2.3.2 Vegard's Law

In an empirical finding published by Vegard in 1921 [4] it was proposed that the lattice parameters of solid solutions consisting of two constituents A and B can be calculated using equation 1.

$$a_{A_{(1-x)}B_x} = (1-x)a_A + x * a_B \quad (1)$$

a ..... Lattice parameter
x ..... Atomic fraction of constituent B

This provides an approximation of the lattice parameter of a solid solution if the elemental composition is known. However, it is an approximation and seldomly matches precisely with laboratory data. As a result, numerous deviations from Vegard's law are documented in literature [5].

It is still useful for providing a rough estimate in conditions where experimental data is unavailable, for example at non-ambient temperatures. For this reason, it was used to calculate starting values for Rietveld refinement at non-ambient temperatures, which is discussed in chapter 2.5. Furthermore, in systems known to follow Vegard's law, it can be used to approximate the composition of a solid solution from the measured lattice parameter.

The applicability of Vegard's law to the silver-copper system was studied by Linde [6] where a positive deviation was found. The published data was plotted in Figure 5 together with the lattice parameter *a* of the pure metals, which were obtained during the calibration described in chapter 4.3 "Calibration of Lattice Parameters", and the values predicted by Vegard's law using these refined parameters as base points.

Multiple samples were prepared during this thesis, with the highest copper content prepared at 10 w%. At this concentration, the deviation from Vegard's law is less than 0.5 %. Considering this, Vegard's law was applied as an approximation for the dependence of the lattice parameter on the composition at nonambient temperatures, as well as an estimation of the copper content from the measured lattice parameter.

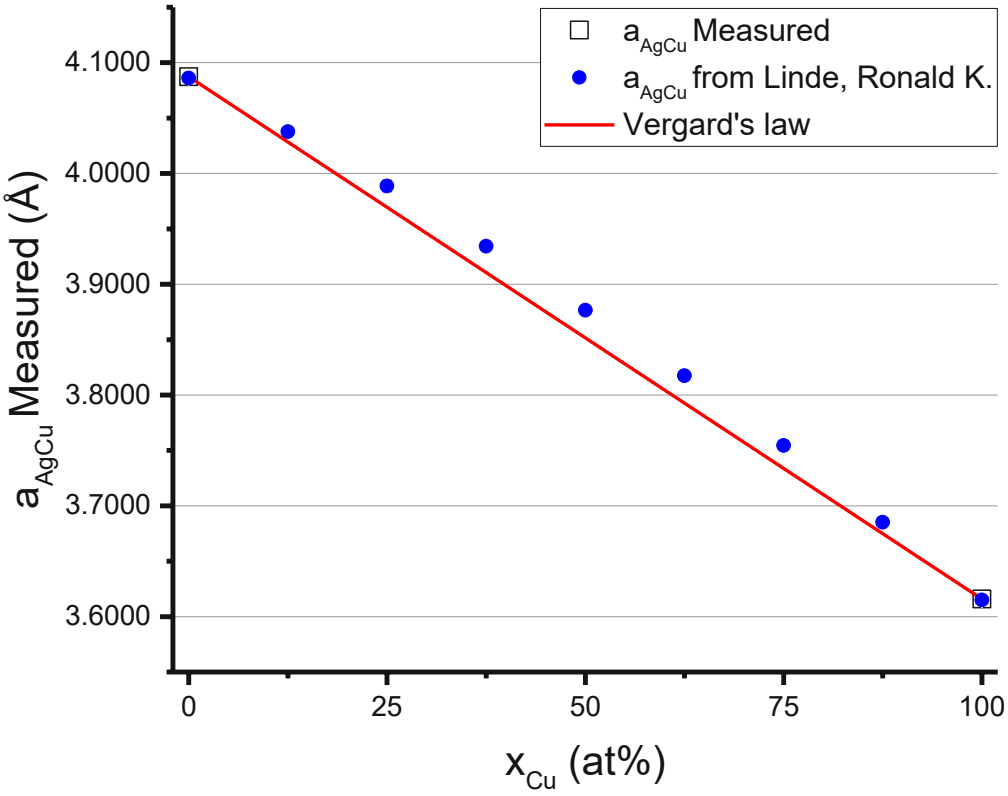

Figure 5: Lattice parameter a of Silver and Copper in a solid solution at different composition compared to Vegard's law

2.3.3 Oxygen Induced Segregation

The Ag-Cu system is known to be susceptible to oxygen induced segregation. [7] Due to this effect copper prefers to be located as the topmost layer of atoms if oxygen is present, otherwise silver is thermodynamically preferred. This causes copper atoms to diffuse to the surface at elevated temperatures, where it reacts with oxygen to form copper oxides. This segregates the silver-copper alloy, where the elements concentrate at different points in the material. Furthermore, silver does not seem to oxidise in these setups, as copper is a more reactive element and tends to diffuse to the surface. Additionally, it is documented in literature that silver(1) oxide decomposes in this temperature range, with some experimenters publishing lower, and some higher decomposition temperatures [8].

This system is extensively investigated for applications in the semiconductor and electronics industry, as well as a solder and a conductor for electrical applications [9]. Fundamental knowledge of this alloy therefore has a lot of potential applications.

2.4 Non-Ambient Powder XRD

2.4.1 X-ray source and beam optics

The X-Ray radiation used in this laboratory setup is produced in a standard X-ray tube, in which electrons are accelerated in vacuum into a specific anode material at high voltages. The high voltage accelerates the electrons with sufficient energies where a collision with electrons in the anode material converts some of the kinetic energy into high-frequency photons. The spectrum of radiation produced using this method is depicted in Figure 6.

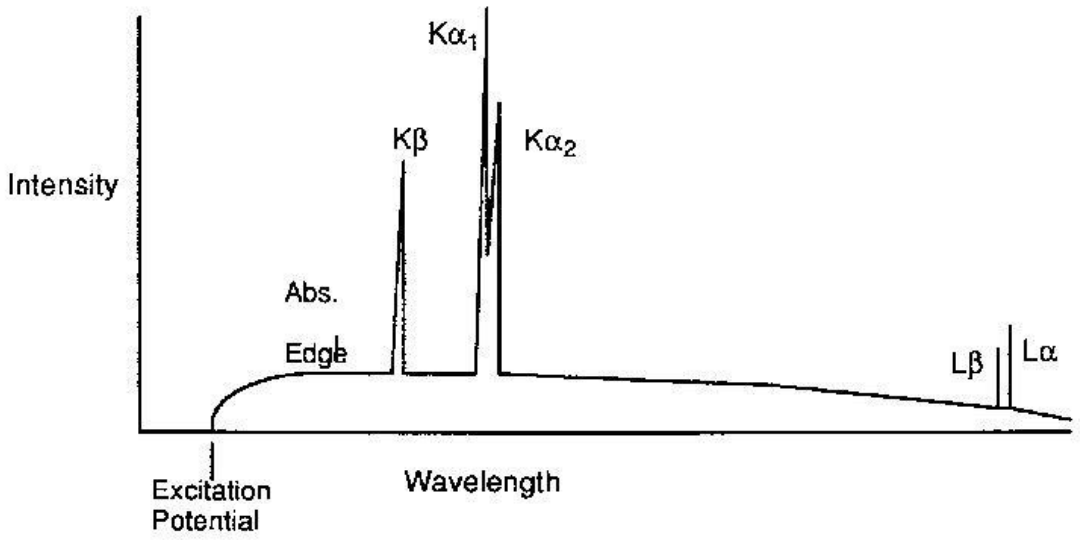

Figure 6: Spectrum of X-ray radiation produced in a classic X-ray tube. Source: http://ruby.colorado.edu/~smyth/G30105.html Obtained: 26.7.21

This spectrum consists of a continuous band of radiation, called Bremsstrahlung, which is produced during the rapid deceleration of the electrons hitting the anode, and lines with certain wavelengths called characteristic radiation. The wavelength of these lines is dependent on the anode material and is related to the binding energies of the electrons.

Most X-Ray diffraction experiments require a monochromatic wavelength beam, which is why characteristic radiation is often used in laboratory setups. Here the characteristic radiation used for the experiments is copper $K_{\alpha 1,2}$ radiation. However, as seen in Figure 6, X-ray tubes produce a spectrum of radiation in addition to the wanted characteristic line. This is one of the reasons why the beam is pre-treated using optical components.

Nowadays, there are many options concerning both primary and secondary X-ray optics when planning X-ray diffraction experiments. For this thesis two types of beam optics were used. Focusing optics (Bragg-Brentano), which focus and monochromatize the beam at the same time. Parallel beam optics

were applied for cases where the sample height is critical. These optics monochromatize and parallelize the beam. Due to the defined information depth, the latter can get rid of the specimen displacement error while sacrificing some intensity [10].

This displacement error is a result of the focusing beam used in Bragg-BrentanoHD optics, where the focal point of the beam is supposed to be on the sample. If the sample is displaced out of the plane of measurement, issues with phase identification as well as Rietveld refinement can arise in traditional Bragg-Brentano measurement setups due to strong shifts in the measured angles. This is not an issue with a parallel beam because it is not focused. Further information can be found in [10] and the therein cited references.

2.4.2 High Temperature / Non-Ambient X-Ray Diffraction

The experiments introduced in the following were performed in non-ambient conditions. While the basic principles of X-Ray diffraction stay the same, there are some differences that should be noted.

Due to thermal expansion the lattice of most materials expands, as expressed by increasing lattice parameters, consequently affecting the measured peak positions. In the case of silver, a temperature difference of 250 °C manifests itself in an increase of the lattice parameters of ~0.02 Å, which shifts the diffraction maxima by up to 0.5° 2θ dependant on the absolute θ-value.

This expansion is not limited to the sample. When heating the reaction chamber all components will slightly expand. Due to this, an expansion table for the sample chamber and -holder was used to compensate the resulting specimen displacement error.

To perform these measurements different atmospheres were required, namely hydrogen, argon, nitrogen, and pressurized air. These gases were sourced from standard laboratory gas cylinder. The electron density of the atmosphere inside the reaction chamber causes measurable differences in the X-ray diffraction measurements. Argon is denser than air, which reduces the measured intensities, while hydrogen is less dense, which results in much higher intensities measured. This happens because X-Ray radiaton is absorbed when passing through matter. This effect is dependent on the electron density since the radiation interacts with the electrons. As a result, dense gases like argon absorb more radiation when compared with oxygen or nitrogen in air, or pure hydrogen gas. This can cause extreme differences in the observed intensities. For example, an argon atmosphere during the measurement can half the observed intensity compared to air.

2.5 Rietveld Refinement

2.5.1 General Information

To evaluate the results a technique known as "Rietveld Refinement" was applied [11]. This technique calculates a theoretical diffraction pattern point by point based on a structural model and adapts the parameters to describe the structure. By applying a least square approach to adjust the parameters of a mathematical model describing the diffraction pattern, the difference between the calculated and measured profile is minimized. This allows to obtain a very precise model of the measured sample and results in extra information from the powder XRD data, like the lattice parameters, phase quantities, atomic coordinates, texture effects, etc. For this study unit cell dimensions are the most important information obtained from refinement.

This method, developed by Hugo Rietveld in 1967 [12], requires a huge number of complex calculations, which is the reason why special computer software is used when applying this method. Today, this functionality is included in most software for powder crystallography. In this study, every refinement was performed using HighScore Plus developed by PANalytical [13].

2.5.2 Principle of the Rietveld Method

The general equation is given in equation 2. It calculates the intensity at point *i* in the diffraction pattern.

$$y_{ic} = y_{ib} + \sum_{p} \sum_{k=k_1^p}^{k_2^p} G_{ik}^p I_k \qquad (2)$$

y_{ic} ..... total intensity calculated at point i
y_{ib} ..... background intensity
G_{ik} ..... normalized peak profile function
I_k ..... intensity of the k^{th} Bragg reflection
k ..... reflection contributing to the intensity
p ..... phases present

By applying the method of Sonneveld & Visser [14], a background is also calculated at every measured point. This is used to describe the background y_{ib} in the model. Alternatively, the background can be modelled based on a refinable function, which approaches the background modulation by a linear part. The modulations are approximated quite often using polynomials of different grades.

2.5.3 Scattering intensity term

The Intensity I_k is calculated using Equation 3.

$$I_k = SM_kL_k|F_k|^2P_kA_kE_k \quad (3)$$

S ..... scale factor
M_k ..... multiplicity
L_k ..... Lorentz polarisation factor
F_k ..... structure factor
P_k ..... preferred orientation factor (no preferred orientation → $P_k = 1$)
A_k ..... absorption correction
E_k ..... extinction correction

This describes the intensity of each reflection based on several parameters. The scale factor is a variable which is used to control the strength of this term. Furthermore, the factor includes a phase concentration parameter.

The multiplicity describes the number of symmetry equivalent reflections with the same d spacing that contribute to the single reflection observed in powder diffraction data.

The Lorentz polarisation factor L_k is involved with converting the structure factor into radiation intensities and is calculated using equation 4. The Lorentz factor considers the different velocities a reflection is staying in reflection conditions dependant on the scattering angle. The polarisation factor describes the polarisation ratio of the X-ray beam. Both factors are dependent on the scattering angle and therefore combine to one correction factor.

$$L_k = \frac{1 + cos^2 2\theta}{sin^2\theta * cos\theta} \quad (4)$$

θ ..... diffraction angle

The structure factor F_k is calculated using equation 5. The squared modulus describes the scattering intensity. The required structural information is taken from a reference pattern of the refined phase. Hence structural data must be available for the starting values for the Rietveld refinement.

$$F_k = \sum_{j=1}^{n} f_j e^{2\pi i(h_r^t r_j - h_k^t B_j h_k)} \quad (5)$$

f_j ..... Scattering factor of the atom j
h_k ..... matrix representing Miller indices
r_j ..... matrix representing atomic coordinates
B_j ..... matrix representing anisotropic thermal vibration parameters

In this analysis the preferred orientation factor P_k was not required. Therefore, it was fixed to the value one.

Finally, the absorption and extinction are corrected using the A_k and E_k terms. However, both terms are not refined in this study.

2.5.4 Peak profile function

While there are many profile functions to choose from, in this study only the Pearson 7 profile function (Equation 6) was used because it provided a more accurate description of the laboratory data when compared with the results produced using pseudo-Voigt or Voigt profile functions.

$$G_{jk} = \frac{2\Gamma(\gamma)}{\Gamma(\gamma - 1/2)} \frac{C_2^{1/2}}{H_k \pi^{1/2}} \left[1 + 4C_2 X_{jk}^2\right]^{-\gamma} \quad (6)$$

Γ……. Gamma function
γ …….. peak shape parameter
C_2 …… = $2^{1/\gamma-1}$
H_k …… full-width and half-maximum (FWHM) of the k^{th} Bragg reflection
X_{jk} …… = $(2\theta_j - 2\theta_k)/H_k$

This profile function consists of two basic functions, the Lorentz and Gauss profile. The weight of each basic function is determined by the refinable parameter γ, also called Peak shape. The peak width is calculated using the Caglioti function (Equation 7) [15].

$$H_k = (U * tan^2(\theta) + V * tan(\theta) + W)^{1/2} \quad (7)$$

U, V, W ……. refinable parameters
θ ……. diffraction angle

The peak asymmetry is modelled by splitting the width and shape into separate parameters for the left and right side of the peak.

2.5.5 Relevance of the Refinements

The calculated diffraction pattern needs to match the measured pattern as closely as possible. One way to compare the patterns is by plotting the calculated data together with the measured data. This way the difference between the calculated points and the measured points is visually apparent but can also be described in a separate difference plot.

The quality of a refinement is also described using R-factors and the "Goodness of Fit" or GOF. To assess the difference between the model and measured data the weighted profile R-factor R_{wp} is calculated using Equation 8.

$$R_{wp} = \left[\frac{\sum w_i (y_{io} - y_{ic})^2}{\sum w_i y_{io}^2}\right]^{1/2} * 100 \quad (8)$$

R_{wp} ..... weighted profile R-factor
y_{io} ..... total intensity observed at point i
y_{ic} ..... total intensity calculated at point i

The weight factor is calculated from Equation 9 and is dependent on the standard uncertainty or estimated standard deviation (ESD).

$$w_i = \frac{1}{\sigma^2} \quad (9)$$

w_i ..... Weight factor of point i
σ ..... estimated standard deviation

Assuming a model which perfectly describes the observed data, Equation 8 can be expressed as Equation 10, which describes the best possible R-factors attainable from this dataset, also called R_{exp}.

$$R_{exp} = \left[\frac{N - P}{\sum w_i y_{io}^2}\right]^{1/2} * 100 \quad (10)$$

R_{exp} ..... best possible R-value for this dataset
N ..... Total number of data points
P ..... Total number of refined parameters

These R-factors are combined in Equation 11 and expressed as the Goodness of Fit. This value should be as close to 1 as possible.

$$GOF = \left[\frac{R_{wp}}{R_{exp}}\right] \quad (11)$$

However, these parameters do not describe the fit perfectly. Nonsensical results can exhibit an exceptionally good GOF while being obviously wrong because a fitting parameter diverged to its limit. The user must manually check and evaluate if the result produced by refinement is valid, but the GOF and R_{wp} offer information about the progress and general quality of the refinement.

3 Measurement Setup

3.1 XRD-Setup

All non-ambient measurements were performed on a PANalytical XPert Pro MPD (θ-θ diffractometer). The X-Ray source was an Empyrean Cu LFR HR X-ray tube, which produces copper $K_{\alpha 1,2}$ radiation with a wavelength of 1.540598 Å for $K_{\alpha 1}$ and 1.544426 Å for $K_{\alpha 2}$ at an intensity ratio of 0.50 with an angle divergency in the scattering plane of 0.2° on top of a Bremsstrahlung spectra.

Two different beam optics were used during the corrosion experiments. The first setup used a standard Bragg-Brentano High-Definition monochromator produced by PANalytical [16]. More information about the functionality can be found in [17]. This was combined with a 10 mm mask, a 1/2 ° divergence slit, a 2 ° anti-scatter slit and a 0.04 rad Soller slit on the primary beam side.

The second setup used a Parallel-beam mirror, which was also produced by PANalytical and is based on a parabolic graded W/Si Crystal producing a parallel beam out of the divergent primary beam. This was combined with a 10 mm mask, a 1/4 ° divergence slit, and a 0.04 rad Soller slit. An anti-scatter slit was not necessary since a parallel beam was used.

The detector was a standard PANalytical X'Celerator RTMS type semiconductor detector.

Figure 7 shows a picture of the inside of the X-ray diffraction (XRD) with the described parallel beam measurement setup.

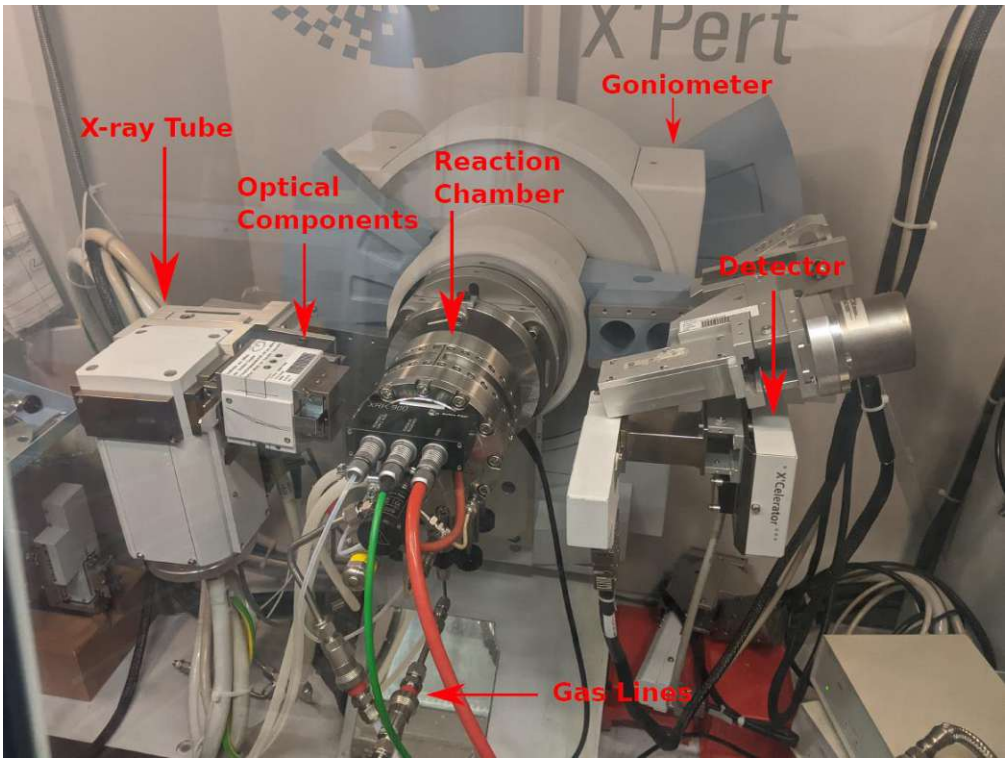

Figure 7: Picture of the used XRD setup using the parallel beam mirror

3.2 Non-Ambient Setup

3.2.1 Reaction Chamber

To achieve non-ambient temperatures and a non-air atmosphere, a reaction chamber was necessary. For these experiments, a standard Anton Paar XRK 900 reaction chamber was used. The atmospheres used during the experiments were pressurised air, hydrogen, nitrogen, and argon. Figure 8 shows a schematic drawing of the setup used for the experiments, with the sample illustrated in grey on top of the movable sample stage.

The non-ambient temperatures cause thermal expansion, requiring a movable sample stage to compensate this height change. Otherwise, a massive sample displacement error is present at higher temperatures. However, due to the nature of the prepared sample, specimen displacement is almost unavoidable. For this reason, a parallel beam mirror was used, since this optical component circumvents specimen displacement below multiple millimetres [10].

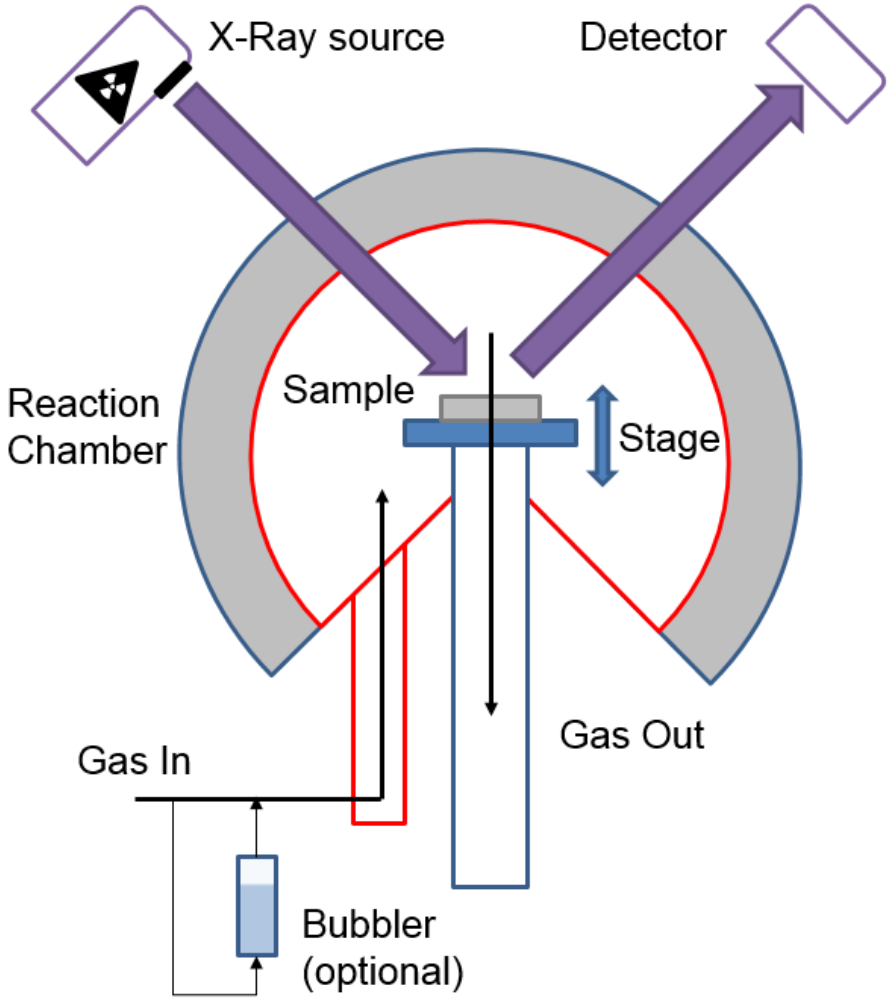

Figure 8: Schematic drawing of the non-ambient setup used.

3.2.2 Atmosphere Control

The atmosphere was provided using a standard pressurised gas bottle hooked up to the laboratory gas supply. While many gases were available, only hydrogen, argon, nitrogen, and pressurized air were used in the experiments. The gas flow was checked using a flow meter at the end of the gas line and adjusted to 0.5 l/min in all cases.

3.2.3 Brine spray

To investigate the effect of brine spray on the silver alloys, a bubbler filled with brine was placed in the gas inlet line. This brine was prepared by dissolving 3.5 w% sea salt in distilled water. The inlet was gas pumped through a pressurized bubbler system (Figure 9) before entering the reaction chamber. The gas is inserted on the right side. It then rises through the brine in the middle part and sprays some water droplets into the gas stream after bubbles reach the surface. This spray gets carried to the reaction chamber through the white tube exiting the bubbler on the left, where it can interact with the sample.

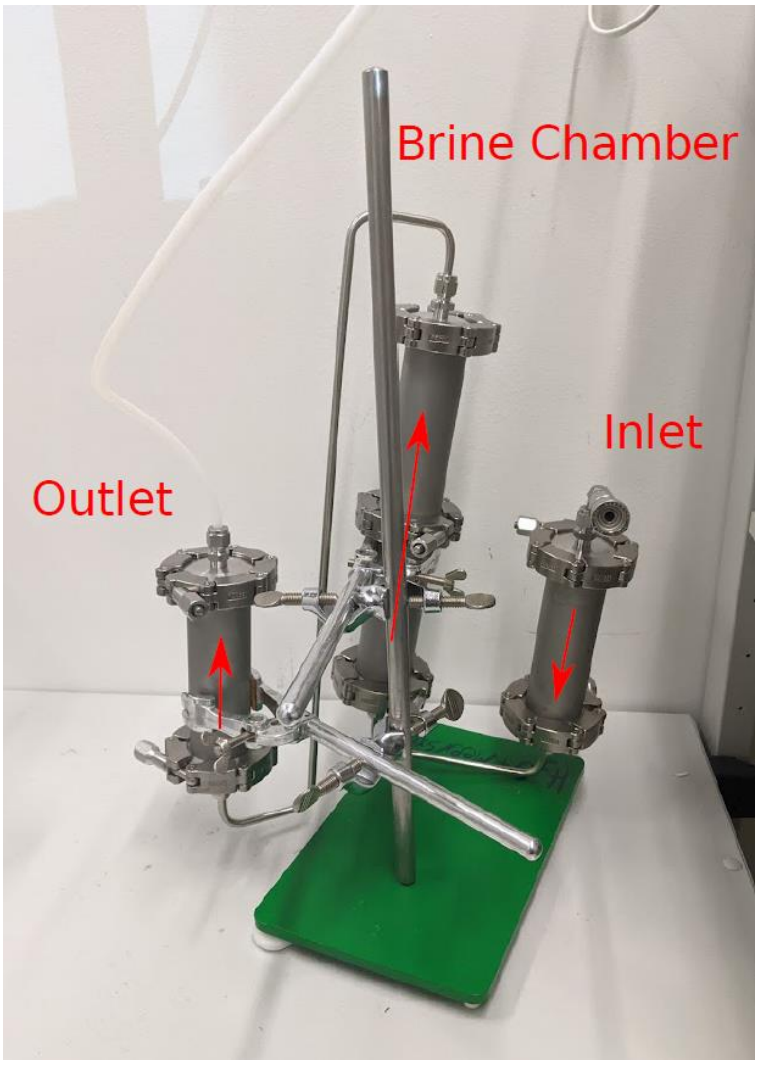

Figure 9: High pressure bubbler system used to produce brine spray

3.3 Alloy Preparation Route

The samples for these experiments had to fulfil several requirements. Firstly, the sample hat to be a metallic silver-copper alloy with a specific copper content. The sample also needs a big surface area, like in a powder, and be (poly)crystalline. Unfortunately, a commercial product with these requirements was not available at the time. A sample preparation method was developed, which is based on the in-situ reduction of a precursor mixture, to obtain a metallic silver-copper alloy with the desired properties. This method was developed using the synthesized silver oxide mixture described in chapter 4.2 before commercial silver(1) oxide was acquired.

Generally, the precursor mixtures were prepared by grinding corresponding amounts of silver(1) oxide Ag_2O and copper(2) oxide CuO with a mortar and pestle, until the mixture was homogenous. An internal standard or other additives can be added at this point as well.

Figure 10 shows the empty sample holder. The sample is placed in the top part, the cable is attached to the temperature sensor unit, the gas adapter in the middle is used for gas inlet and the red adapter at the bottom is used as the gas outlet.

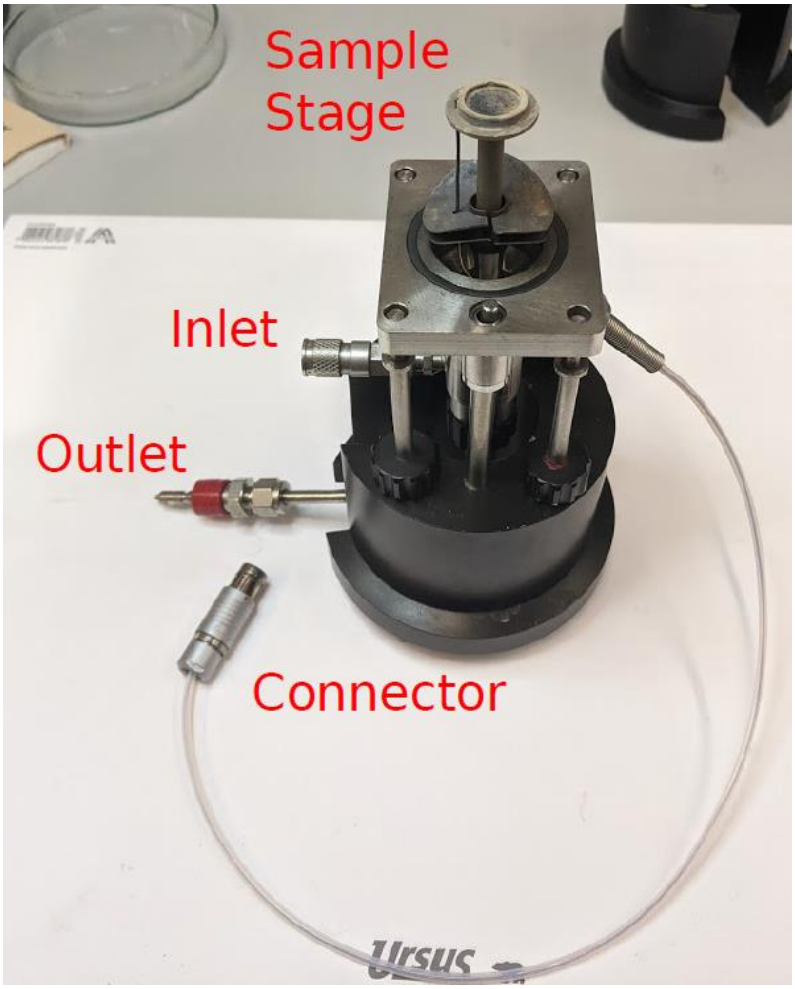

Figure 10: Empty sample holder for the XRK 900 reaction chamber.

To prevent powder from being carried out of the reaction chamber by the gas flow, the bottom of the sample holder is covered with two layers of filter material made from glass fibres, which was cut to fit into the holder. These glass fibres are amorphous and thus don't exhibit strong x-rays diffraction maxima. The precursor mixture is then loaded into the sample holder using a spatula, pressed down, and the surface is scraped until it is even. Afterwards the sample holder is cleaned using a brush and attached to the XRD instrument.

The reduction is achieved by first flushing the air for 30 minutes using argon, switching to a hydrogen atmosphere, and flushing the argon for 30 minutes. This is followed by heating the sample to 500 °C where it is held for 30 minutes, after which one diffraction pattern is measured at 275 °C. Afterwards the hydrogen is flushed again for 30 minutes using argon while the sample cools. After this point, the sample is ready for the corrosion experiment. The temperature profile of this reduction, including representative data from one reduction, is shown in Figure 11. Figure 12 shows representative images of a sample produced following this route before the reduction and after the corrosion.

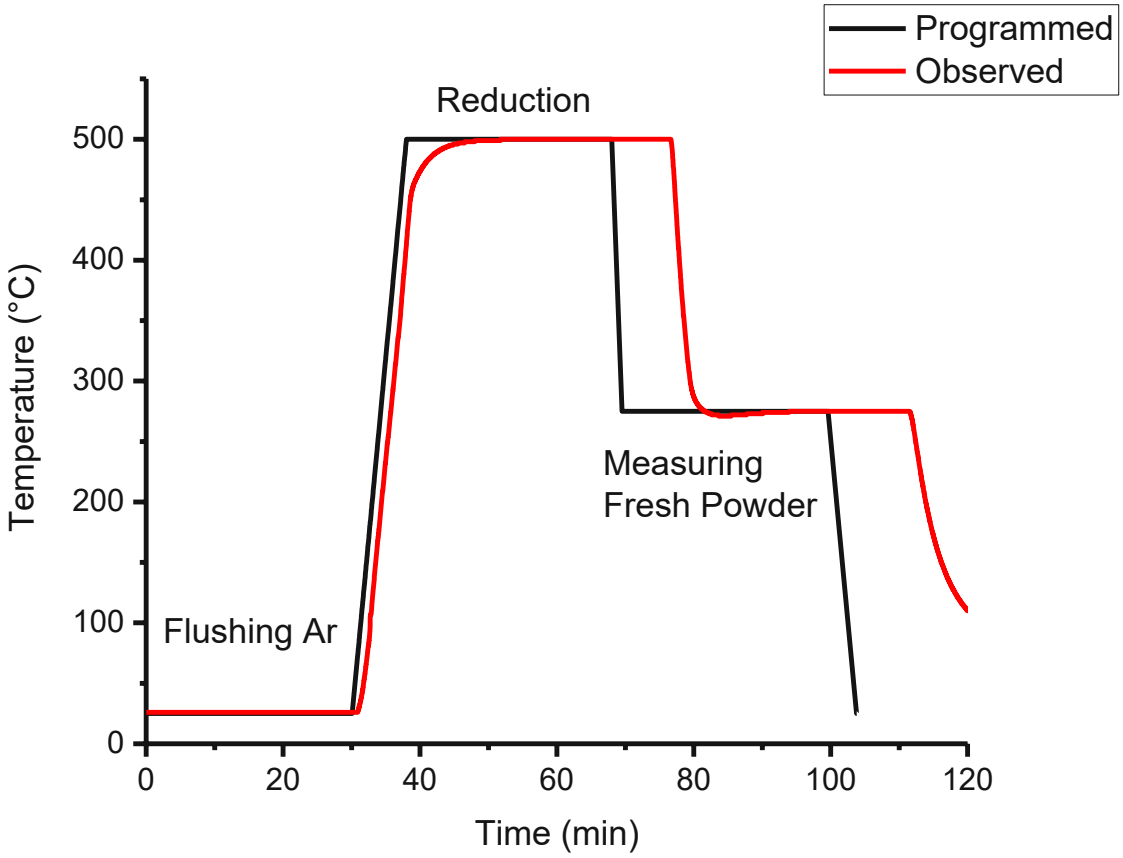

Figure 11: Temperature profile of the reduction step in the alloy preparation route

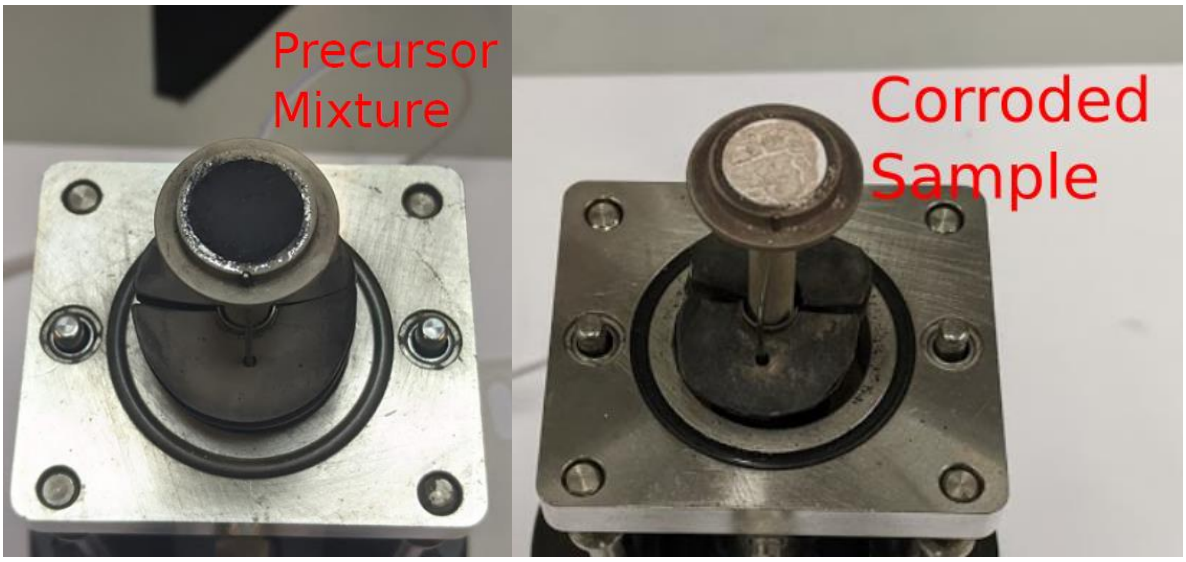

Figure 12: Sample holder with Ag_2O + CuO precursor mixture before (left) and after (right) the corrosion experiment.

Samples prepared following this route meet all the requirements. It should be noted however that some parts of the silver are amorphous. Further details about the properties of the samples prepared following this route can be found in the scanning electron microscopy chapter 6.3 “Scanning Electron Microscopy Images”.

3.4 Corrosion Measurement

To track the changes happening to the sample during the corrosion process, powder X-ray diffraction (PXRD) was measured during the reaction. A measurement program, which requires 30 minutes to finish, was repeated multiple times during the corrosion experiment to gather the data. The non-ambient temperature profile of one corrosion experiment is depicted in Figure 13. Here the series corroding a 10 w% copper alloy with an internal standard is pictured (chapter 4.5.3), which includes a recrystallisation step at 500 °C. The measurement starts as soon as the reaction chamber reaches the set reaction temperature of 275 °C, which is Time = 0 in Figure 13. After this point the measurement program is repeated for the programmed duration. In this series a recrystallisation step follows, where the sample is heated to 500 °C for 1 hour, followed by further measurements until the series is concluded by letting the sample cool.

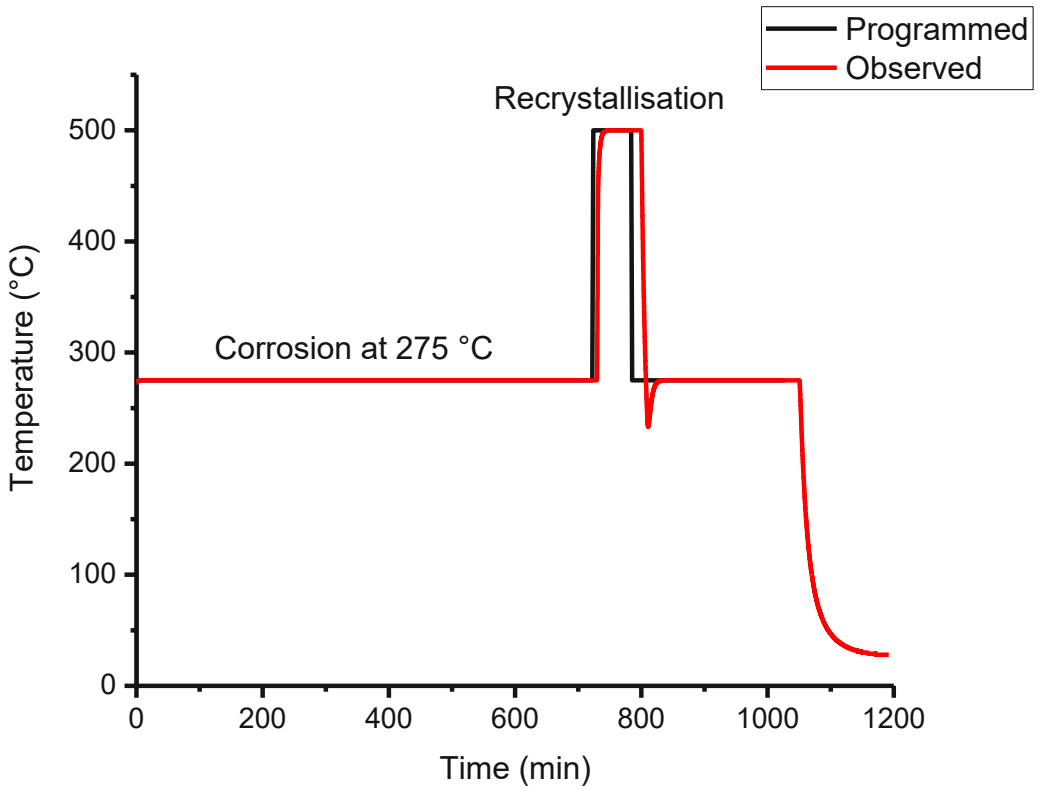

Figure 13: Non-ambient temperature profile of the corrosion measurements described in chapter 4.5.3

The corrosion was achieved by treating the prepared alloy with pressurized air and brine spray, which are introduced through the gas inlet line. A blind measurement under an inert argon atmosphere was also measured to confirm the stability of the sample during the temperature program. By using a temperature controller, the temperature inside the reaction chamber is adjusted and tracked throughout the experiment. The observed temperature is pictured in red in Figure 13. After the final measurement, the sample is cooled to room temperature, after which it can be removed to prepare the next experiment.

4 Samples and Measurements

4.1 Overview of Measurement Series

Table 4 shows an overview of all prepared samples with their respective composition, measurement parameters, used corrosive agents and complementary information. It should be noted that 10 w% Cu / 1.5 w% Cu are the intended composition. The prepared precursor mixtures have slightly different actual compositions of 9.57 w% and 1.49 w% copper respectively. Also, all experiments were performed at 275 °C unless stated otherwise.

Table 4: Overview of measured samples with the composition, measurement parameters and corrosive agents

Series Name	Composition	Measurement Parameters	Corrosive Agents	Notes
Temperature Variation	~ 10 w% Cu (impure)	36x 25 - 70 °2θ 18h	Air Brine	Repeated in 50 °C steps from 25°C to 375 °C
10wCu_Air	10 w% Cu	36x 25 - 120 °2θ 18h	Air	Repeated after homogenisation
10wCu_NaCl	10 w% Cu	29x 50 - 83 °2θ 2x 25-120 °2θ 15.5h	Air Brine	Smaller Angle range except first and last
10wCu_LECO	10 w% Cu	34x 25 - 120 °2θ 17h	Air	Homogenized precursor mixture, oxygen content known
10wCu+Al_2O_3_Air	10 w% Cu	24x 25 - 120 °2θ 8x 25 - 120 °2θ 17h	Air	Recrystallisation at 500 °C for 1h after 12h corrosion
10wCu+Al_2O_3_Blind	10 w% Cu	24x 25 - 120 °2θ 8x 25 - 120 °2θ 17h	Argon	Recrystallisation at 500 °C for 1h after 12h corrosion
10wCu_Long	10 w% Cu	470x 25 - 120 °2θ 235h	Air Brine	Long-Term Experiment at 75 °C
1.5wCu+Al_2O_3_Air	1.5 w% Cu	24x 25 - 120 °2θ 10x 25 - 120 °2θ 18h	Air	Recrystallisation at 500 °C for 1h after 12h corrosion

4.2 Synthesis of Ag_2O

Synthetic silver oxide was prepared for use in the preliminary experiments. The synthesis can be achieved by following a simple route. In the first step (equation 12) silver metal is dissolved using hot nitric acid to produce a solution of silver nitrate. This solution is then neutralized using a sodium hydroxide solution (equation 13) to produce silver hydroxide, which is unstable under these conditions and rapidly decomposes to form silver oxide (equation 14).

$$3\,Ag + 4\,HNO_3 \rightarrow 3\,AgNO_3 + 2\,H_2O + 1\,NO \quad (12)$$

$$AgNO_3 + NaOH \rightarrow AgOH + NaNO_3 \quad (13)$$

$$2\,AgOH \rightarrow Ag_2O\downarrow + H_2O \quad (14)$$

This route was followed using 4.70 g refined silver granulate (Ögussa, ≥ 99.99 %). This was mixed with ~20 ml concentrated nitric acid in a beaker and heated until the silver dissolved completely. After the mixture cooled down to room temperature the acid was neutralized using a 1 mol/L solution of sodium hydroxide, which caused a brown precipitate to form. The base was added until no new precipitate formed. The beaker was then covered with parafilm, wrapped in aluminium foil to protect the light sensitive product and stored overnight in a dark place to let the fine precipitate agglomerate and settle at the bottom. The solution was decanted, the precipitate washed with distilled water and left in the beaker to dry while protected from light.

4.3 Calibration of Lattice Parameters

The lattice parameter of silver is dependent on the temperature. To calibrate this dependence a sample of pure silver / pure copper with an added internal standard was prepared.

To calibrate silver, 4.50 g silver(1) oxide (Aldrich, ≥ 99.99 %) was mixed with 0.51 g of Alumina (NIST Standard Reference Material (SRM) 676a [18]) using a mortar and pestle. For copper 2.37 g copper(2) oxide (Merck, p.a.) was mixed with 0.27 g of the aforementioned alumina standard.

These precursor mixtures were then treated as described in chapter 3.3 “Alloy Preparation Route” and measured in 25 °C steps between 25 °C and 400 °C under N_2 to provide an inert atmosphere. Nitrogen was chosen instead of argon to achieve higher counting statistics, since argon is denser and absorbs more X-rays.

4.4 Temperature Variation Series

This was the first measurement series that was performed, with the goal of identifying at which temperatures corrosion phenomena occur. The precursor mixture was prepared by mixing 1.87 g of the synthetic Ag_2O with 0.14 g of copper(2) oxide (Merck, p.a.) using a laboratory mixer mill (Retsch MM 400) in a tungsten carbide vessel and grinding ball at 25 Hz for 1 min.

These precursor mixtures were then treated and reduced as described in chapter 3.3 “Alloy Preparation Route” and the corrosion measured in 50 °C steps between 25 °C and 375 °C with pressurized air and brine.

Figure 14 shows the corroded samples side by side. A colour change can be observed in the samples corroded above 200 °C, which was not present after the original corrosion and developed over time. This reaction is explored further in chapter 6.7 “Oxygen induced segregation”.

Figure 14: Corroded Samples of the Temperature Variation series prepared using synthesized Ag_2O and commercial CuO. Corroded using pressurized air and brine. Temperatures start with 25 °C on the left and increase in 50 °C steps. Picture taken 19 months after the original experiment.

4.5 10 w% Copper Alloy

4.5.1 Pure Alloy / 10wCu series

To prepare a precursor mixture which results in 10 w% copper in the reduced state, 2.90 g of silver(1) oxide (Aldrich, ≥ 99.99) were mixed with 0.36 g copper(2) oxide (Merck, p.a.) using a mortar and pestle. The true elemental composition in the reduced state is therefore 90.43 w% Ag and 9.57 w% Cu.

The alloy was then reduced as described in the chapter 3.3 “Alloy Preparation Route” and the corrosion with air measured at 275 °C between 25 ° and 120 ° 2θ with pressurized air in the parallel beam setup. The sample corroded with air and brine spray was measured at 275 °C in a smaller angle range of 50 to 83 °2θ in the parallel beam setup.

Following some inconsistent homogenisation, the corrosion with air was repeated after further grinding in the mortar and pestle. This sample was also used for the oxygen content analysis and was produced at a later date.

Figure 15 shows the prepared and corroded samples. The sample on the left was corroded with air only, the sample on the right with air and brine. In the right sample the filter material is also visible. The second sample corroded with air is not shown, since it was destroyed during the oxygen content measurement.

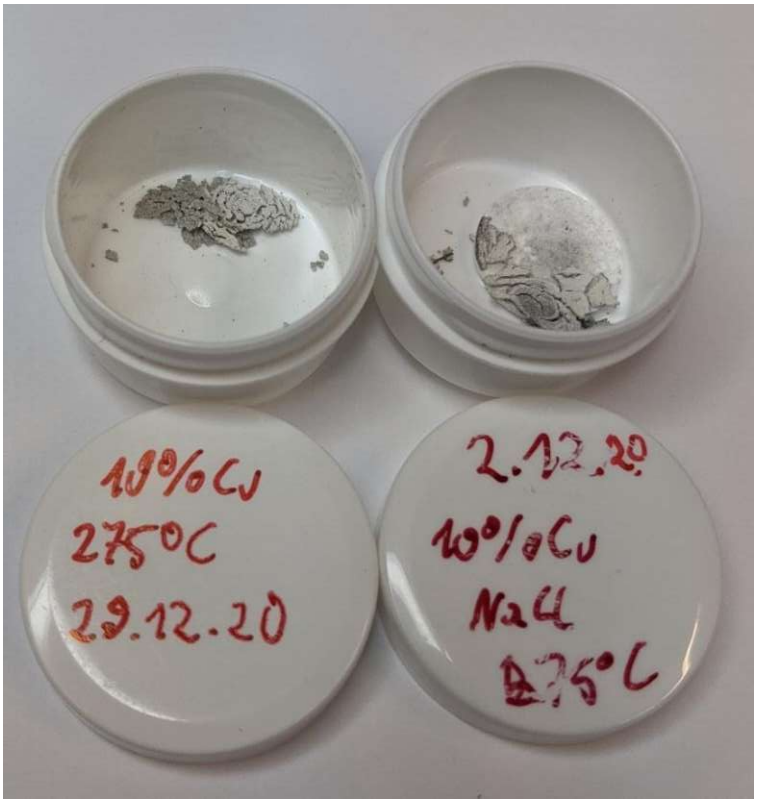

Figure 15: Corroded Samples of the 10wCu series prepared using commercial Ag2O and CuO. Corroded using pressurized air only (left; 10wCu_Air) and pressurized air and brine (right; 10wCu_NaCl). Picture taken 7 months after the original experiment.

4.5.2 Oxygen Content Analysis / 10wCu LECO

The oxygen content of a 10 w% Cu silver-copper alloy sample was analysed using an LECO TC500 Series Elemental Analyzer. In this method a weighed amount of the sample is placed in a graphite crucible and heated using an impulse furnace. At these high temperatures the bound oxygen is released, which reacts with the graphite crucible to form CO and CO_2. These gases are extracted with helium as an inert carrier gas and detected with a nondispersive infrared sensor. This allows the software to calculate the oxygen content of the sample by comparing the signal to a standard. In this case an oxygen in copper reference sample was used as the standard, which has an oxygen content of 0.0543(8) w%.

The alloy was prepared as described in Chapter 3.3 “Alloy Preparation Route” and corroded using air for 17 hours. After the sample cooled down to room temperature the alloy wafer was removed from the sample chamber and stored in an argon atmosphere for 16 weeks to prevent further oxidation before the oxygen content analysis.

The samples were prepared by removing the filter material as much as possible and breaking the thin wafer into multiple small pieces. These fragments were then placed in an oxygen free tin metal tube and the weight noted. Afterwards, the tube was sealed and inserted into the reaction chamber together with a fresh graphite crucible. The analyser then purges the chamber, removes adsorbents, and starts the measurement. In total 6 samples were prepared from one wafer.

4.5.3 Samples containing an Internal Standard / 10wCu+Al_2O_3 series

To introduce an internal standard to the 10 w% Cu precursor mixture 2.09 g of the mix described in the previous chapter were combined with 0.34 g of the NIST SRM 676a Alumina standard [18] and mixed with a mortar and pestle until the mixture was homogenous.

The alloy was then reduced as described in the chapter 3.3 “Alloy Preparation Route” and the corrosion measured at 275 °C between 25 ° and 120 ° 2θ with pressurized air in the parallel beam setup for 12 hours. To test the temperature properties of the segregated species a recrystallisation at 500°C for one hour was performed. Afterwards the sample was cooled back down to 275 °C and measured for 4 hours to see if any further reaction is observed. Additionally, a fresh sample was measured under an inert argon atmosphere as a blind value to test the stability of this sample during the temperature program.

Figure 16 shows the prepared and corroded samples next to each other. A colour change can be observed between the sample corroded with air and the blind.

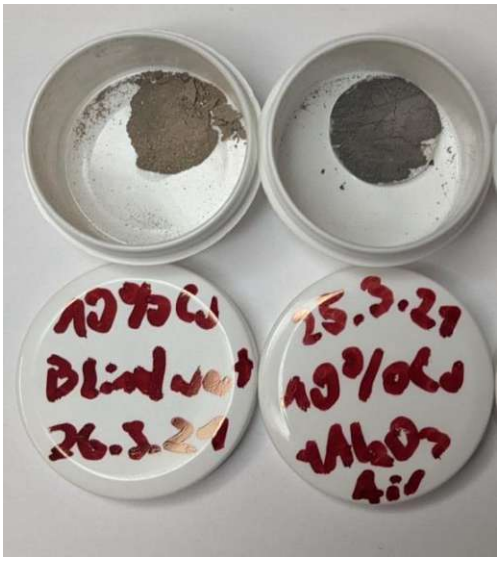

Figure 16: Corroded samples of the 10wCu+Al_2O_3 series. One sample was measured under argon as a blind (left) and one corroded with air (right).

4.5.4 Long-Term Experiment /10wCu_Long

A long-term experiment of this composition was also performed to test for corrosion processes at a lower temperature. The precursor mixture without the internal standard was treated as described previously and the corrosion measured at 75 °C between 25 ° and 120 ° 2θ with pressurized air and brine spray. This experiment lasted for a total of 470 measurements in 10 days.

Figure 17 shows the corroded sample. The shrinkage of the sample during reduction led to large cracks in the metal wafer, which are very visible in this sample.

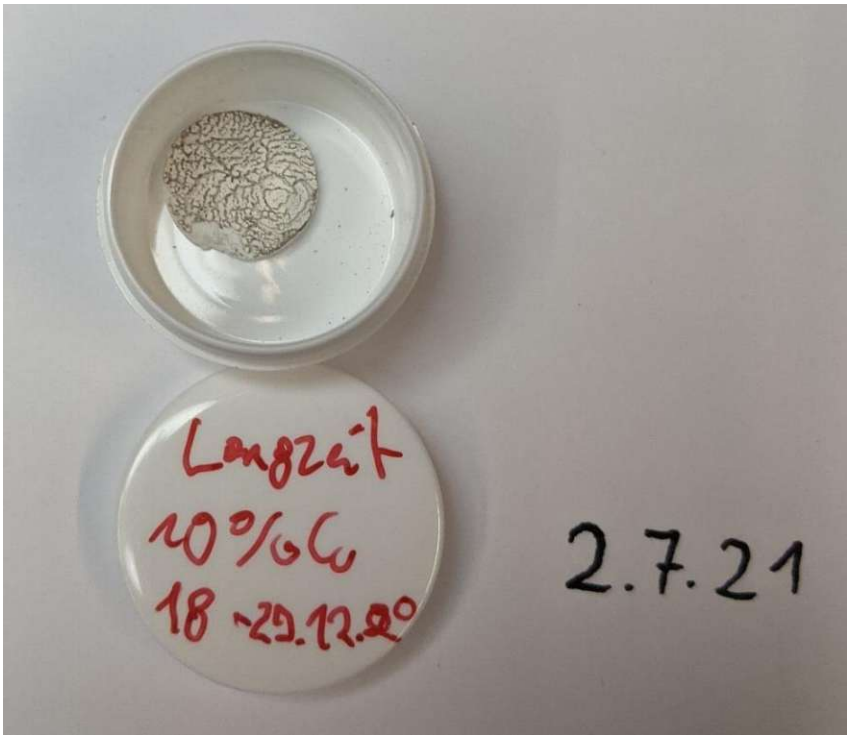

Figure 17: Corroded sample for the 10wCu_Long series. Picture taken 6 months after the original experiment.

4.6 1.5 w% Copper Alloy

4.6.1 With internal Standard / 1.5wCu+Al_2O_3 Air

To prepare a precursor mixture which results in 1.5 w% copper in the reduced state 3.176 g of silver(1) oxide (Aldrich, ≥ 99.99) were mixed with 0.056 g copper(2) oxide (Merck, p.a.) using a mortar and pestle. The true elemental composition in the reduced state therefore is 98.51 w% Ag and 1.49 w% Cu.

Similar to the 10 w% Cu sample, a mixture containing an internal standard was prepared by mixing 1.65 g of this precursor mixture with 0.26 g of the NIST alumina standard [18] using a mortar and pestle.

The alloy was then prepared as described in chapter 3.3 “Alloy Preparation Route” and the corrosion measured at 275 °C between 25 ° and 120 ° 2θ with pressurized air in the parallel beam setup.

Figure 18 shows the corroded sample.

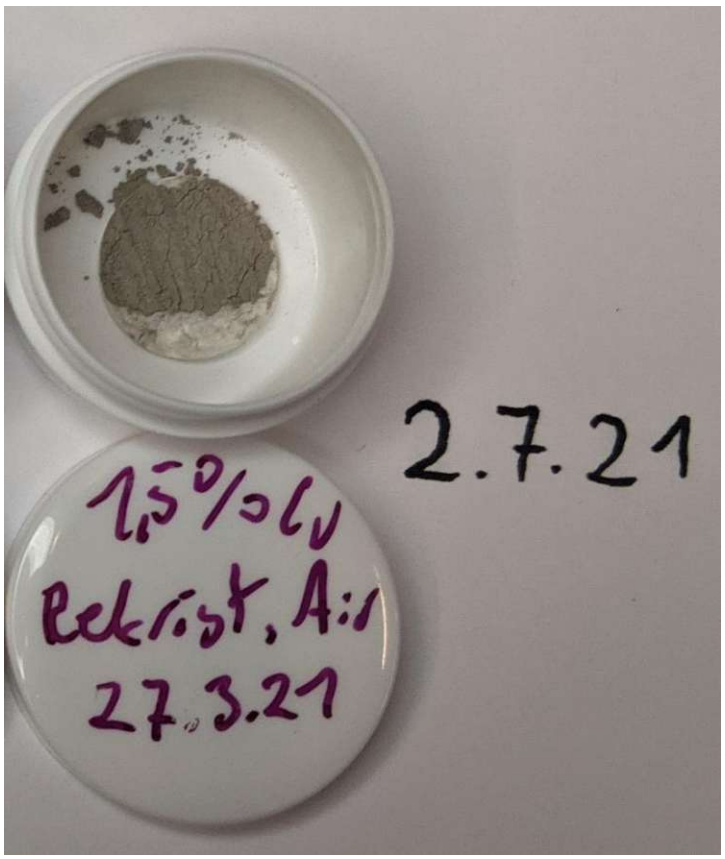

Figure 18: Corroded sample 1.5wCu+Al_2O_3_Air

4.7 Scanning Electron Microscopy (SEM)

The morphology of the samples was measured with Scanning Electron Microscopy (SEM) using a FEI Quanta 250 FEGSEM with a back-scattered electron detector. Figure 19 shows an image of the microscope.

Two samples were measured in the available measurement time. The first sample was obtained by reducing pure commercial silver oxide using the method described in chapter 3.3 “Alloy Preparation Route” and was measured immediately after reduction.

The second sample was prepared by introducing an internal standard to the pure silver metal. For this 4.50 g of the pure silver(1) oxide were combined with 0.51 g of the NIST SRM 676a Alumina standard [18] and ground with a mortar and pestle until the mixture was homogenous. This precursor mixture was then reduced using the method described in chapter 3.3 “Alloy Preparation Route” and corroded in the same way the 10wCu_NaCl sample described in chapter 4.5.1 was corroded. Figure 20 shows the samples mounted on the holder used for SEM-measurements.

Figure 19: Quanta FEG 250 Scanning Electron Microscope

Figure 20: SEM sample holder loaded with both samples. Right: pure silver, left: silver + alumina

5 Refinement

5.1 Configuration and Refined Parameters

The Rietveld refinement was configured using the following settings, which were adjusted in the HighScore Plus software for each phase:

- Background: Use Available Background (Chapter 2.5.2)
- Calculate Errors: Yes (= estimated standard deviation (ESD))
- FWHM Function: Caglioti (Chapter 2.5.4)
- Profile Function: Pearson 7 (Chapter 2.5.4)
- Asymmetry: Split width and shape (Chapter 2.5.4)

Since most measurements were performed at nonambient temperatures, the starting values of the lattice parameters of silver copper and the internal standard, if it was used, were adjusted using the predicted values calculated in chapter 6.2.3 “Starting Values for Rietveld Refinement”.

The following variables were refined in this study:

- Scale Factors (Chapter 2.5.3)
- Zero Shift (with parallel beam optics) or Specimen Displacement Errror (with BBDH optics)
- Cell parameters (Chapter 2.5.3)
- Caglioti U’s, V’s, W’s (Chapter 2.5.4)
- Peak Shape 1 & 2 (Chapter 2.5.4)

Structural parameters, such as positions of atom and occupancy factors of these positions for the different elements, were fixed during the refinements since we restricted the refinement on quantitative phase fractions. Dependent on the phase fraction, not all mentioned parameters could be refined for the individual phases due to statistical reasons.

Generally, the refinement was carried out using the following order:

1. Scale factors
2. (Specimen displacement)
3. Cell parameters
4. Scale Factors + cell parameters (+ Specimen displacement)
5. W’s
6. Scale + W’s
7. Scale + Cells + W’s

Following this routine, a good fit, represented by the minimised residuals (chapter 2.5.5 “Relevance of the Refinements”), was generally achieved. For the strong reflections, silver and in some cases copper, the rest of the parameters mentioned before were also refined until the fit did not improve anymore without diverging. The specimen displacement was only refined for measurements using BBHD optics, as parallel beam optics are independent of the specimen displacement.

5.2 Automation

The number of datasets obtained from these experiments is far outside the scope of manual refinement of each data set. The amount of work required to refine just one complex diffraction pattern with peaks exhibiting heavy overlap can in some cases already require days to achieve a reasonable fit quality. For this reason, a semi-automatic approach was chosen to refine the obtained data.

The first step in this process was to manually refine a representative diffraction pattern, usually the first or last pattern of a series, until no further improvement in the refinement could be achieved. After checking that the refinement is valid and no diverging fit or unreasonable fit parameters are observed, the resulting fit is applied to the other patterns. This is achieved by taking advantage of the “Smart Batch” functionality of High-Score Plus. [19]

The Smart-Batch consisted of 3 steps. Firstly, an automatic background is applied following Sonnefeld & Visser [14], with a granularity of 25 and a bending factor of 1. Afterwards, the diffraction pattern is cropped to the desired angle range, usually between 25 – 93° 2θ, the region most relevant reflections of this analysis are recognized. The inclusion of diffraction maxima at larger angles reduces the fit quality significantly due to instrumental effects.

By inserting all other scans from the measurement series that are similar using the insert function, this “Smart-Batch” [19] could be applied to the entire dataset at once. If the batch is configured correctly (Figure 21) this batch ignores the “Automatic Fitting Steps” and instead applies all refinement settings from the already refined diffraction pattern of the “Anchor-Scan” to the new diffraction patterns. However, in addition to copying the settings and models, the fit parameters are used as starting values for the fresh diffraction pattern and the refinement is started. This significantly speeds up the refinement process since the patterns are very similar.

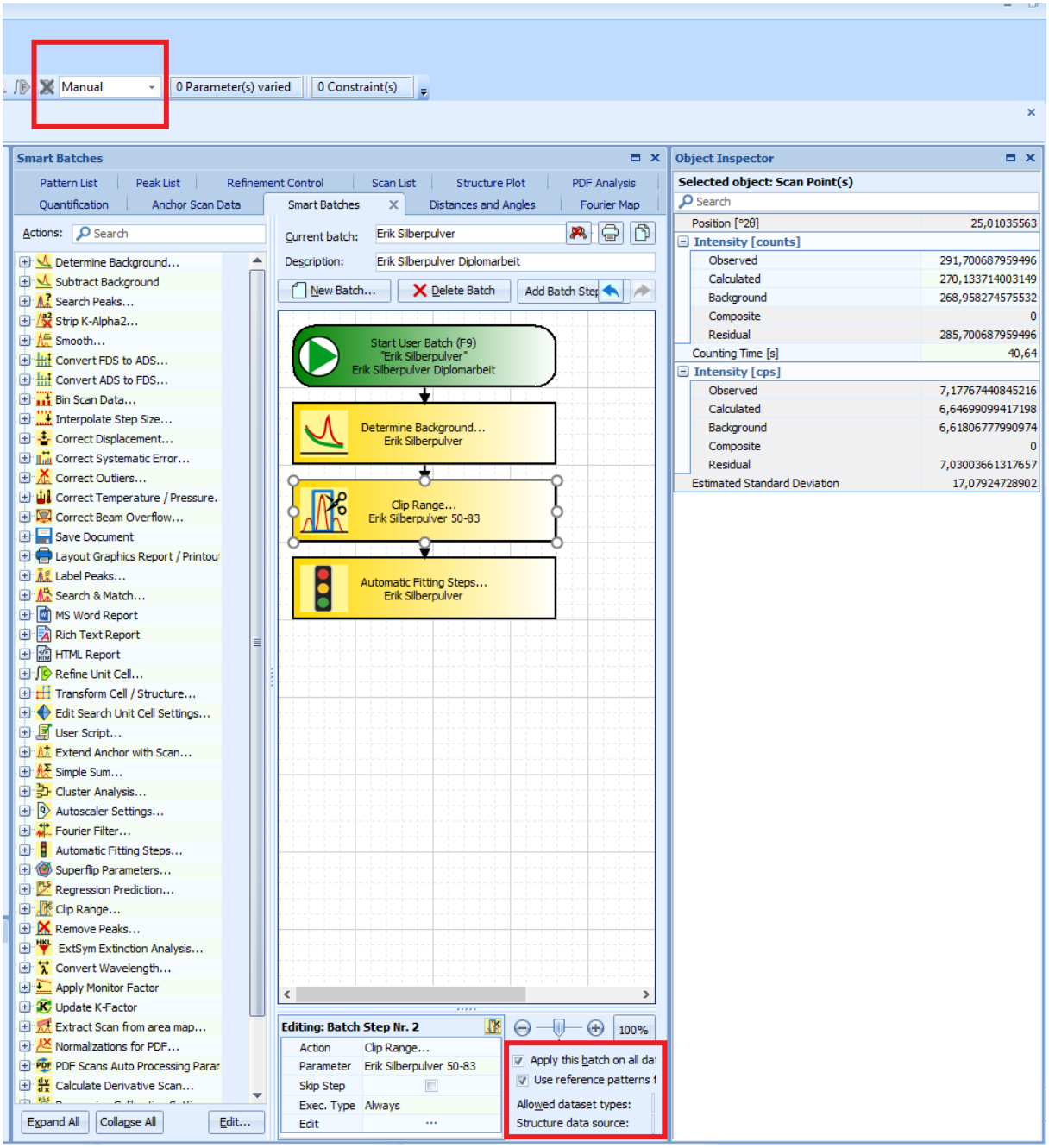

Figure 21: Settings of the "Smart-Batch" used for the semi-automation of Rietveld Refinement

In the last step each pattern of the series is checked individually, at which point the sensitive fit parameters can be refined until the refinement reaches the desired quality. For most cases, this is not necessary as the fit is already at the quality level of the first refinement. Finally, the data is extracted using a script to write a text file.

6 Data Analysis

6.1 General Information

The first step in any measurement was to compare the observed diffraction pattern with entries in the ICCD PDF4+ database [20]. Table 5 shows a list of all patterns that were found to explain the phases present in the corrosion experiments.

Table 5: List of patterns matched from the ICCD PDF-4+ database

Reference Number	Compound
04-001-2617	Silver; Ag
00-004-0836	Copper; Cu
00-045-0937	Copper(2)oxide; CuO
04-007-9767	Copper(1)oxide; Cu_2O
04-007-1400	Alumina; Al_2O_3

These patterns contain the structural information required for Rietveld refinement. Table 6 to Table 10 show the peaks listed in the reference patterns that were usually observed during the measurements. The intensities are normalized on the individual strongest reflection. It should be noted that not every peak was observed in every measurement. This is especially noticeable with the oxide species, where reflections with single digit relative intensities were only visible after the corrosion progressed almost to completion. Usually only the strongest diffractions were observable for these phases. The reference patterns also contain multiple weaker reflections that are not listed here for the same reason, since they are not discernible from the background in these measurements.

Table 6: Observed peak list of the used silver reference pattern 04-001-2617 [21]

Silver / Ag / 04-001-2617

Number	hkl	2θ (°)	Relative intensity (%)
1	1 1 1	38.119	100.00
2	2 0 0	44.305	45.2
3	2 2 0	64.4522	23.0
4	3 1 1	77.409	22.8
5	2 2 2	81.552	6.3
6	4 0 0	97.900	2.7
7	3 3 1	110.532	8.1
8	4 2 0	114.950	7.7

Table 7: Observed peak list of the used copper reference pattern 00-004-0836 [22]

Copper / Cu / 00-004-0836

Number	hkl	2θ (°)	Relative intensity (%)
1	1 1 1	43.298	100.00
2	2 0 0	50.434	46.0
3	2 2 0	74.132	20.0
4	3 1 1	89.934	17.0

Table 8: Observed peak list of the used copper (2) oxide reference pattern 00-045-0937 [23]

Copper (2) oxide / CuO / 00-045-0937

Number	hkl	2θ (°)	Relative intensity (%)
1	-1 1 0	32.497	8.0
2	-1 1 1 & 0 0 2	35.496	100.0
3	1 1 1	38.731	91.0
4	2 0 0	38.958	28.0
5	-2 0 2	48.726	20.0
6	0 2 0	53.453	6.0
7	2 0 2	58.337	9.0
8	-1 1 3	61.535	15.0
9	0 2 2	65.787	8.0
10	-3 1 1	66.250	11.0
11	1 1 3	67.945	9.0
12	-2 2 0	68.091	11.0
13	3 1 1	72.429	5.0
14	0 0 4	75.032	5.0
15	2 0 0	75.227	6.0

Table 9: Observed peak list of the used copper (1) oxide reference pattern 04-007-9767 [24]

Copper (1) oxide / Cu_2O / 04-007-9767

Number	hkl	2θ (°)	Relative intensity (%)
1	1 1 0	29.572	5.1
2	1 1 1	36.428	100.0
3	2 0 0	42.314	34.3
4	2 2 0	61.384	25.4
5	3 1 1	73.528	18.4
6	2 2 2	77.384	3.9

Table 10: Observed peak list of the used alumina reference pattern 04-007-1400 [25]

Alumina / Al_2O_3 / 04-007-1400

Number	hkl	2θ (°)	Relative intensity (%)
1	0 1 2	25.576	64.5
2	1 0 4	35.151	100.0
3	1 1 0	37.777	46.3
4	1 1 3	43.354	97.6
5	0 2 4	52.552	48.5
6	1 1 6	57.501	95.0
7	2 1 4	66.519	36.2
8	3 0 0	68.211	55.2
9	1 0 10	76.876	15.4
10	1 1 9	77.238	8.5
11	2 2 6	95.251	15.2
12	2 1 10	101.078	10.9

A common problem with the refinement was a complex preferential orientation resulting in an over- or underestimated relative intensity in comparison to the unaffected diffraction pattern. The in-situ reduction at high temperatures caused the powder to sinter slightly, which affects the orientation of the reduced metal crystallites. As a result, most measurement series exhibit some form of preferential orientation, with the {2 0 0} reflection of silver usually being much stronger than expected.

The specimen displacement error proved to be an issue here as well in the measurements using BBHD optics. This has a significant effect on the refinement, which complicates the refinement process. As a result, it reduces the significance of the results. Including the internal standard helps with the specimen displacement. However, most measurements using BBHD optics did not include the standard.

Finally, because it is neither practical nor sensible to depict every single measured diffraction pattern of a measurement series, only the first and last measurement of the corrosion, as well as a representative or notable measurement from the series are shown here. The full raw data can be accessed in the data repository linked in the attachments.

6.2 Calibration

6.2.1 Prepared Ag_2O

The synthesised silver oxide was measured using X-ray diffraction to analyse the phase contents of the resulting powder.

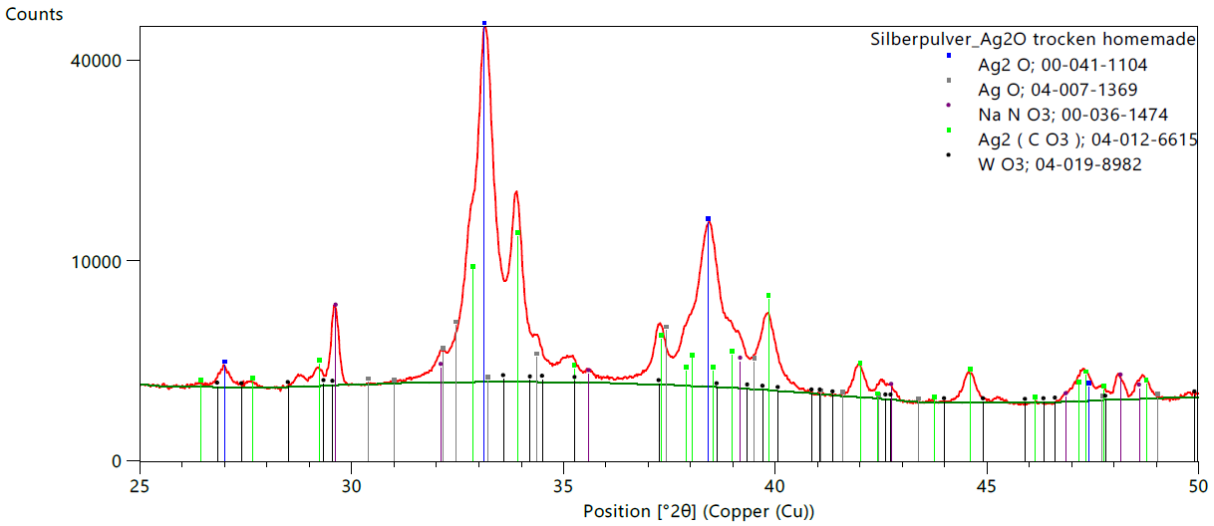

Figure 22: XRD-pattern of the prepared silver oxide mixture with matched phases

This analysis showed that the prepared powder was impure, as expected. Multiple silver species, namely Ag_2O, AgO, as well as Ag_2CO_3 were found. The silver oxides were expected to form and silver carbonate formed from the reaction of carbon dioxide with remaining sodium hydroxide, following Equations 15 - 17. Besides those, there were two impurities. Namely $NaNO_3$, which is a product in the reaction depicted in Equation 13, and WO_3 which was introduced during the grinding in a tungsten carbide crucible, where a thin layer of oxide forms on the surface of the crucible.

$$CO_2 + H_2O \rightarrow H_2CO_3 \quad (15)$$

$$H_2CO_3 + 2\,NaOH \rightarrow Na_2CO_3 + 2\,H_2O \quad (16)$$

$$Na_2CO_3 + 2\,AgNO_3 \rightarrow Ag_2CO_3 + 2\,NaNO_3 \quad (17)$$

It should be noted that the presence of sodium nitrate is acceptable, as it was an additive in some of the prepared silver inks and caused heavy damage to the parchment in the artificially aged samples (chapter 2.2). The different silver species all get reduced during the treatment with hydrogen and the measured tungsten oxide is a very small amount, because the electron dense tungsten exhibits strong x-ray diffraction lines.

6.2.2 Non-ambient Temperatures

As mentioned before, a change in temperature influences the crystal structure, which usually expands with rising temperature. The former is important for X-ray diffraction experiments because the observed peak position is dependent on the lattice. This expansion was calibrated by refining the diffraction pattern of pure silver and pure copper mixed with alumina as an internal standard measured at different temperatures. These measurements were described in Chapter 4.3 “Calibration of Lattice Parameters”. Figure 23 shows a sample fit of the temperature calibration series.

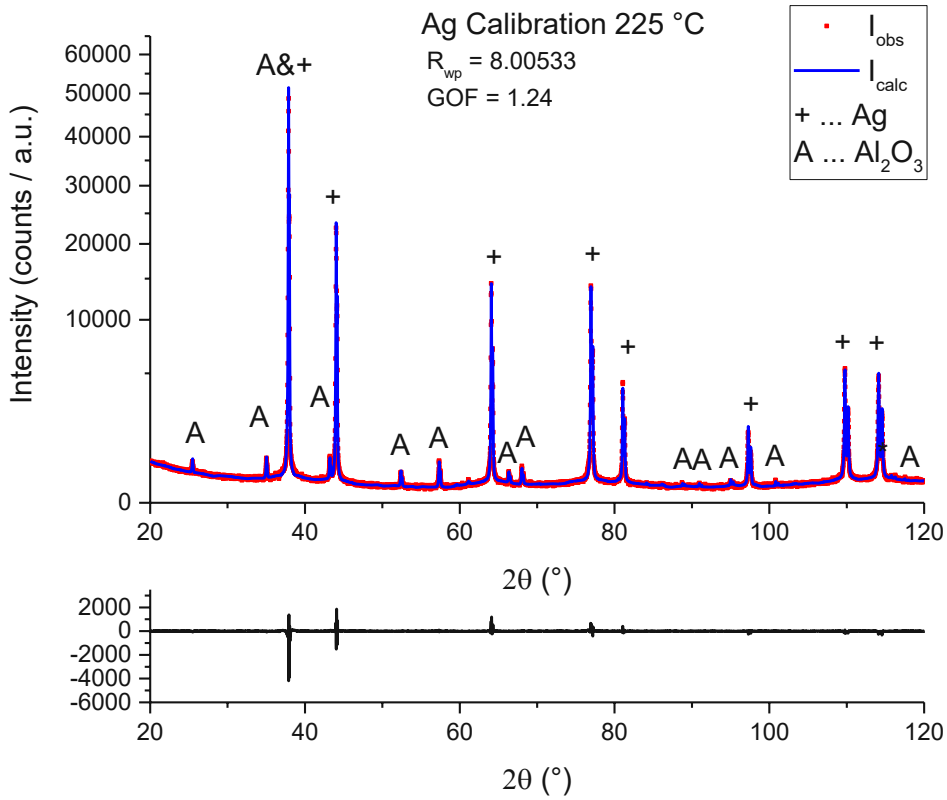

Figure 23: Sample Fit of the calibration of lattice parameters of silver metal with alumina, taken at 225 °C with a GOF of 1.24

The refined phases are depicted in Table 11, together with the weight fractions calculated by the refinement. It should be noted that these weight fractions are for the crystalline content of the sample and are not calibrated for the amorphous content. The error is given in a bracket behind the number and represents the estimated standard deviation of the last digit.

Table 11: Refined phases for the calibration of the lattice parameters of silver and copper at non-ambient temperatures

PDF 4+ DBN	Chemical Formula	Crystal System	Space Group	Weight fraction (w%)
04-001-2617	Ag	Cubic	Fm-3m	83.1(3)
04-007-1400	Al2O3	Rhombohedral	R-3c	16.9(2)
00-004-0836	Cu	Cubic	Fm-3m	81.97(8)
04-007-1400	Al2O3	Rhombohedral	R-3c	18.03(5)

After refining every temperature for both silver and copper, the resulting lattice parameters were plotted against the temperature and depicted in Figure 24 and Figure 25. A linear dependence on the temperature can be observed in the measured temperature range of 25 – 375 °C.

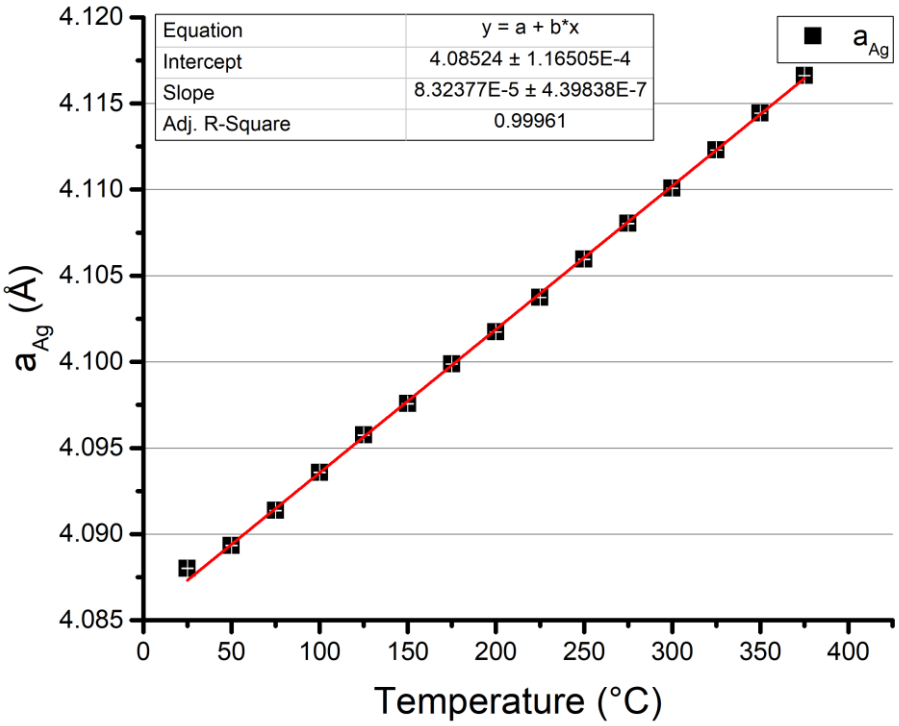

Figure 24: Refined lattice parameter of pure silver metal against the temperature with a linear fit

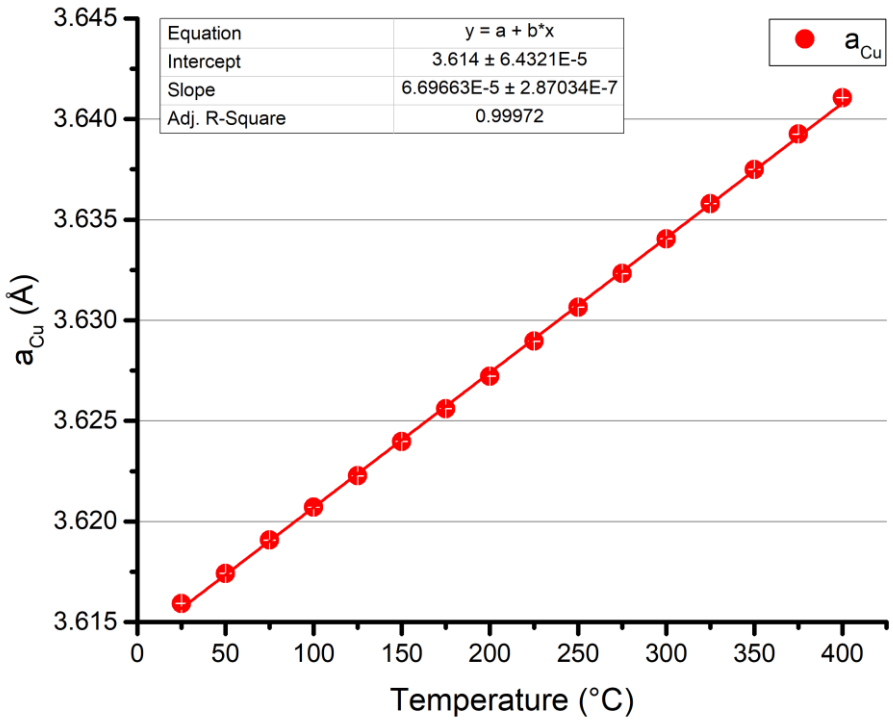

Figure 25: Refined lattice parameter of pure copper metal against the temperature with a linear fit

To create a model of the lattice expansion with the temperature, the linear dependence in this temperature range was fitted using a linear curve fit, which is depicted in the top left of each figure. This linear model describes the lattice parameters in dependence of the observed temperatures with reasonable significance. Note that the error bars of the data points are depicted in white to visualize them.

6.2.3 Starting Values for Rietveld Refinement

By combining Vegard's law for both calibrations of the lattice parameters with temperature, a model of the lattice parameter, which is dependent on both copper content and temperature, was obtained. The model can be described as shown in equation 18:

$$a_{AgCu}(x_{Ag}, T) = x_{Ag} * (k_{Ag} * T + d_{Ag}) + (1 - x_{Ag}) * (k_{Cu} * T + d_{Cu}) \quad (18)$$

a …… Lattice parameter a
x …… Molar fraction
T …… Temperature
k …… Slope of the linear fit from chapter 6.2.2
d …… Intercept of the linear fit from chapter 6.2.2
Indexed:
AgCu …… Alloy of Silver and Copper with a composition of $Ag_xCu_{(1-x)}$
Ag …… Pure silver metal
Cu …… Pure copper metal

This procedure, which obtains starting values for the refinement process, is very useful. By including the temperature of the measurement as well as the expected composition, the model results in lattice parameters already very close to the final result, and therefore helps to speed up the refinement.

Furthermore, the composition of the solid solution can also be approximated from the refined lattice parameter. However, this model is far from perfect. The Ag-Cu system follows Vegard's law closely, but not exactly, meaning that the calculated composition is only an approximation. Moreover, the lattice parameters obtained for the segregated species are larger than the measured lattice parameters of pure silver. This would result in a negative copper content, and hence exhibits the model's limit since there cannot be a negative amount of copper in the crystal structure.

6.3 Scanning Electron Microscopy Images

6.3.1 Pure Silver Metal

The SEM measurements offered insights into the morphology and characteristics of the prepared metal powder.

Figure 26 shows a 150 times magnified picture of the sample on the sample holder. Here the round shape of the XRD-Sample holder is still visible. Denser areas alternating with more porous areas can be observed, which are marked in Figure 26.

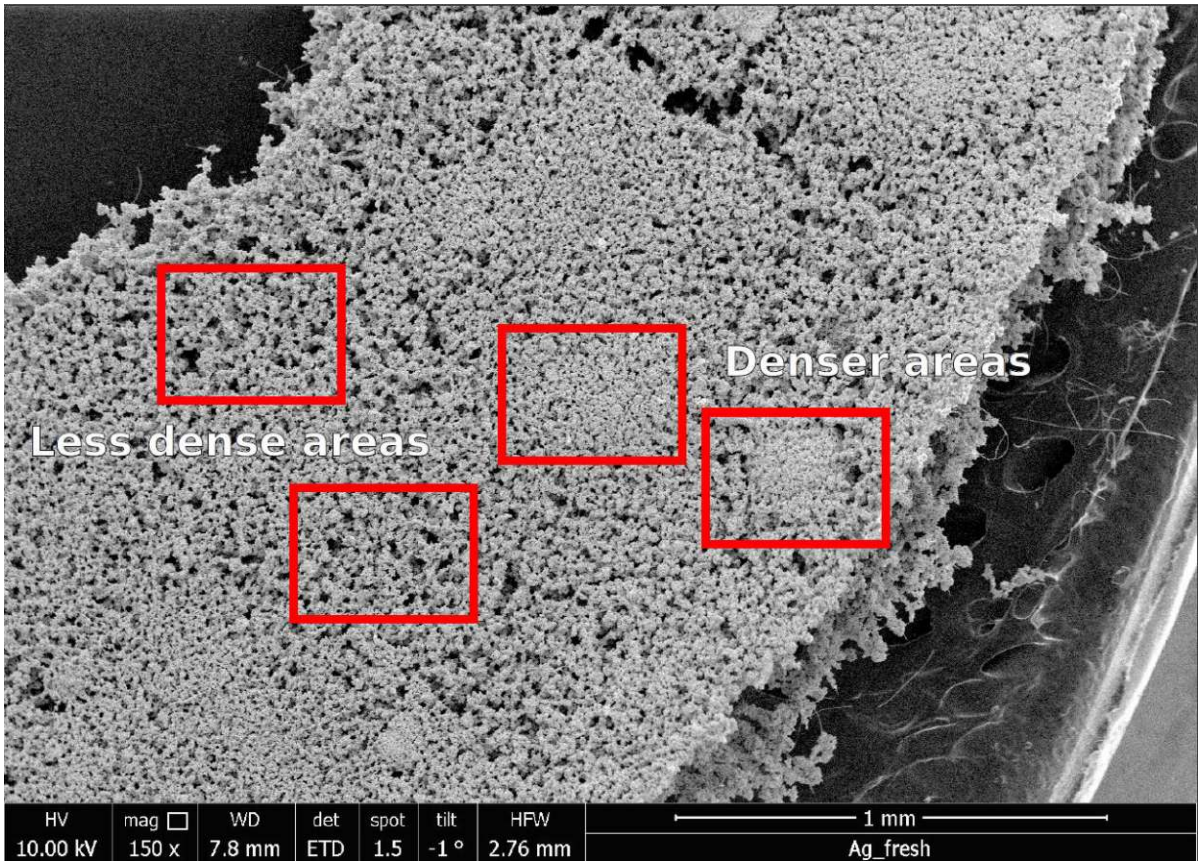

Figure 26: SEM Image of pure Silver directly after the reduction step at 150x magnification.

Zooming in to 600 times magnification in Figure 27 the porous structure is recognisable even better. This structure is comparable to a metal sponge. At this magnification, some bigger fragments of silver metal are visible.

Two areas of interest marked in Figure 27 were investigated in more detail, an area of high porosity, and a more compact piece of silver, respectively.

At 5000 times magnification in Figure 28, it is confirmed that the in-situ reduction does not produce a traditional powder consisting of separate particles, but rather a scaffold of sintered particles, as marked in Figure 28.

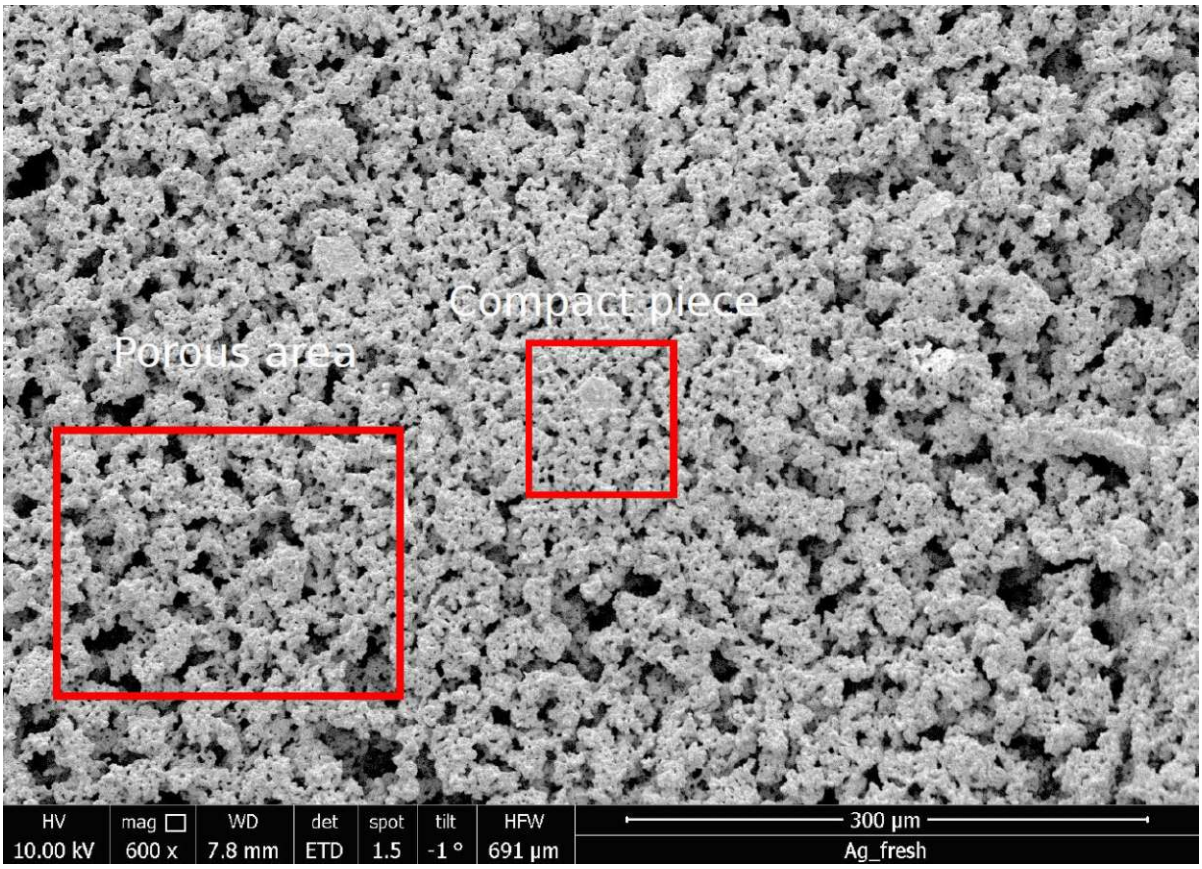

Figure 27: SEM image of pure silver directly after the reduction step at 600x magnification

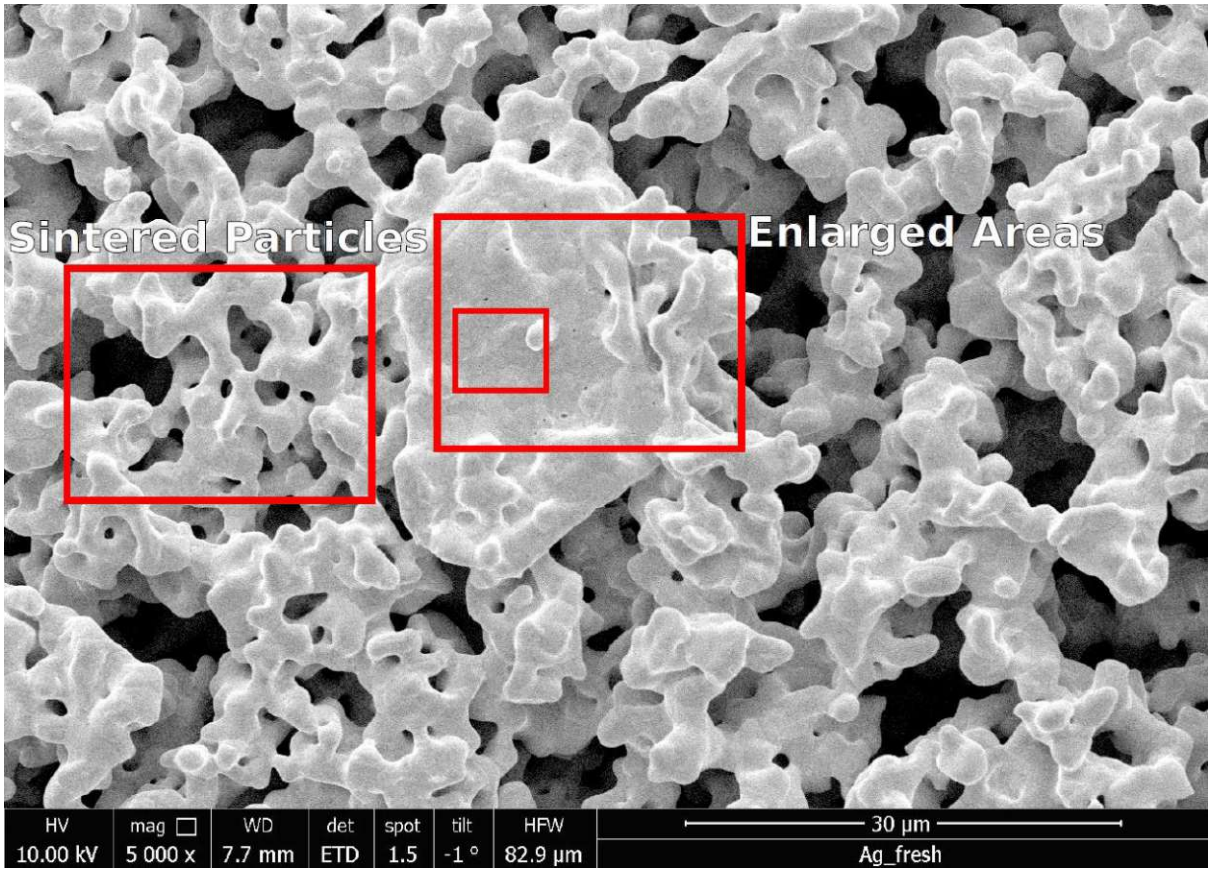

Figure 28: SEM image of pure silver directly after the reduction step at 5000x magnification, centred at a bigger piece.

Enlarging the marked area of the bigger piece to 20k magnification in Figure 29, grain boundaries become visible, with black spots in some of these. These black spots in the image probably represent remaining pores left by particles fusing together during the reduction step.

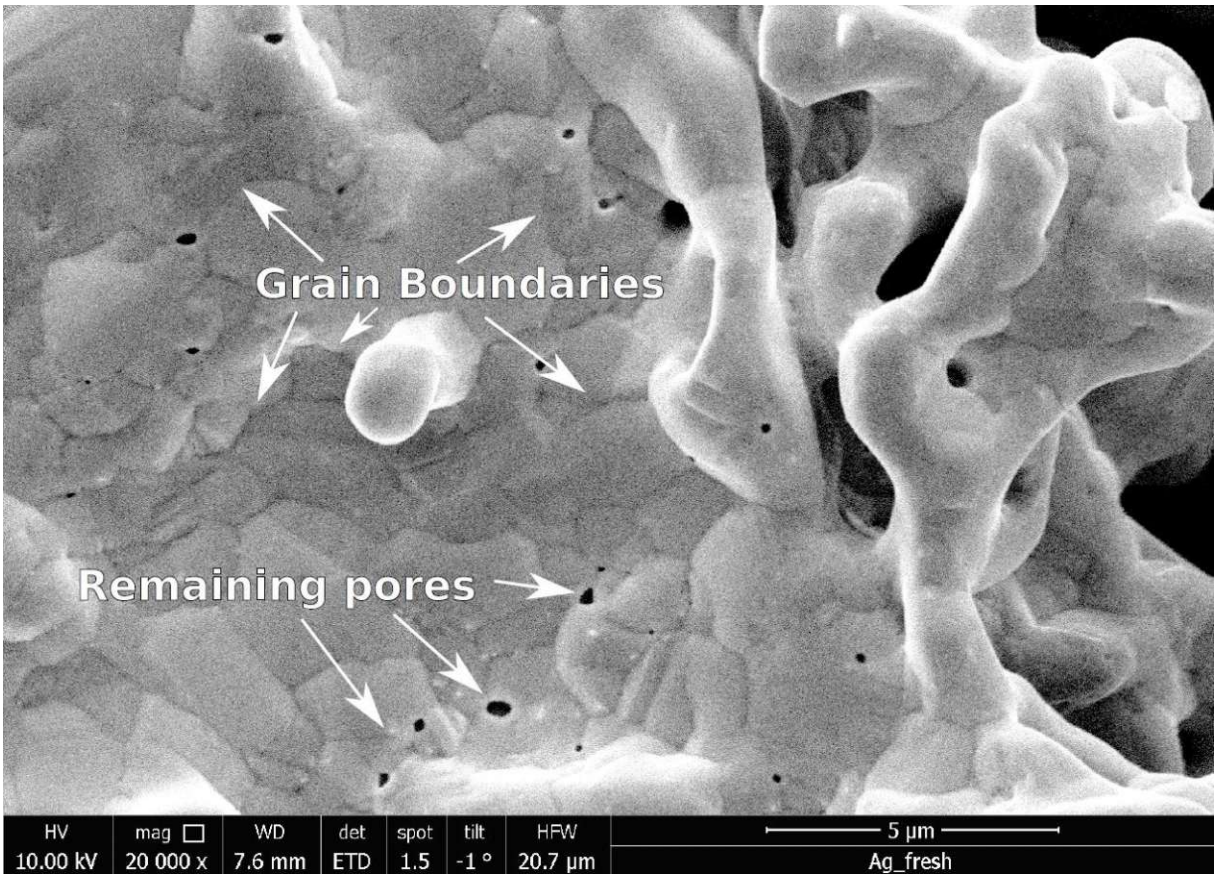

Figure 29: SEM image of pure silver directly after the reduction step at 20000x magnification, centred on a bigger piece.

The size of these grains was measured at 80k magnification in Figure 30 in the smaller area marked in Figure 28. In this more compact area, the grain size seems to be spread around 1 µm diameter, with some parts being significantly smaller and some being significantly larger.

The second spot marked in Figure 27 was also measured at a higher magnification, to consider the properties of the sample in the more porous areas. Figure 31 shows one of these areas at 5000 times magnification. Here the massive surface area of the prepared sample, as well as a deep pore structure is recognisable.

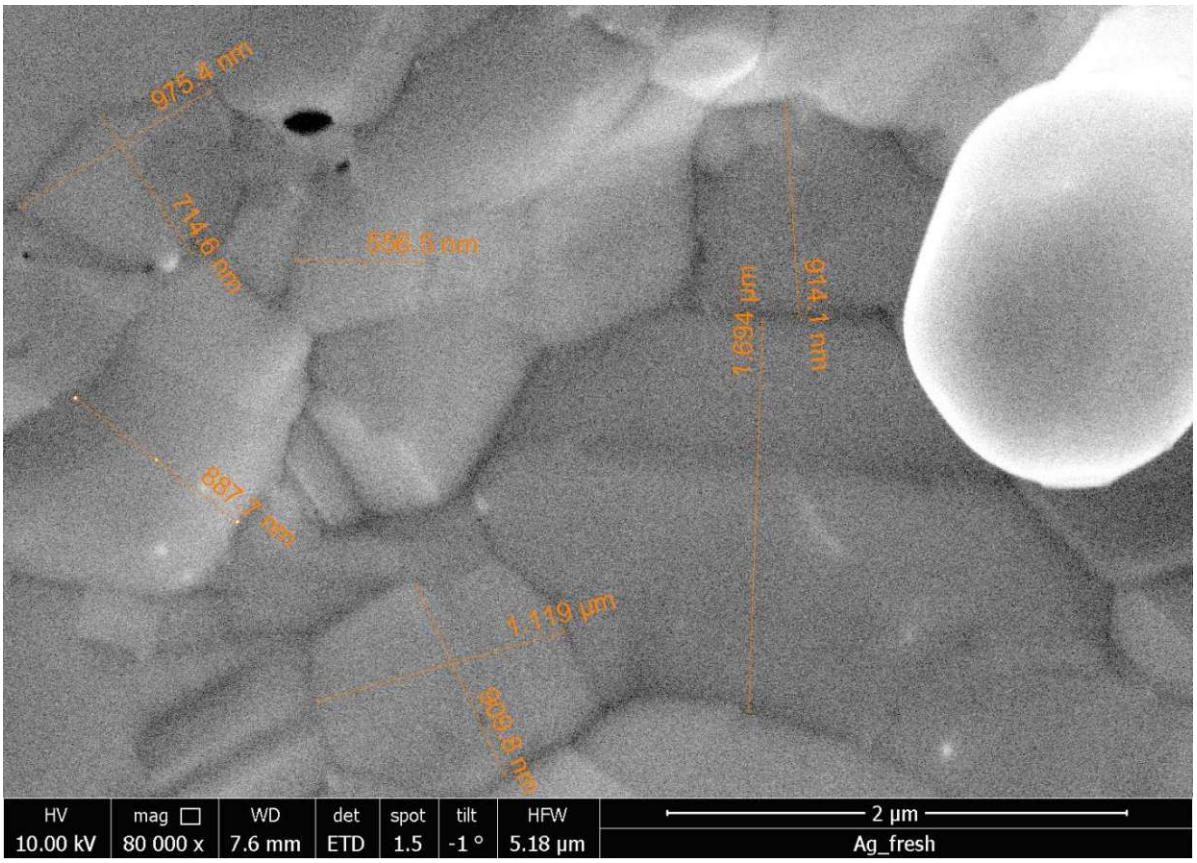

Figure 30: SEM image of pure silver directly after the reduction step at 80000x magnification, centred on a bigger piece.

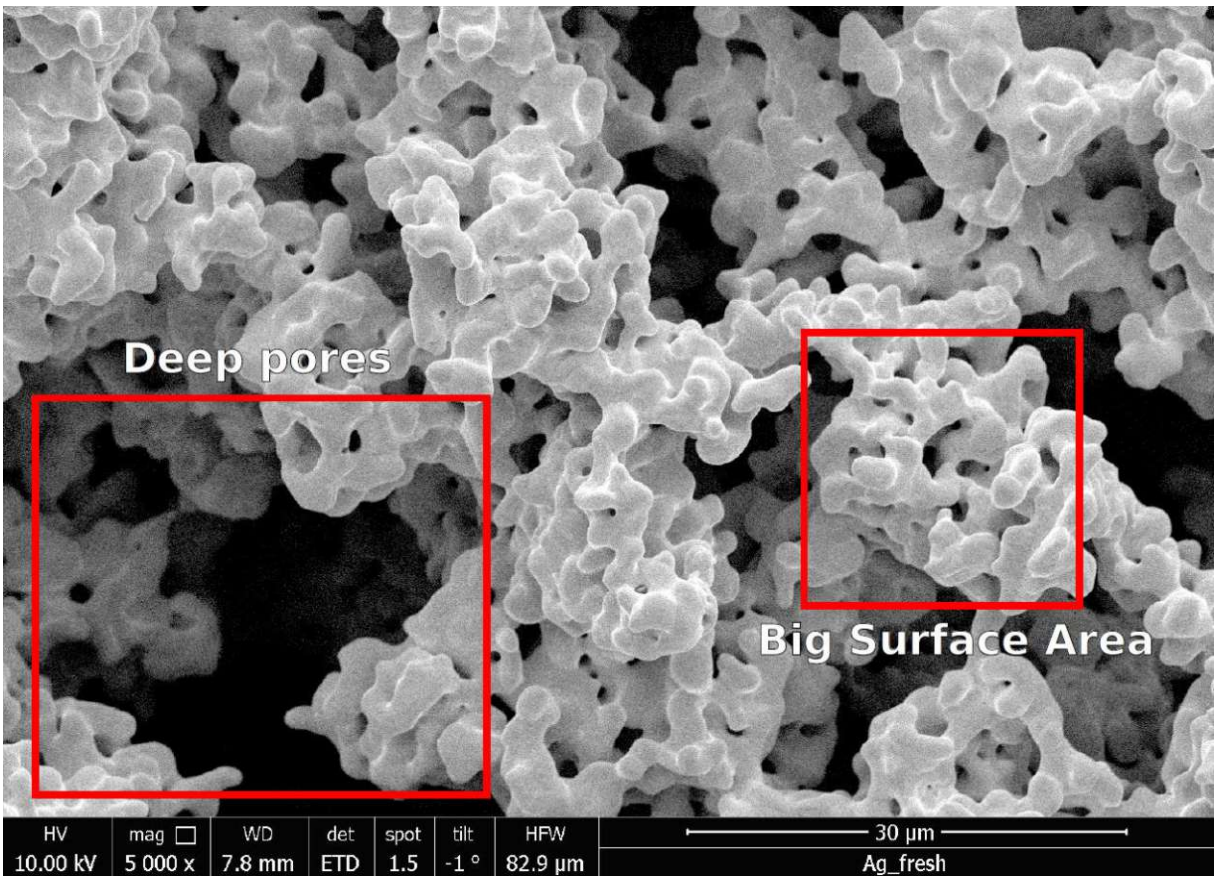

Figure 31: SEM image of pure silver directly after the reduction step at 80000x magnification, centred on a porous area.

At 40k magnification the grain boundaries become visible again, as seen in Figure 32. In this image the contrast was increased, which revealed bright parts on the surface of the silver, marked using red arrows. The size of these particles was measured at 320k magnification to be in the nanometre size range, as seen in Figure 33.

Because a back-scattered electron detector was used, the bright spots are caused by a material denser than silver. The source of these particles is most likely a lead impurity. The commercial silver oxide contains a 3 parts per million (ppm) impurity of lead [26], which was also reduced during the reduction process. The reduction temperature of 500 °C is above the melting point of lead [27], which consequently melted and collected at the surface as nanometre sized droplets. Since this impurity is present in the ppm range, it is not visible in the laboratory XRD data due the small weight fraction.

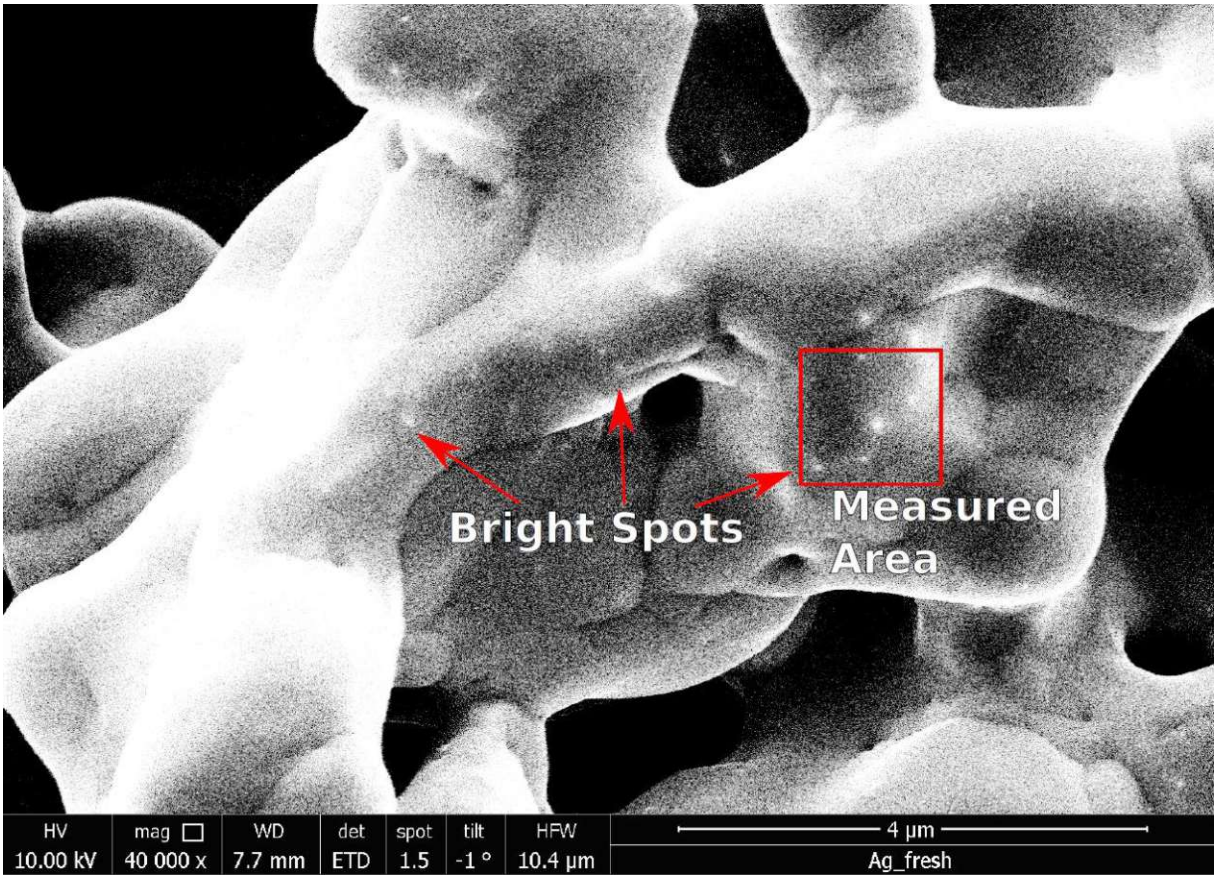

Figure 32: SEM image of pure silver directly after the reduction step at 80000x magnification, centred on a porous area.

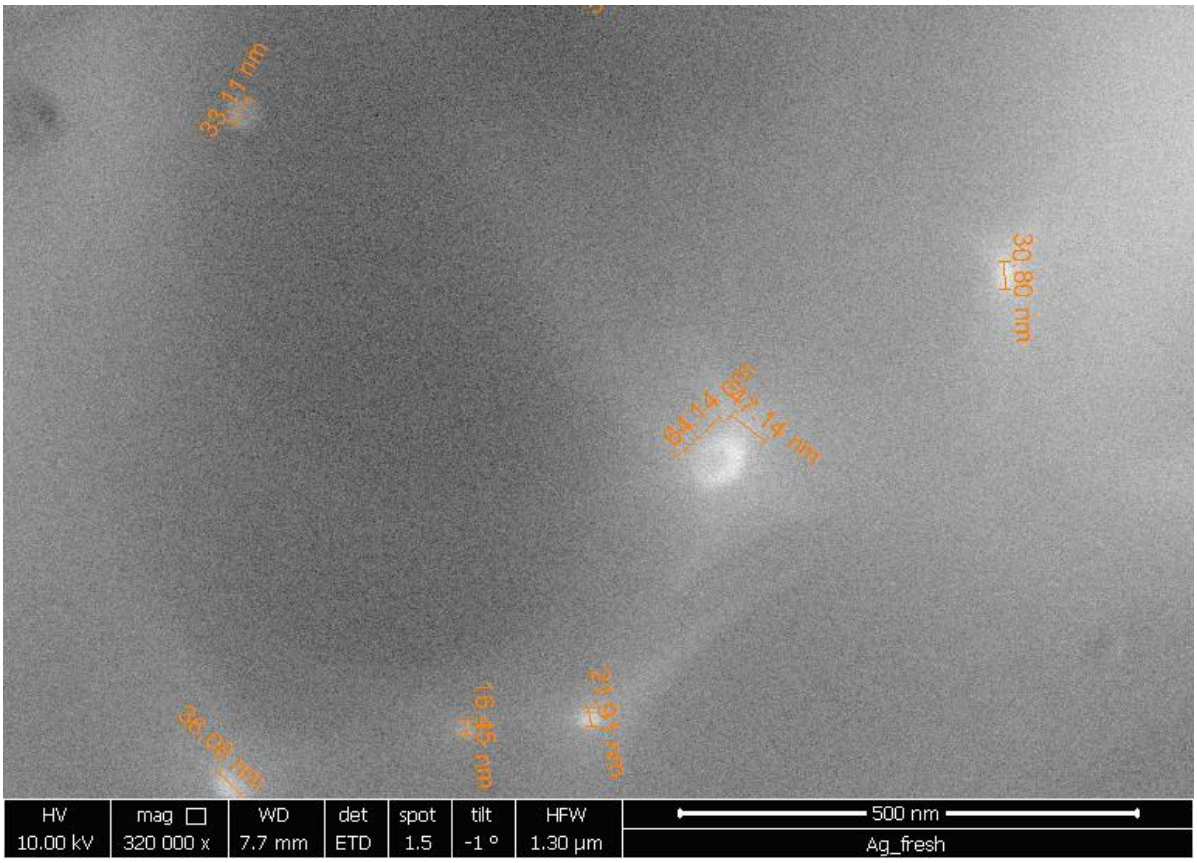

Figure 33: SEM image of pure silver directly after the reduction step at 320000x magnification, centred on a porous area.

6.3.2 Silver Metal with added Alumina

A second sample was measured using scanning electron microscopy in the same setup. This sample contains the internal alumina standard and was corroded with pressurized air and brine spray. These SEM-Measurements were performed 10 days after the corrosion finished. The preparation is described in chapter 4.7 “Scanning Electron Microscopy (SEM)”.

It was found that the addition of the internal standard causes significant differences in the sample morphology. Figure 34 shows the sample at a magnification of 20000x.

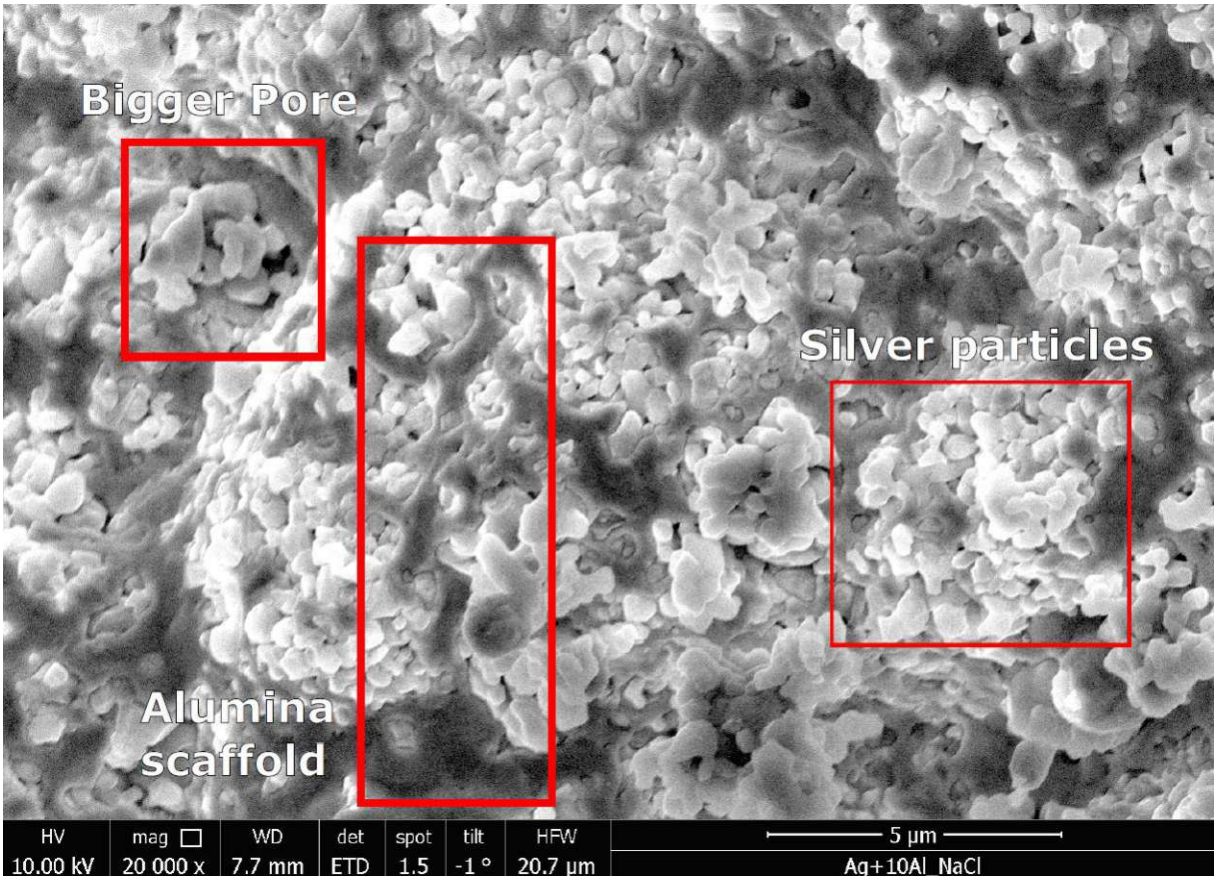

Figure 34: SEM image of pure silver with added alumina, 10 days after the corrosion, at 20000x magnification

The added alumina, which appears darker because it is less dense and a back-scattered electron detector is used, seems to offer a scaffold in which the silver particles are embedded. This prevents the silver particles from sintering together during the reduction to form a connected structure, contrary to what is observed in the pure silver. This seems to have resulted in more traditional particle shapes when compared to the pure silver, where the edges of the particles are rounded in almost all cases. The porosity and surface area of the silver phase in the sample also seems much lower than in the measured pure silver sample, since visible pores are rarer. There are no visible corrosion phenomena present.

Figure 35 shows the silver sample with alumina at a magnification of 40000x with the size range of the silver particles measured. This analysis showed that the particle size of silver is about half the observed particle size in pure silver (see Figure 30).

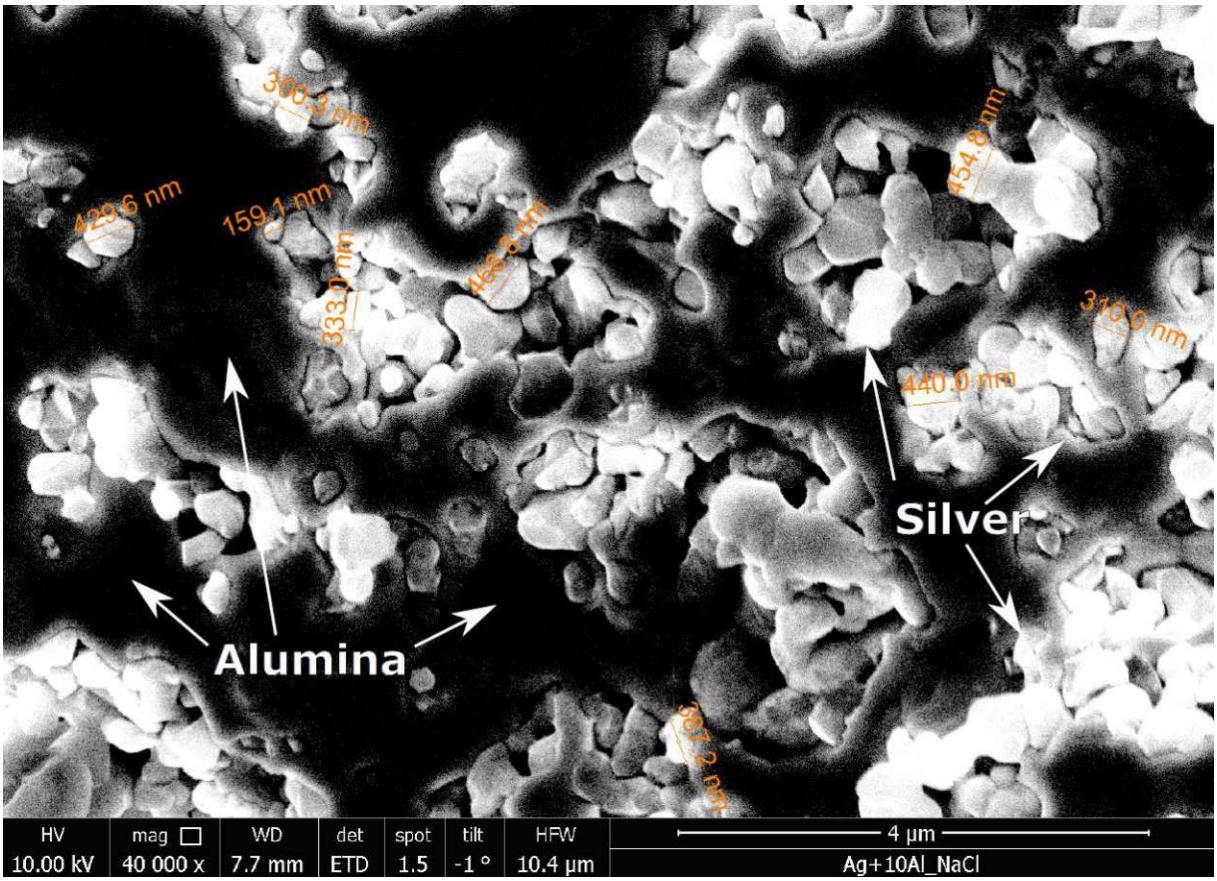

Figure 35: SEM image of pure silver with added alumina, 10 days after the corrosion, at 40000x magnification

These measurements show that the addition of the standard causes significant differences of the morphology of the samples. However, these differences might not be obvious in the PXRD measurements. Particle size has effects on the XRD measurements, which the peak width is dependent on, and a preferential orientation can cause differences in the observed intensities of some reflections. However, both these effects are small and can be indistinguishable from statistical uncertainties in some cases. These effects should be considered when assessing observed results of the corrosion and segregation discussed in the following chapters.

6.4 Temperature Variation Series

The series was investigated as a preliminary experiment to test the sample preparation route described in chapter 3.3 “Alloy Preparation Route” and used the synthesised silver oxide as the silver source in the precursor mixture. As discussed in the previous chapter 6.2.1, this silver oxide mixture is impure and contains other silver species, as well nitrates and traces of tungsten oxide. As a result, the weight fractions of elements in the prepared alloy are not known precisely.

While multiple series were performed, only the two most important series will be presented here, as these represent the two different routes of corrosion products that were observed. The first is the sample corroded at 25 °C using air and brine. Figure 36 and Figure 37 show the final diffraction measurement taken after 17 hours with the matched phases. The figure was split in two to provide better readability.

Eight different phases were found in this corrosion experiment (see Table 12). The composition was estimated from the observed diffraction intensities and grouped in one of three categories: “++” was used for the main phase, “+” for components present in significant proportions and “-“ was used for trace components.

The presence of crystalline NaCl proves that brine spray does indeed reach the reaction chamber and is deposited on the sample. The tungsten impurity present in the precursor mixture reacted as well to form two different phases. There are no silver corrosion products present, besides the species that formed with the tungsten impurity. Copper did partly corrode however to form both copper(1) oxide Cu_2O and copper(2) oxide CuO. Moreover traces of copper(1) chloride CuCl can be observed.

Another effect that can be spotted is the specimen displacement, which causes a shift in the observed peak positions, which gets more pronounced at higher angles because the observed $\Delta\theta$ is dependent on the value of θ.

Table 12: Identified phases in the corrosion experiment at 25 °C of the temperature variation series

PDF 4+ DBN	Chemical Formula	Crystal System	Space Group	Estimated quantity
04-001-2617	Ag	Cubic	Fm-3m	++
00-004-0836	Cu	Cubic	Fm-3m	+
00-045-0937	CuO	Monoclinic	C2/c	+
04-007-9767	Cu_2O	Cubic	Pn-3m	-
04-007-3879	CuCl	Cubic	F-43m	-
01-070-2509	NaCl	Cubic	Fm-3m	-
01-084-2722	Ag_2WO_4	Orthorhombic	Pn2n	-
04-007-5006	WO_3	Monoclinic	P21/c	-

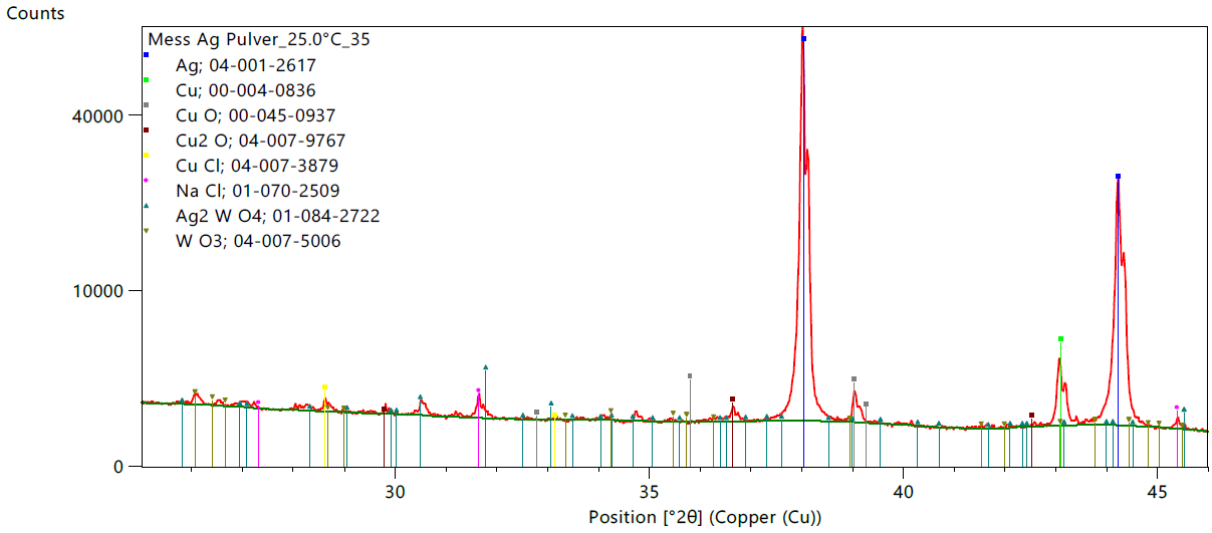

Figure 36: Phase analysis of the temperature variation series after 17 hours or corrosion at 25 °C between 25 and 46 °2ϑ

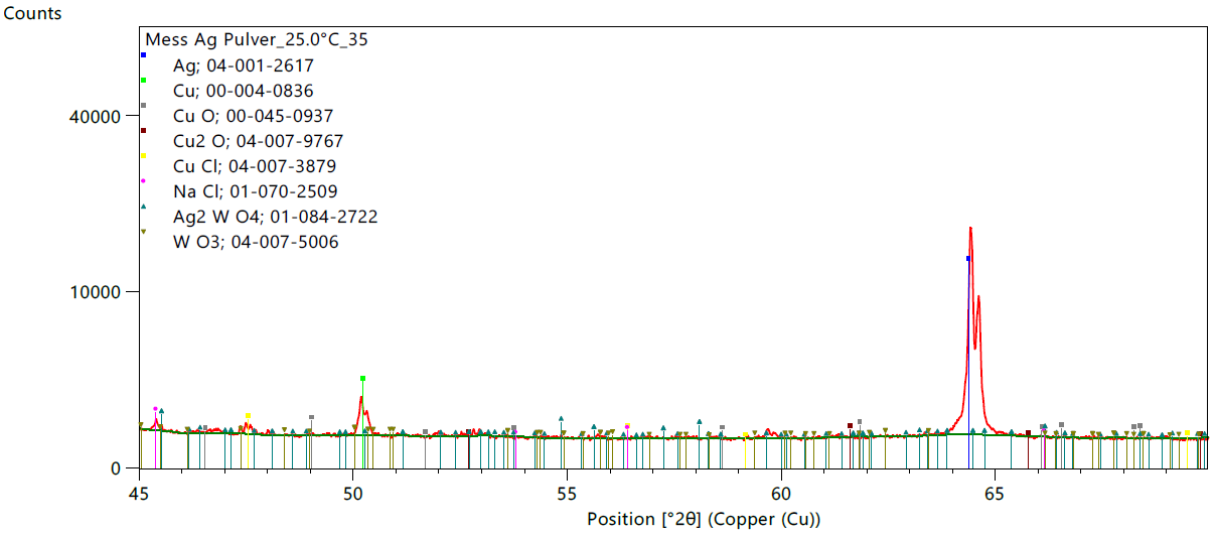

Figure 37: Phase analysis of the temperature variation series after 17 hours of corrosion at 25 °C between 45 and 75 °2ϑ

The second series which is presented here was measured at 275°C and corroded using air and brine (Table 4). Figure 38 and Figure 39 show the final diffraction pattern taken after 17.5 hours of corrosion, with the matched phases depicted in Table 13. This figure was spit in two as well to provide better readability.

Table 13: Identified phases in the corrosion experiment at 275 °C of the temperature variation series

PDF 4+ DBN	Chemical Formula	Crystal System	Space Group	Estimated quantity
04-001-2617	Ag	Cubic	Fm-3m	++
00-045-0937	CuO	Monoclinic	C2/c	+
04-007-9767	Cu_2O	Cubic	Pn-3m	+
04-007-3879	CuCl	Cubic	F-43m	-
04-005-5745	W_8O_{21}	Orthorhombic	Pbam	-

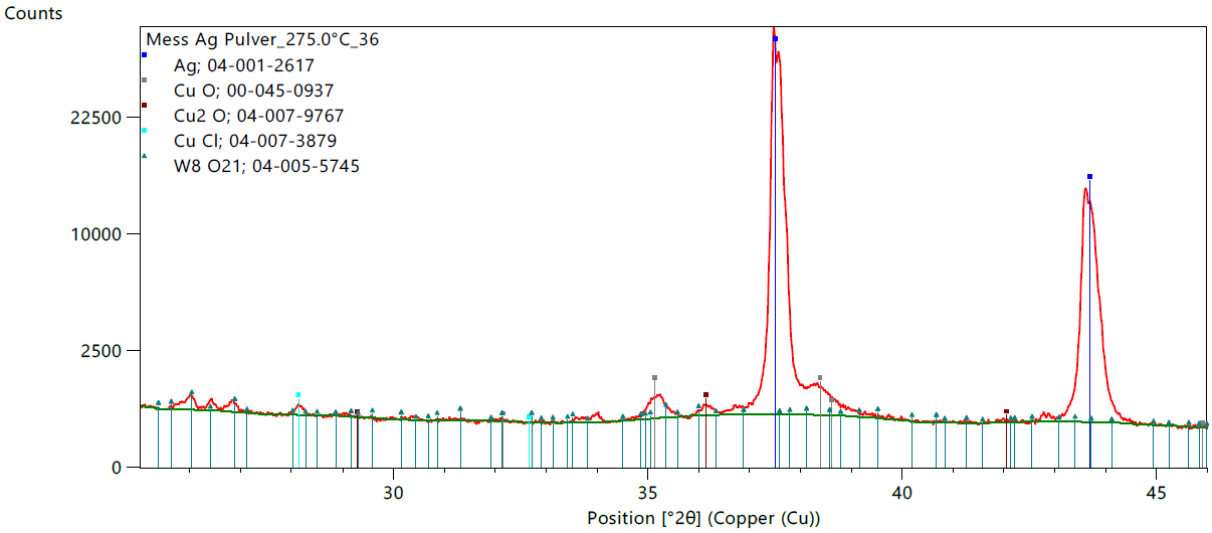

Figure 38: Phase analysis of the temperature variation series after 17.5 hours of corrosion at 275 °C between 25 and 46 °2ϑ.

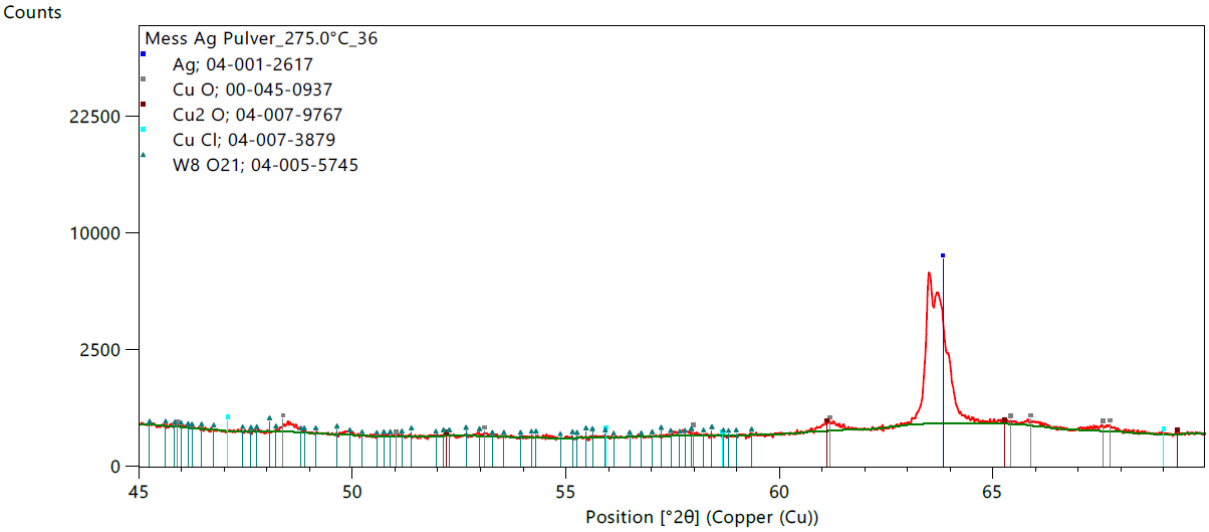

Figure 39: Phase analysis of the temperature variation series after 17.5 hours of corrosion at 275 °C between 45 and 75 °2ϑ

There are pronounced differences observed between the series measured at 275 °C and 25 °C. At higher temperatures only five phases were present in the sample. Cu, NaCl, WO_3 and Ag_2WO_4 were present only at 25 °C and W_4O_{21} only present at 275 °C. The metallic copper corroded completely to form both copper(1)- and copper(2) oxides, as well as traces of copper(1) chloride. There was no crystalline NaCl present. This can be explained by the elevated temperatures of 275 °C in the reaction chamber. At this temperature the brine spray is rapidly vaporized when entering the reaction chamber, which prevents the formation of crystalline sodium chloride. The tungsten impurity formed a different oxide compared to the corrosion at 25 °C. There are no silver corrosion products. However, a reaction happening to the silver is observed in the silver reflections, which shift to smaller angles by less than one degree θ. This change is pictured in Figure 60 is explored further in the corresponding chapter 6.7 “Oxygen induced segregation”.

These results did not match with the results that were assumed from the preliminary research of the artificial parchment samples and ageing, where silver(1) oxide Ag_2O, silver(1) chloride AgCl, as well as copper(2) chloride were found as corrosion products. It was hoped that the combination of brine spray and traces of nitrates present in the sample resulted in similar, or any, silver corrosion products as observed on the parchment samples. Further experiments need to be performed to explain the absence of silver corrosion products.

Unfortunately, this measurement series proved impossible to refine in a reasonable way, due to issues caused by the specimen displacement error, as well as the large number of phases present in these samples.

The most important results of this study are that the preparation route produces a sample which fulfils the requirements to perform these experiments, the observed reaction happening to the silver at temperatures above 200 °C, where the silver reflections shift to lower angles, and the fact that brine spray does indeed reach the sample. After these results pure silver(1) oxide was acquired commercially for the following experiments.

6.5 10 w% Copper Alloys / 10wCu Series

Following the results of the T-variation series (Table 4) the observed peak shift of silver was investigated further. For these experiments clean silver(1) oxide was used instead of the synthesized silver oxide and -carbonate mixture.

Three samples were prepared for this series and exposed to different atmospheres. One was corroded with air and brine spray, the next one was corroded with air only and the final one was prepared after further homogenisation of the precursor mixture and corroded with only air as well. The oxygen content of this last sample was also measured by thermal decomposition and detecting the contained oxygen using infrared radiation, as described in 4.5.2 “Oxygen Content Analysis”. All the corrosion measurements of these series were done at a temperature of 275 °C. Parallel beam optics were used to avoid a shift of the peak positions due to a specimen displacement.

6.5.1 10 w% Cu Alloy corroded with Air / 10wCu Air

Figure 40 shows the first corrosion measurement of the series at 275 °C, in which the alloy was only corroded with air. The phase analysis resulted in silver, copper and copper(1) oxide (Table 14). Comparing it to Figure 41, which shows the corrosion measurement after 18h corrosion time at a temperature of 275 °C, it is visible that most of the metallic copper corroded. This formed both copper(1) oxide and copper(2) oxide as separate phases. Additionally, the silver diffractions shifted to the left during the corrosion process, as predicted by the rule of Vegard. The second reflection of silver shifted from 44.0546 °2θ at the start of the corrosion to 43.9053 °2θ, which is a shift of 0.1493 °2θ. However, the lattice parameter that was refined for the silver phase after the shift is larger than the lattice measured of pure silver from the calibration. This is explored further in chapter 6.7 “Oxygen induced segregation”.

Another effect that can be noticed is the silver reflections becoming lopsided at higher angles. This is caused by the peak shift of the silver reflections. This is a result of the fact that the reaction keeps happening while the measurement is running. Because the reaction does not stop, by the time the detector has reached higher angles the sample has already changed. Because of this, diffractions at higher angles represent the measurement at a slightly later point of the reaction progress compared to the diffractions at lower angles. This is especially pronounced in this series because the segregation happened at a very high speed. As a result, in the time required to measure from 38° to 80° 2θ the segregation shifted the silver diffractions noticeably to the left. This is also a reason for the lower fit quality of the first measurement compared to the last, in this series the sample changed quickly during the first measurement.

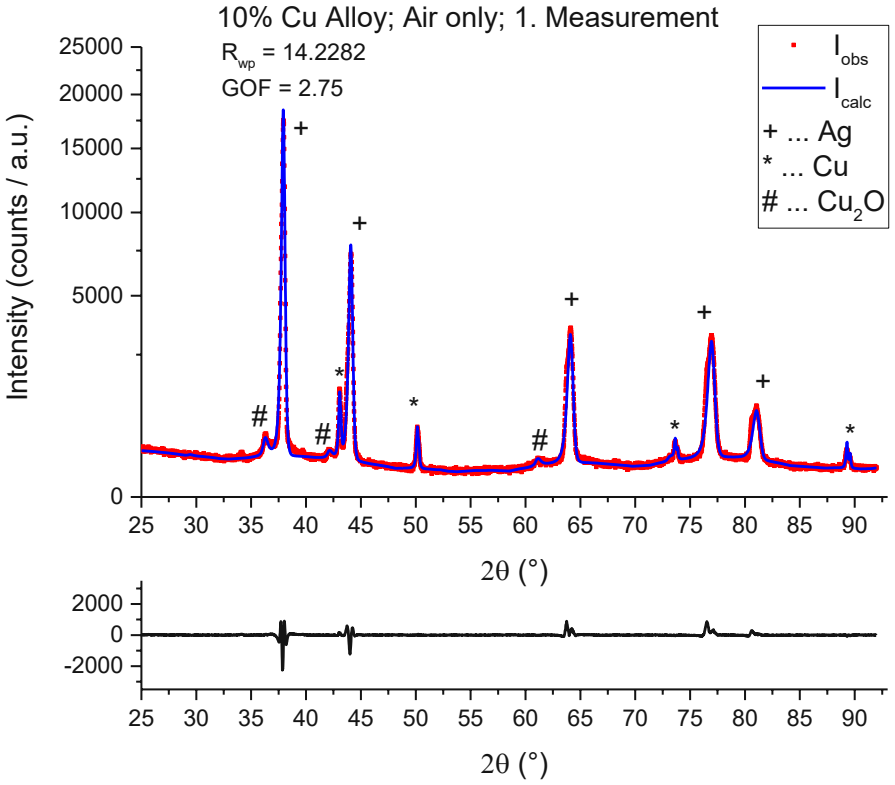

Figure 40: Refined XRD data of the 10wCu_Air corrosion series at the start of corrosion

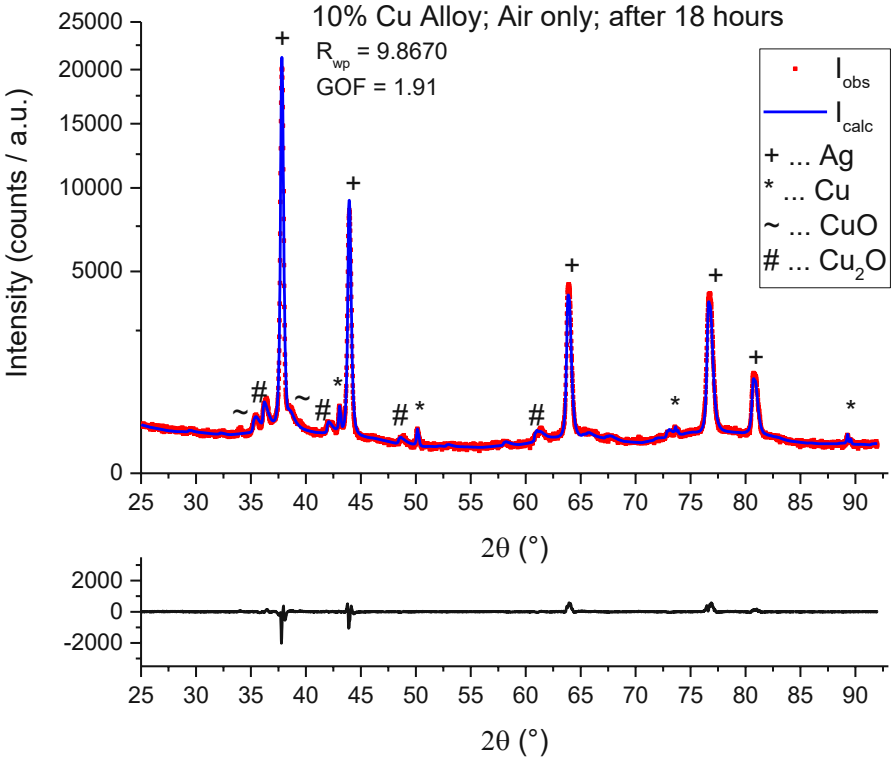

Figure 41: Refined XRD data of the 10wCu_Air series after 18 hours of corrosion

Table 14: Refined phases of the 10wCu_Air series

PDF 4+ DBN	Chemical Formula	Crystal System	Space Group	Weight Fraction Start (w%)	Weight Fraction End (w%)
04-001-2617	Ag	Cubic	Fm-3m	87.5(1)	80.8(3)
00-004-0836	Cu	Cubic	Fm-3m	7.805(8)	1.98(4)
00-045-0937	CuO	Monoclinic	C2/c	------	9.6(2)
04-007-9767	Cu2O	Cubic	Pn-3m	4.673(5)	7.6(1)

The rest of the measurements in this series were also refined to a similar quality as the first and last measurement. Figure 42 shows a representative sample fit of the series in the mid-range of the corrosion investigation, which was taken after 9 hours of corrosion. This diffraction pattern is almost identical to the final measurement depicted in Figure 41, with only statistical differences and slightly weaker copper oxide reflections.

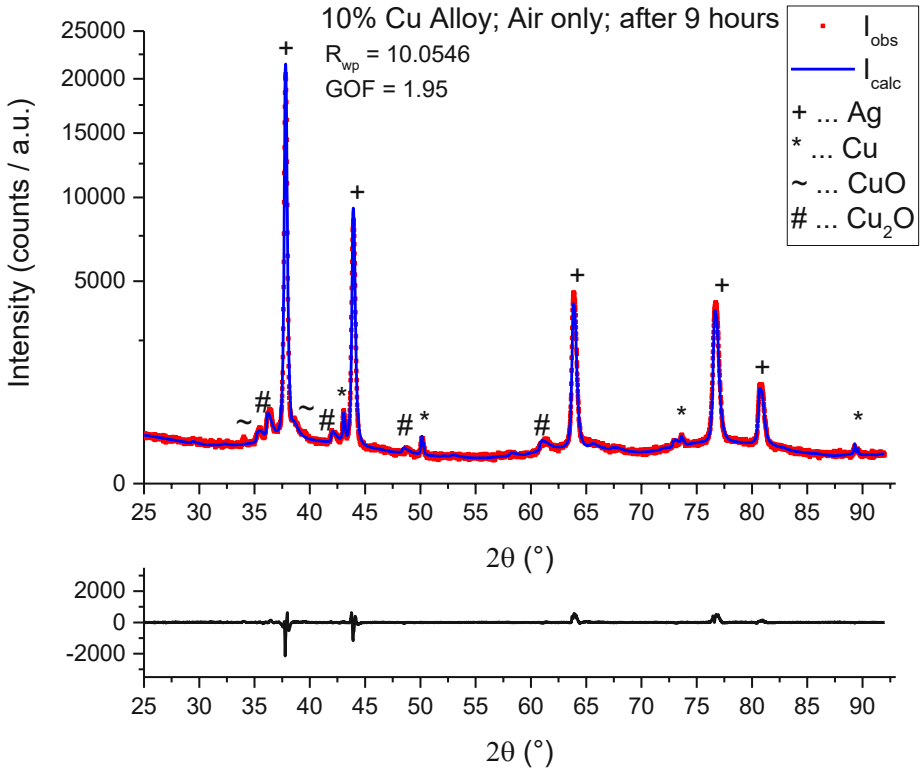

Figure 42: Refined XRD data of the 10wCu_Air series after 9 hours of corrosion

6.5.2 10 w% Cu Alloy corroded with Air and Brine Spray / 10wCu_NaCl

In comparison to the investigation beforehand (Chapter 6.5.1) this sample was additionally exposed to brine in addition to air (Table 4). Figure 43 and Figure 44 show the first and last measurement respectively and the refined phases are depicted in Table 15.

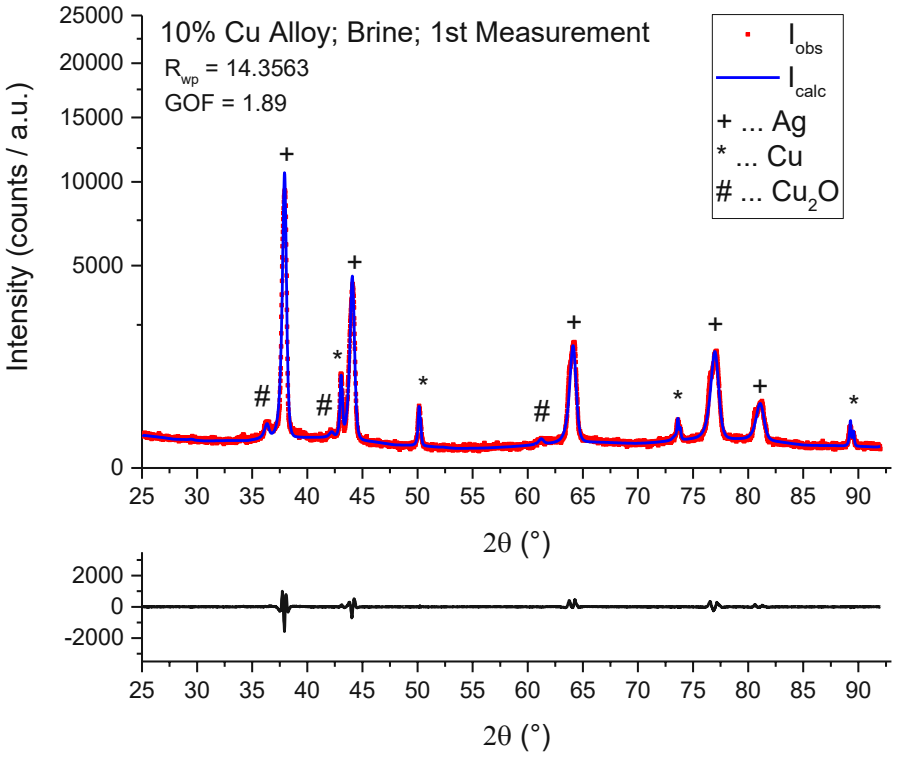

Figure 43: Refined XRD data of the 10wCu_NaCl series at the start of the corrosion

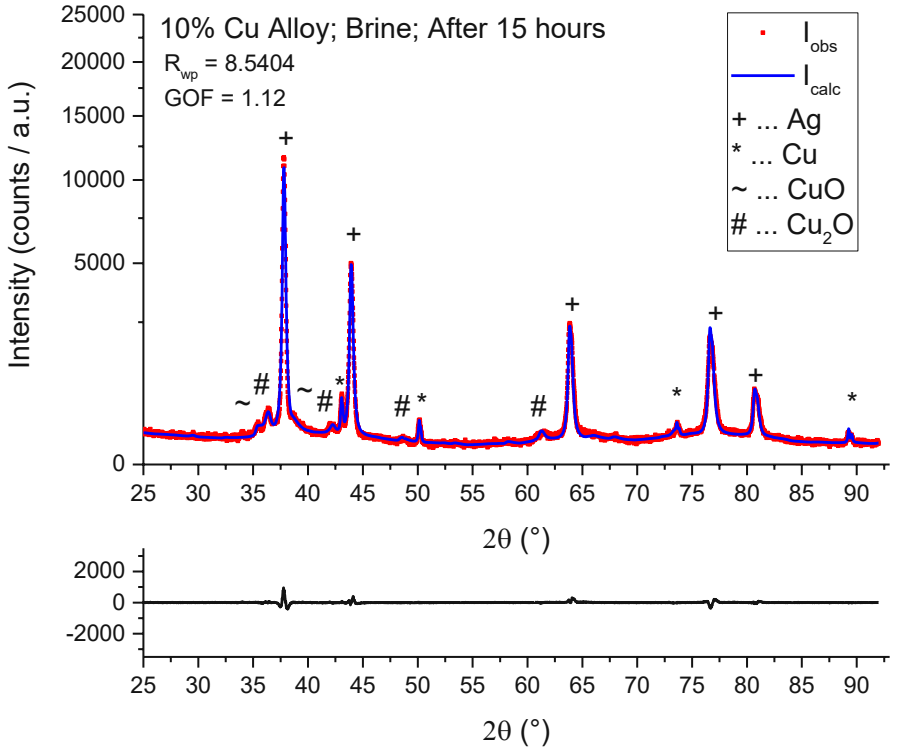

Figure 44: Refined XRD data of the 10wCu_NaCl series after 15 hours of corrosion

Table 15: Refined phases of the 10wCu_NaCl series

PDF 4+ DBN	Chemical Formula	Crystal System	Space Group	Weight Fraction Start (w%)	Weight Fraction End (w%)
04-001-2617	Ag	Cubic	Fm-3m	86.7(8)	81.6(3)
00-004-0836	Cu	Cubic	Fm-3m	9.57(8)	4.1(3)
00-045-0937	CuO	Monoclinic	C2/c	-------	7.6(2)
04-007-9767	Cu_2O	Cubic	Pn-3m	3.7(1)	6.7(2)

Comparing these two figures, the same trends compared the alloy corroded with air can be noted (Chapter 6.5.1). During the corrosion experiment the reflections of silver shift slightly to the left, with the second reflection of silver shifting from 44.0729 °2θ to 43.9006 °2θ, which is as shift of 0.1723 °2θ. The copper metal oxidises to form both copper(1)- and copper(2) oxide as two separate phases. There are no changes in the phases formed by the corrosion compared to the alloy corroded without the brine. Since there are no crystalline silver oxides or chlorides detected in the sample, these results do not match the corrosion products observed on the original Vienna Genesis.

Figure 45 shows a representative sample from the other refined patterns collected during the corrosion of the 10 w% Cu alloy with air and brine. As mentioned in chapter 4.5.1, a much smaller angle range was measured during the corrosion experiment in the same measurement time. For this reason, the diffraction pattern of Figure 45 shows a smaller angle range.

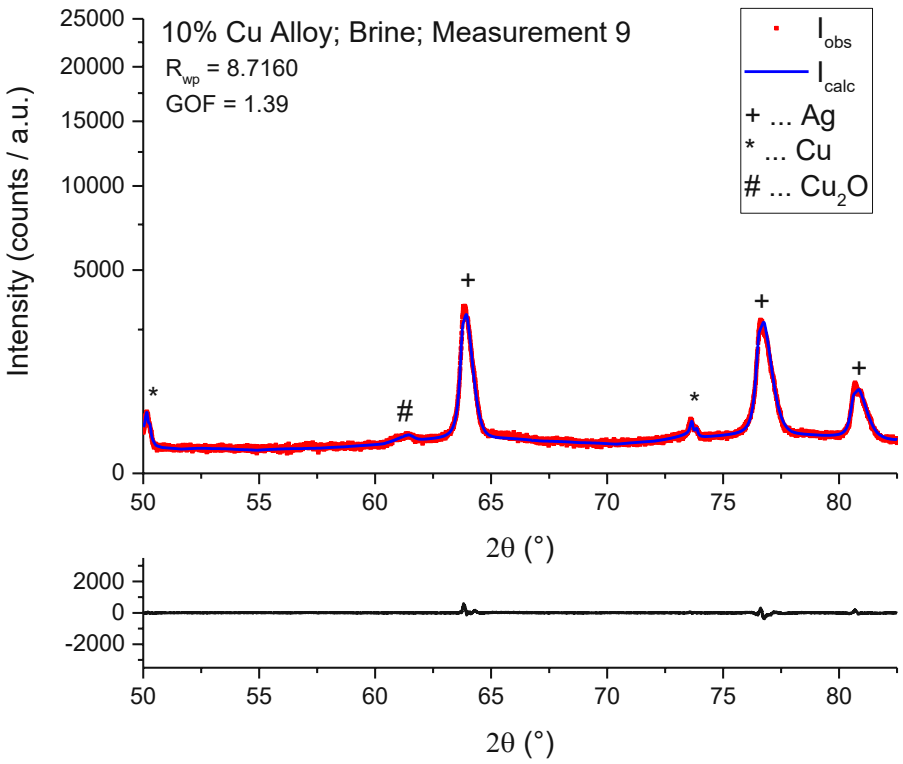

Figure 45: Refined XRD data of the 10wCu_NaCl series after 4.5 hours corrosion

This smaller angle range seems to offer advantages because the refinement process of only a few reflections is less complex and more straightforward in comparison to the full accessible pattern. Furthermore, a higher signal to noise ratio can be achieved because keeping the measurement time constant but decreasing the angle range increases the time per measured angle and yields a better signal to noise ratio.

However, there are serious drawbacks to using the smaller range. There are only a restricted number of reflections within the angle range for the individual phases (three for silver and two for copper), meaning the results out of the structural refinement are based on restricted information of the measurement. The significance of this error is observable by comparing the refined lattice parameter of silver in the full range with the refined parameter of the smaller range. In this series, the lattice parameter of silver determined by refining the full range was 4.10586(7) Å. However, if only the smaller angle range is refined, the result changes to 4.10596(11) Å, which is a significant difference outside of the error range determined when refining the full range. Because of this, the corrosion was measured in the full range for the experiments that were performed afterwards.

6.5.3 10 w% Cu Alloy corroded with Air after Homogenisation / 10wCu_LECO

The corrosion of the pure 10 w% Cu alloy with air (chapter 6.5.1) was repeated for multiple reasons, the most important being that the oxygen content of this alloy was measured to gain more information about the observed structure change during the segregation process. For this measurement a fresh alloy was required, which was prepared from the same precursor mixture as the other 10 w% copper samples after the powder was homogenized further, as described in 4.5.1.

Figure 46 and Figure 47 show the first XRD measurements of the corrosion collected at the beginning of the experiment, as well as the final measured XRD before stopping the corrosion. The refined phases are depicted in Table 16.

Table 16: Refined Phases of the 10wCu_LECO series

PDF 4+ DBN	Chemical Formula	Crystal System	Space Group	Weight Fraction Start (w%)	Weight Fraction End (w%)
04-001-2617	Ag	Cubic	Fm-3m	87.4(2)	82.3(3)
00-004-0836	Cu	Cubic	Fm-3m	6.11(5)	1.33(4)
00-045-0937	CuO	Monoclinic	C2/c	-------	7.6(1)
04-007-9767	Cu_2O	Cubic	Pn-3m	6.45(9)	8.77(9)

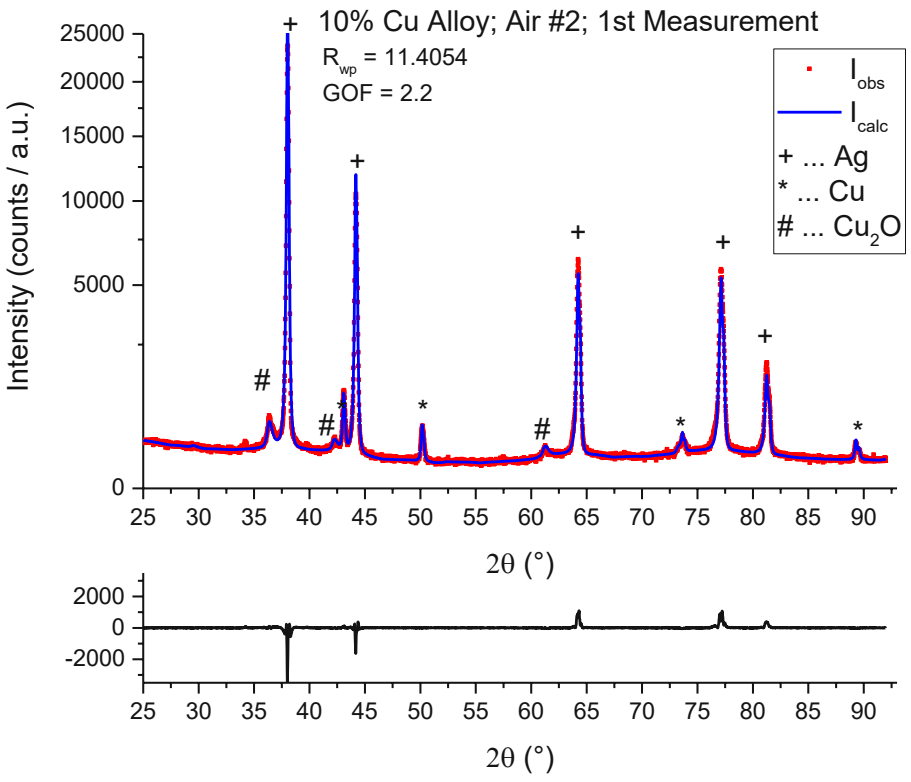

Figure 46: Refined XRD data of the 10wCu_LECO series at the start of the corrosion

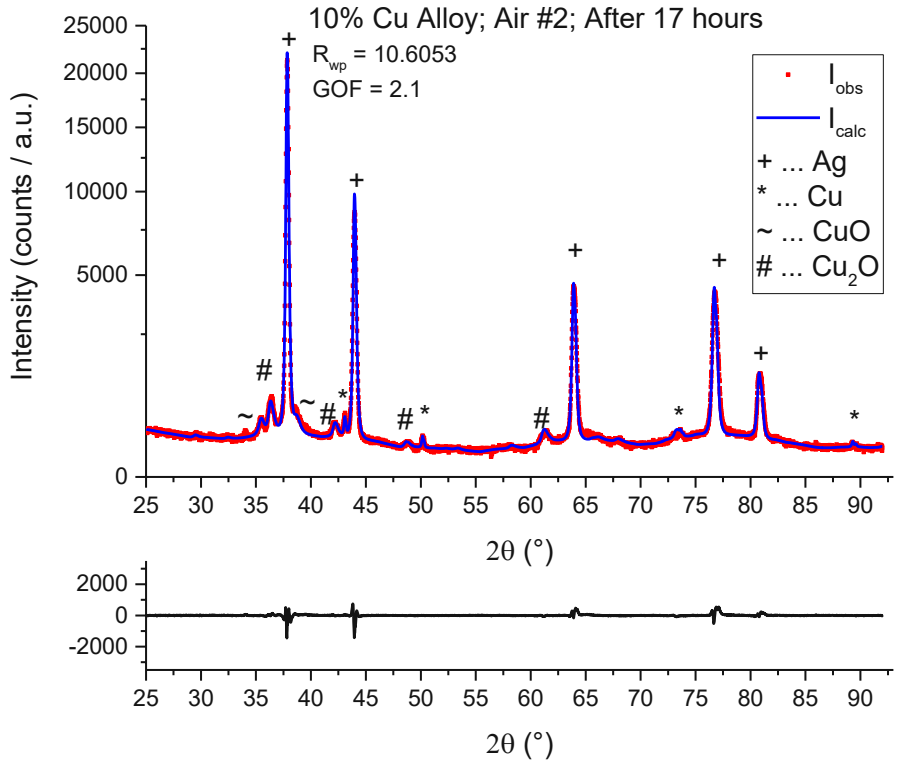

Figure 47: Refined XRD data of the 10wCu_LECO series after 17 hours of corrosion

The same behaviour of the copper metal corroding seen in chapters 6.5.1 and 6.5.2, which forms both copper(1)- and copper(2)oxide phases, can be observed in this sample as well. However, a big difference between this sample and the originally performed experiment (chapter 6.5.1) is present in the observed peak shift of the silver reflections. Here the segregation reaction causing this shift is much slower than what was observed originally for an undetermined reason. In numerical values the second silver reflection shifts from 44.1677 °2θ to 43.9448 °2θ, which is a decrease of 0.2229 °2θ. Furthermore, the shift stops at marginally bigger angles than with the original experiment. This is depicted in Figure 61 and Figure 62 of chapter 6.7, where this is discussed further.

Figure 48 shows a representative sample of the other refined diffraction patterns of this corrosion series, which was taken after 9.5 hours of corrosion.

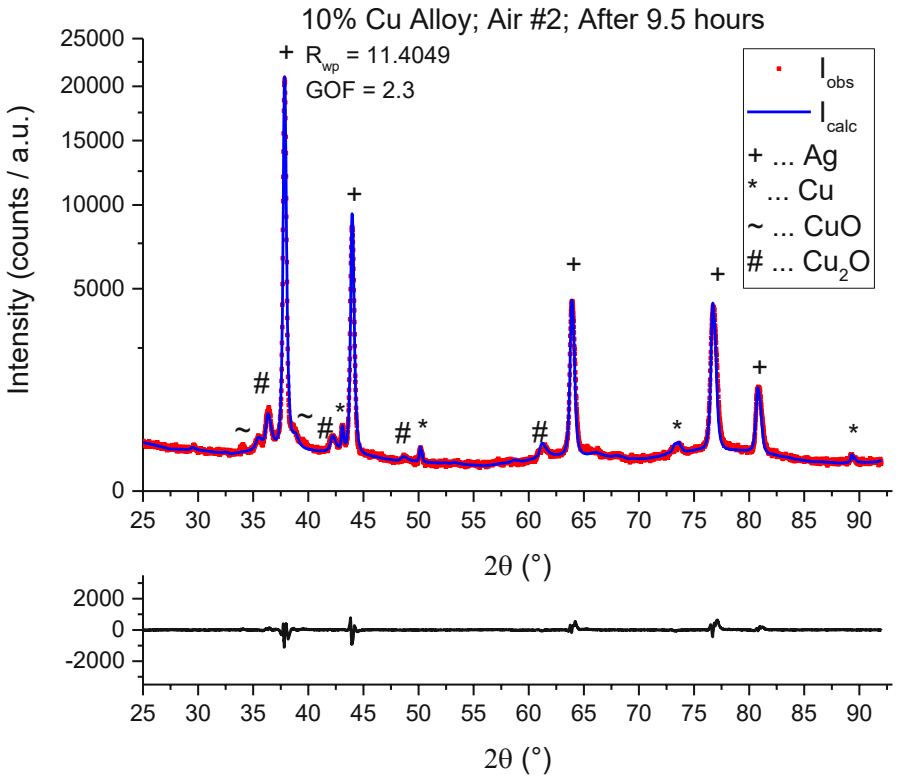

Figure 48: Refined XRD data of the 10wCu_LECO series after 9.5 hours of corrosion

The oxygen content of this sample was also determined using thermal decomposition and detecting the contained oxygen using infrared radiation, as described in 4.5.2 “Oxygen Content Analysis”. The results of this analysis are shown in Table 17. Sample 4 was omitted from the average- and error calculation, because it was noted that it contained significant contamination with the oxygen rich silica-based filter material, which could not be separated completely and falsified the result. This was noticed

while weighing the samples before the measurement took place. The other samples did not contain significant amounts of this filter material.

Table 17: Results of the oxygen content analysis of the 10 w% copper alloy

Sample Number	Weight (g)	Oxygen content (w%)
1	0.0149	2.67
2	0.0123	2.59
3	0.0193	2.74
4	0.0135	3.10
5	0.0203	2.65
6	0.0166	2.66
Average	----------	2.66 ± 0.05

To prove the significance of these results, a calculation of the theoretical oxygen content was performed. This calculation assumes that all of the copper contained in the alloy got corroded fully to copper(2) oxide CuO, with silver remaining in the metallic state. This reaction is described by equation 19 and represents the maximum amount of oxygen that can be bound by copper alone. The calculated weight percentages of the fully corroded alloy are depicted in Table 18.

$$Ag_xCu_y + \frac{y}{2}O_2 \rightarrow x\,Ag + y\,CuO \tag{19}$$

Table 18: Theoretical composition a 10 w% Cu silver-copper alloy, after the total corrosion of copper metal to copper(2) oxide CuO with silver remaining metallic.

Element	Fresh alloy Composition (w%)	Fully corroded alloy (w%)
Ag	90	87.8
Cu	10	9.76
O	0	2.44

The calculated maximum oxygen content after the full corrosion of copper is therefore only 2.44 w%. The oxygen content analysis found a higher oxygen content than that at 2.66 w%. This assumes that additional oxygen is bound somewhere in the structure, either on lattice sites or as interstitials. This is further supported by the observation that copper metal is left over in the phase mixture in the final state of the sample. Moreover, part of the copper is found present as copper(1) oxide Cu_2O. An Impurity in form of filter material based on silica was found. It could not be separated effectively during the preparation of the samples. As seen with sample 4, it can have a strong effect on the measured oxygen content. But representing only a tiny fraction of the weighed sample, it cannot explain the huge difference between the expected and measured oxygen content. Hence the analysis supports the

assumption that some oxygen enters the crystal structure of silver. This might also explain the shift to lattice parameters higher than in pure silver for the silver cell of the segregated species.

6.5.4 Sample with added internal Standard corroded with Air / 10wCuAl_2O_3_Air

To further confirm the refined lattice parameters, the corrosion series described in chapter 6.5.1 was repeated with an internal standard. The sample preparation and measurements are described in chapter 4.5.3.

Figure 49 shows the fresh powder directly after the reduction. This measurement was performed while the sample was still in the hydrogen atmosphere. Because hydrogen is a light gas with a very low density, it absorbs less X-ray radiation than air, which results in higher measured intensities during the measurement. The final measurement before the corrosion was stopped is depicted in Figure 50 and the refined phases depicted in Table 19.

An identical behaviour to the second corrosion experiment of the pure 10 w% Cu alloy with air is observed (chapter 6.5.3). In both samples the copper corrodes almost completely to form copper(1)- and copper(2) oxide and the silver reflections slowly shift to smaller angles. In this series the second reflection of silver shifts from 44.2040 °2θ to 43.9434 °2θ, which is a shift of 0.2606 °2θ. There are no silver corrosion products observed in the sample.

The addition of the standard provides a reference value to check if the refinement results are valid. While the SEM measurements of the sample containing the standard showed a strong influence on the morphology, it does not influence the XRD measurements nor the refinement. Contrary, higher intensities are observed compared to the samples without the standard. This is probably a result of the standard preventing the silver particles from sintering together, which is discussed further in chapter 6.3.2.

Table 19: Refined Phases of the 10wCuAl_2O_3_Air series

PDF 4+ DBN	Chemical Formula	Crystal System	Space Group	Weight Fraction Start (w%)	Weight Fraction End (w%)	Weight Fraction Recryst. (w%)
04-001-2617	Ag	Cubic	Fm-3m	64.7(1)	63.2(3)	60.6(2)
00-004-0836	Cu	Cubic	Fm-3m	10.43(4)	2.78(3)	-------
00-045-0937	CuO	Monoclinic	C2/c	--------	4.9(1)	12.89(7)
04-007-9767	Cu2O	Cubic	Pn-3m	2.04(3)	7.36(8)	3.96(4)
04-007-1400	Al2O3	Rhombo-hedral	R-3c	22.83(3)	21.7(2)	22.6(1)

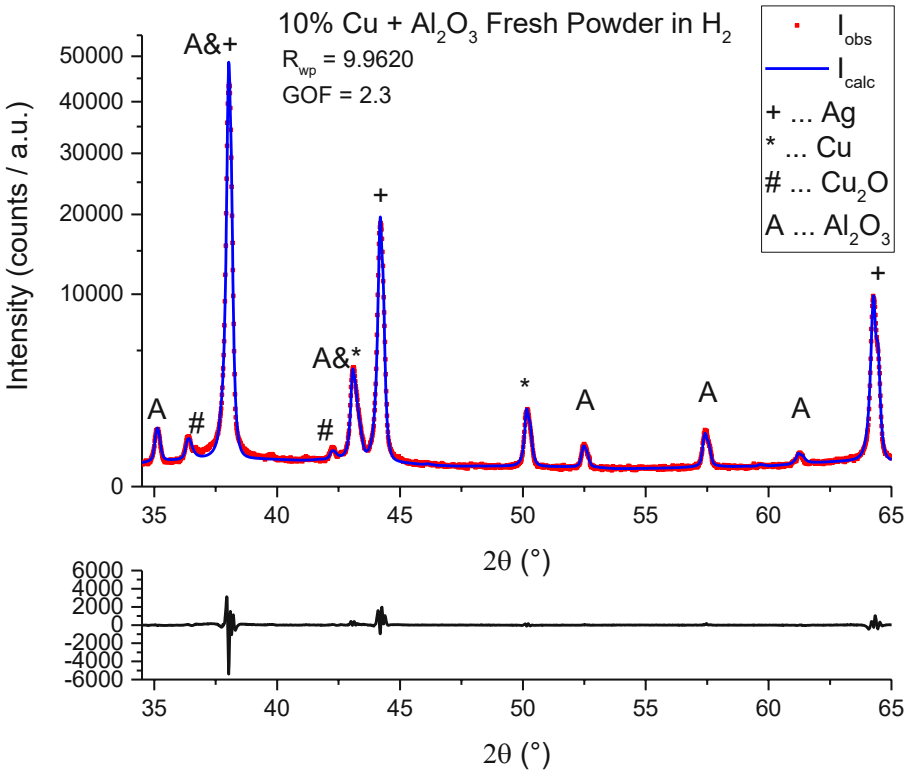

Figure 49: Refined XRD data of the 10wCuAl$_2$O$_3$_Air series before the corrosion, measured under hydrogen

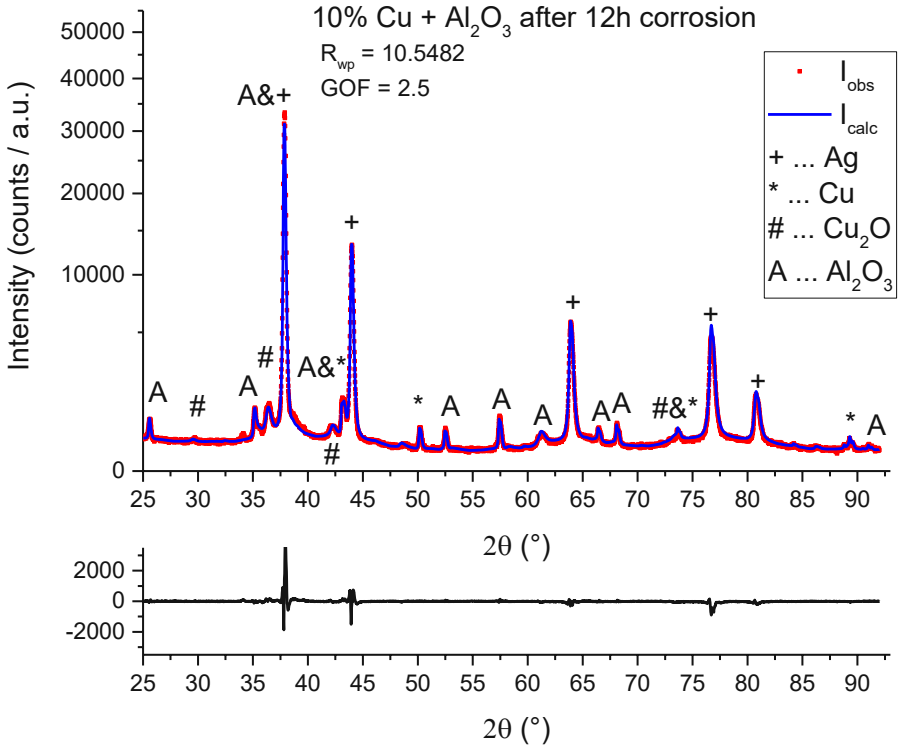

Figure 50: Refined XRD data of the 10wCuAl$_2$O$_3$_Air series after 12 h of corrosion

To further test the properties of the segregated phases, a recrystallisation was performed after the measurement, which is illustrated in Figure 50. After this recrystallisation step the sample was cooled back down again and measured for four hours to check if the segregation would continue, or if the alloy had reached a stable state during the recrystallisation. One of these measurements is depicted in Figure 51.

By comparing Figure 51 to the sample before the recrystallisation (Figure 50), it is found that this recrystallisation step has multiple effects on the sample. One effect is that the leftover copper metal is corroded completely, since the remaining copper reflections of Figure 50 vanished in Figure 51. Furthermore, parts of the copper(1) oxide are converted to copper(2) oxide, which developed strong reflections during the recrystallisation. This is expected, because the higher temperature of 500 °C during the recrystallisation speeds up the high temperature corrosion process corroding the copper. The other effect is, that the silver reflections shift back to higher angles. The second silver reflection shifts from 43.9434 °2θ to 44.0699 °2θ, which matches the predicted position for pure silver metal. Setting this observation in light of the lattice parameters for pure silver, we can state that the recrystallisation process recovers the lattice parameter values to the ones of pure silver metal. This is discussed further in chapter 6.7 about the observed segregation.

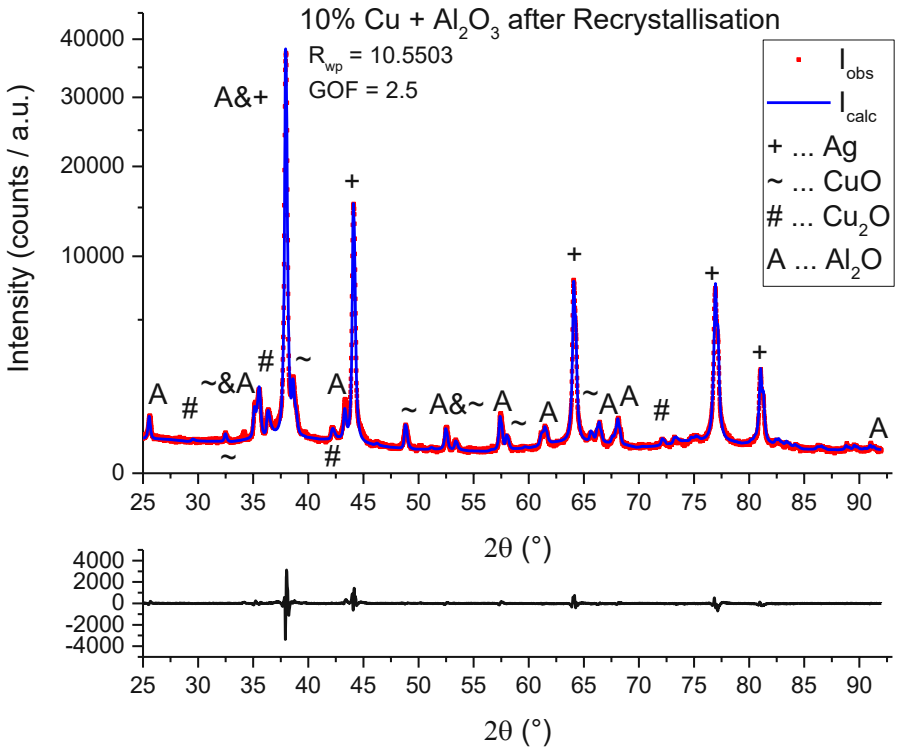

Figure 51: Refined XRD data of the 10wCuAl₂O₃_Air series after the recrystallisation at 500 °C for 1 hour

6.5.5 Sample with added internal Standard, Blind Experiment / 10wCuAl_2O_3_Blind

To confirm that oxygen is responsible for the observed segregation, the experiment described in the previous chapter with the added internal standard was repeated with the same precursor mixture, but without pressurized air. Instead, argon was used as an inert gas. This has the effect that more x-ray radiation is absorbed by the dense argon gas in the reaction chamber and results in lower overall intensities.

Figure 52 shows the first XRD measurement taken at the start of the corrosion experiment and Figure 53 shows the last XRD measurement of this corrosion series. Both diffraction patterns are virtually identical, with no corrosion products formed or peak shift happening to the silver reflection during the experiment. Only silver, copper, alumina and traces of remaining copper(1) oxide were detected.

Table 20: Refined phases for the 10wCu+Al2O3_Blind series

PDF 4+ DBN	Chemical Formula	Crystal System	Space Group	Weight Fraction Start (w%)	Weight Fraction End (w%)
04-001-2617	Ag	Cubic	Fm-3m	64(1)	65(1)
00-004-0836	Cu	Cubic	Fm-3m	9.2(1)	9.1(1)
04-007-9767	Cu2O	Cubic	Pn-3m	2.9(1)	3.2(1)
04-007-1400	Al2O3	Rhombohedral	R-3c	23.7(5)	23.1(5)

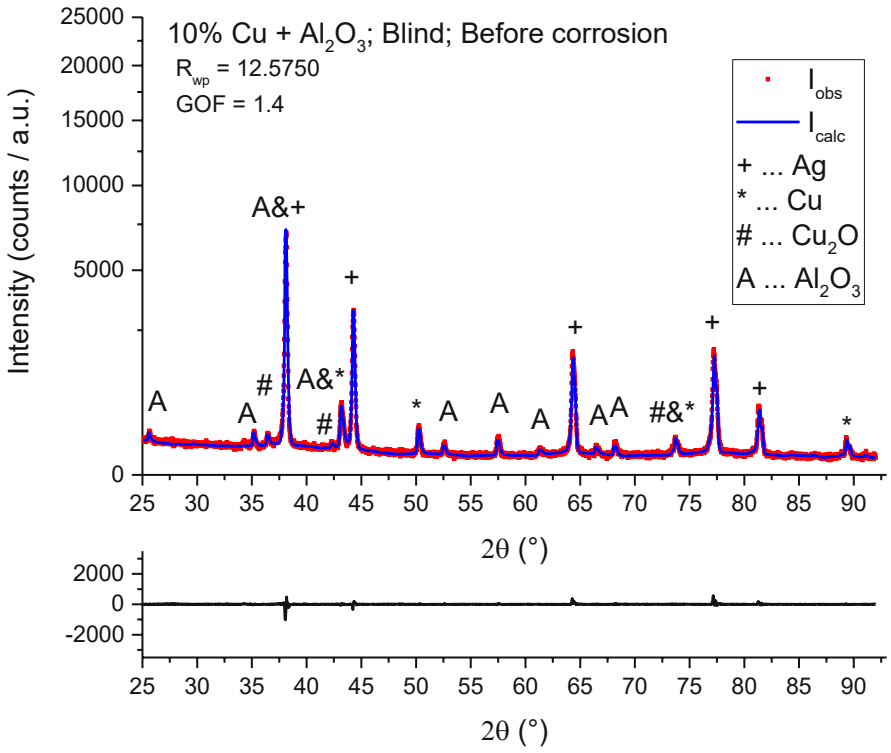

Figure 52: Refined XRD data of the 10wCuAl_2O_3_Blind series before the corrosion, measured at 275 °C under argon

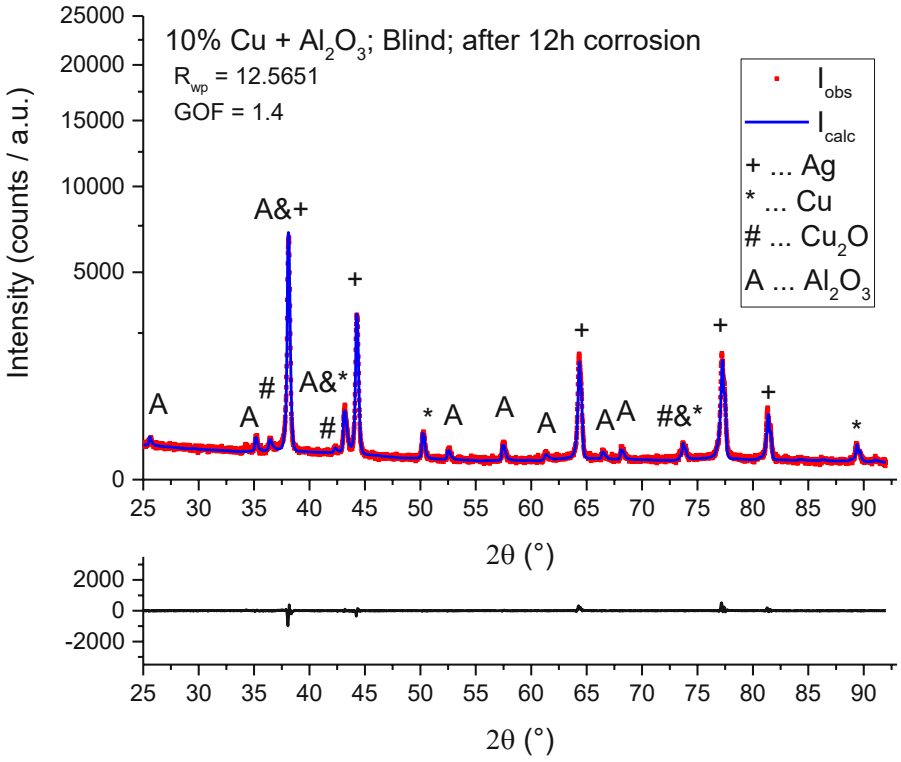

Figure 53: Refined XRD data of the 10wCuAl_2O_3_Blind after 12 hours of corrosion, measured at 275 °C under argon

The recrystallisation step performed by heating the sample to 500 °C for 60 minutes also did not cause any change in the observed phases or reaction in the sample, as seen in Figure 54 which is also almost identical to Figure 52 and Figure 53, besides statistical differences.

No corrosion products or shift of the silver reflection were detected in the inert and oxygen free atmosphere. It is not surprising that no oxidised copper is found in the sample besides the oxide present from the start of the corrosion, because oxygen is required to form copper oxides. However, this proved that the observed shift of the silver reflection to smaller angles is not an effect of the temperature program, but oxygen is implied to be responsible for this.

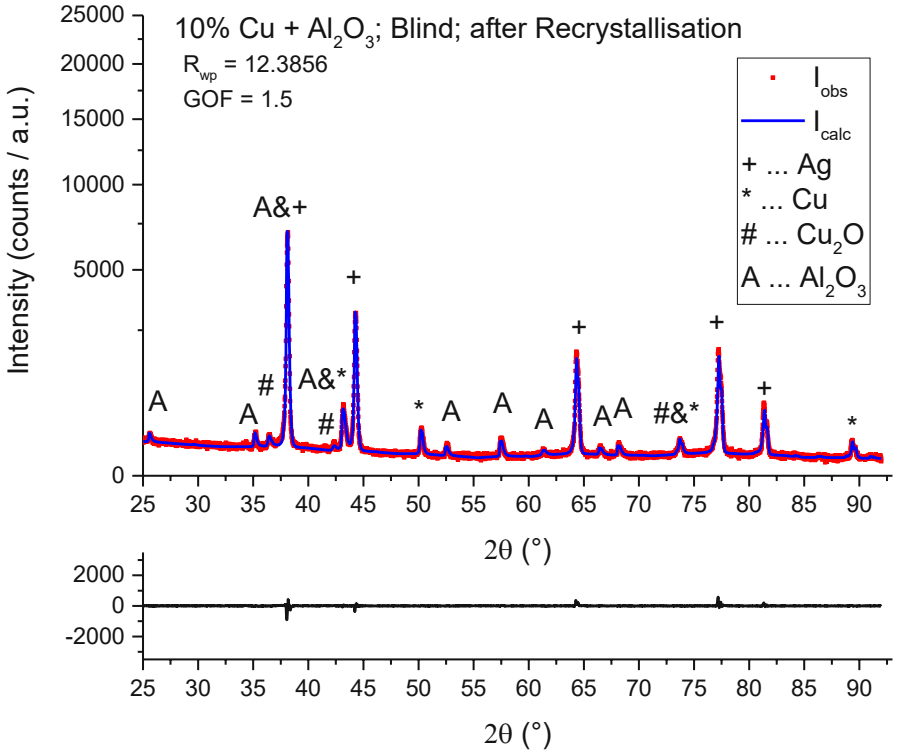

Figure 54: Refined XRD data of the 10wCuAl_2O_3_Blind after recrystallisation at 500 °C for 1 hour, measured at 275 °C under argon

6.5.6 Long-Term Experiment / 10wCu_Long

To investigate the stability of the sample at a lower temperature, a long-term experiment was performed. A selection of the measured diffraction patterns is shown in Figure 55.

There is no significant change observed in the diffraction patterns during the experiment. This is emphasised further in Figure 56, which shows a smaller angle range of the measured XRD-data. While there are small differences in the peak intensities, these most probably arise due to small reorientation processes of the crystallites from the extended treatment with brine spray, or increased absorption of X-ray radiation by liquid water collecting on the sample. There is also no crystalline sodium chloride present. This can be explained by the presence of liquid water in the sample. At 75 °C the solubility of salt in water is increased when compared to 25 °C, which explains the absence of undissolved crystalline sodium chloride. Because liquid water left the reaction chamber and entered the flow meter at the end of the gas line, a constant flow of salt in and out of the reaction chamber is achieved. The fact that the water leaving the reaction chamber contains salt is confirmed by the corrosion damage observed on the flow meter.

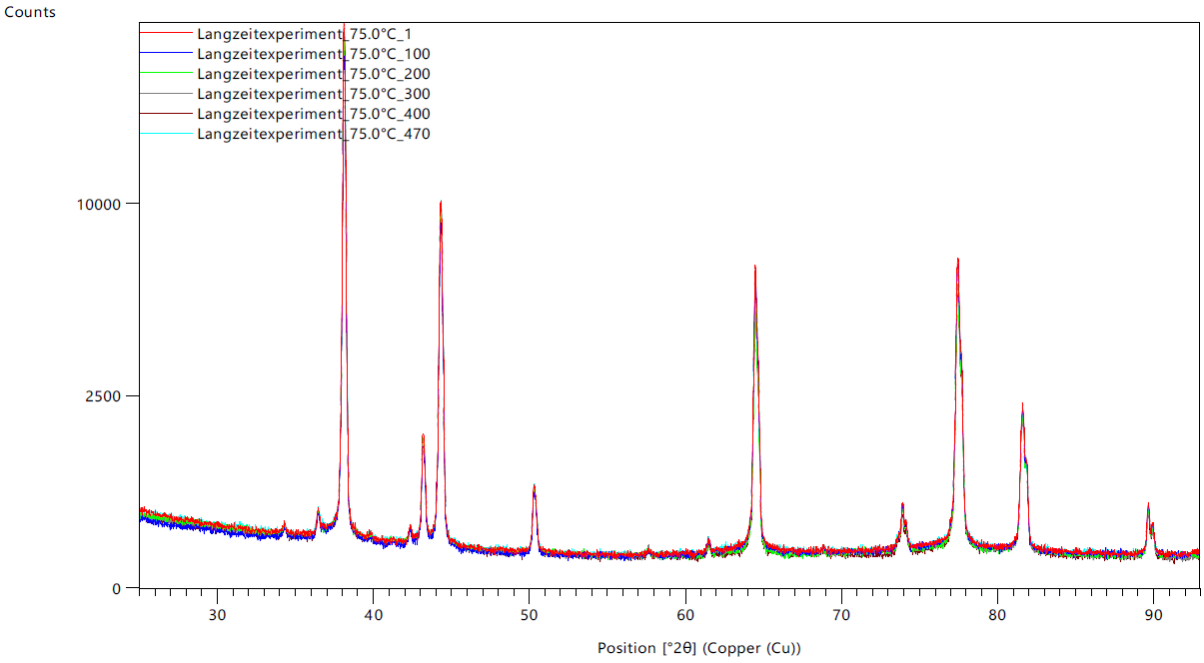

Figure 55: Overview of the 10wCu_Long series, measured at 275 °C

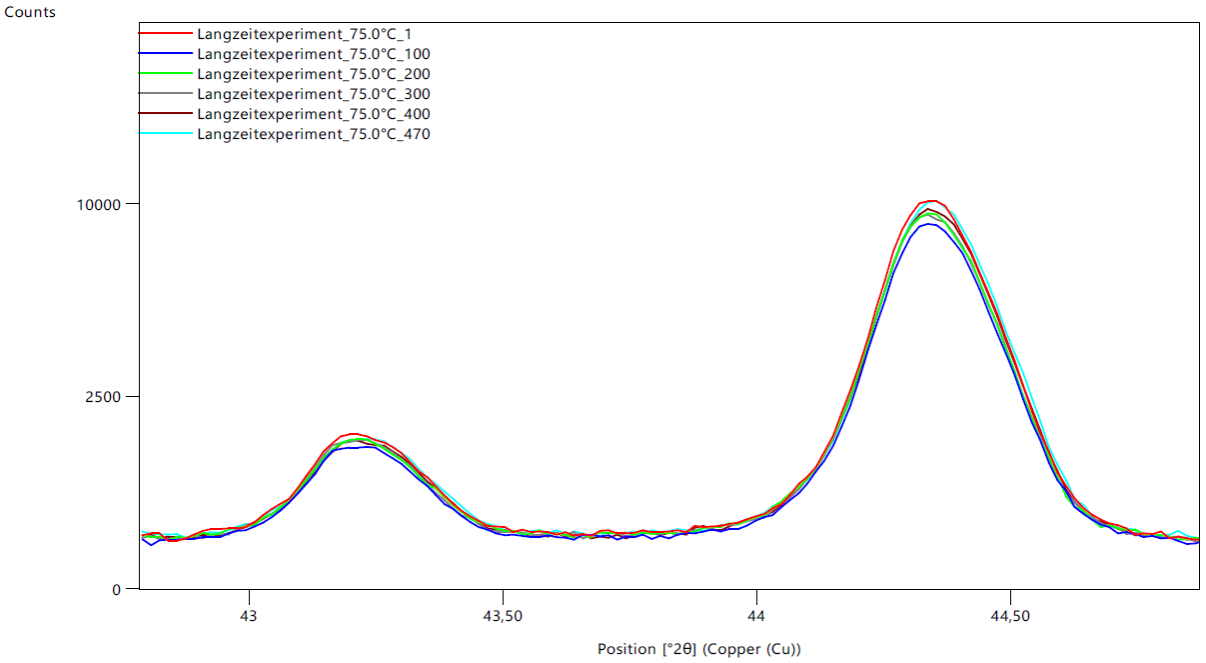

Figure 56: Zoomed area of the10wCu_Long series depicted in Figure 55.

6.6 1.5 w% Copper Alloy

The precursor mixture prepared for a 1.5 w% Cu alloy (chapter 4.6) was mixed with the internal standard and homogenized thoroughly. Parallel beam optic for monochromatizating the beam was used to remove the specimen displacement error.

Figure 57 shows the refinement of the first measurement of the series, with the refined phases depicted in Table 21. In this case only a very small amount of a separate copper phase was present. The lattice parameter calibration model outputs an approximate copper content of 0.84 w% copper in the silver phase, which is in the expected range considering there is a trace of copper metal visible in the PXRD.

Comparing this with Figure 58, which shows the last measurement in this series, a slight shift of the silver reflection can be observed, as in the samples containing 10 w% copper which were discussed in chapter 6.5. In this series the second reflection of silver shifts from 44.1458 °2θ to 44.0464 °2θ, which is a difference of 0.0994 °2θ, much smaller than the peak shift observed with 10 w% copper samples. Furthermore, small amounts of oxides were also formed. The peak shift was refined using the Rietveld method, where a slight but significant increase of the lattice parameter above the value of pure silver was observed. This is discussed further in chapter 6.7 “Oxygen induced segregation”.

Table 21: Refined phases of the 1,5wCuAl_2O_3_Air corrosion series

PDF 4+ DBN	Chemical Formula	Crystal System	Space Group	Weight Fraction Start (w%)	Weight Fraction End (w%)	Weight Fraction Recryst. (w%)
04-001-2617	Ag	Cubic	Fm-3m	74.1(3)	73.4(2)	72.4(2)
00-004-0836	Cu	Cubic	Fm-3m	0.42(4)	0.25(3)	0.21(2)
04-007-9767	Cu2O	Cubic	Pn-3m	2.52(5)	2.64(4)	2.32(4)
04-007-1400	Al2O3	Rhombo-hedral	R-3c	23.0(2)	23.7(2)	25.1(2)

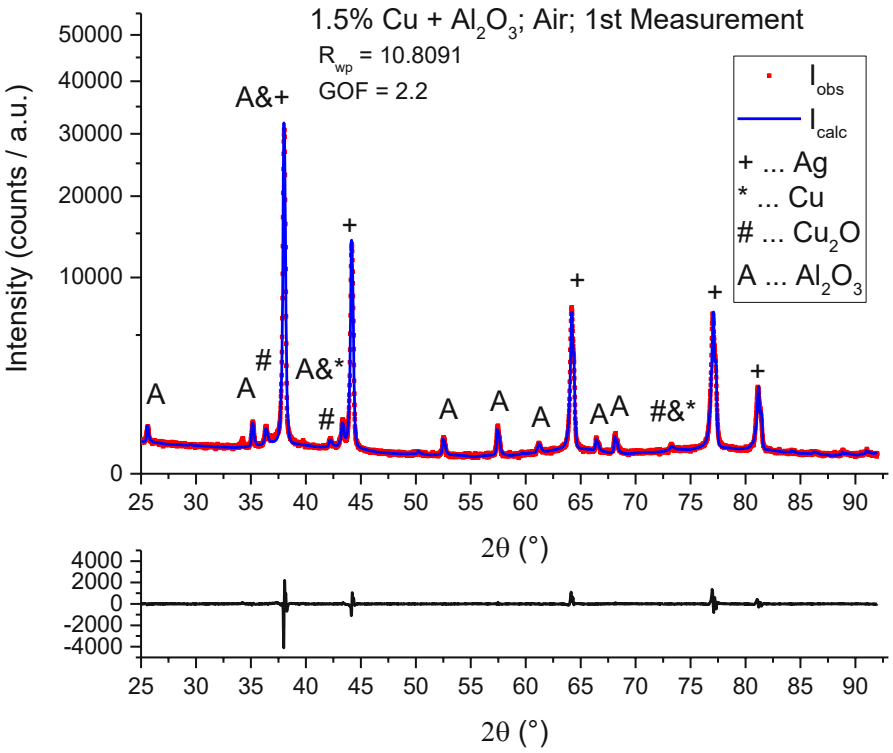

Figure 57: Refined XRD data of the 1.5wCuAl$_2$O$_3$_Air series at the start of corrosion

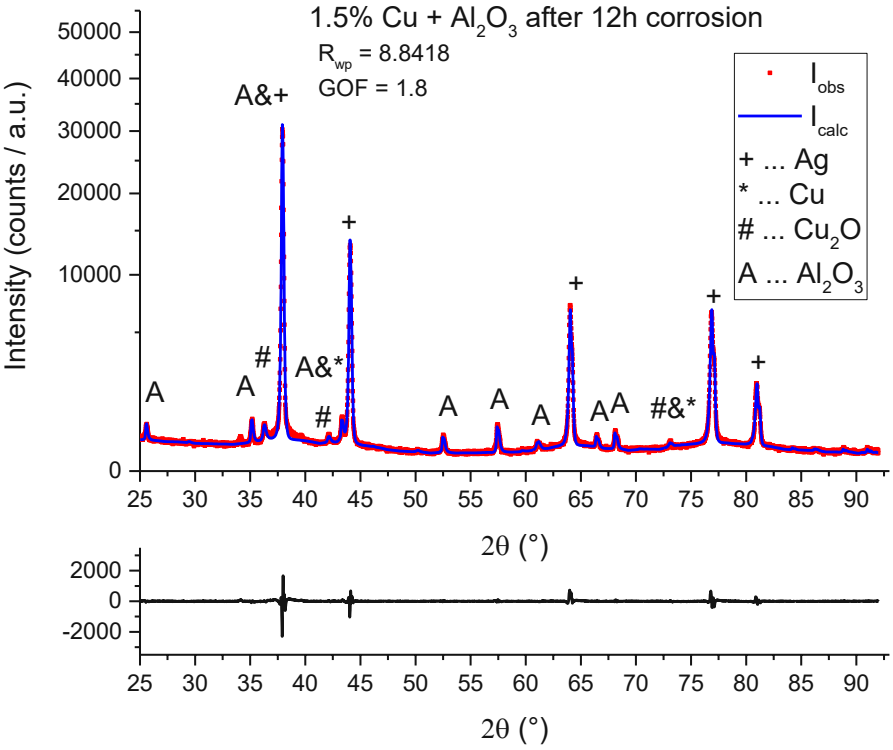

Figure 58: Refined XRD data of the 1.5wCuAl$_2$O$_3$_Air series after 12 hours of corrosion

Like the 10 w% copper sample containing the internal standard (chapter 6.5.4), a recrystallisation step was also performed after the corrosion process was finished. The diffraction pattern after the recrystallisation is pictured in Figure 59. Here the silver reflections shifted again, this time to larger angles. The refined lattice parameter of the recrystallized silver is slightly below the expected value for pure silver. This is probably caused by some copper remaining in the silver metal.

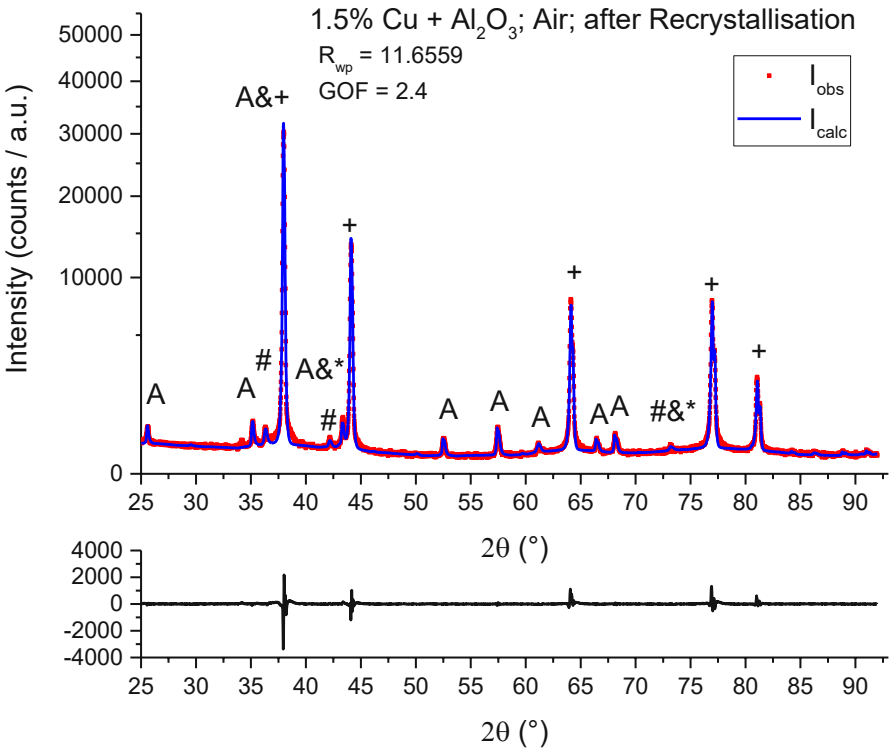

Figure 59: Refined XRD data of the 1.5wCuAl_2O_3_Air series after recrystallisation at 500 °C for 1 hour

6.7 Oxygen induced segregation

Segregation of the Ag-Cu alloy, where the elements concentrate at different points, was first observed in the Temperature Variation series during the corrosion of the 10 w% copper alloy at temperatures above 200°C in the presence of oxygen gas. In the PXRD this is visible as a shift of the diffraction maxima of silver to lower angles. This change is predicted by the rule of Vegard, which predicts an increase of the lattice parameters with lower copper contents. This leads to the reflections being observed at lower angles. Figure 60 shows the segregation effect as originally observed in the Temperature Variation Series discussed in chapter 6.4. In this case, the first 300 minutes of corrosion time are pictured, since the segregation seems to have run to completion at this point. There is also only a small angle range from 42.5 – 45 °2θ depicted to make the peak shift visible. The second silver reflection pictured shifts from 43.911 °2θ to 43.614 °2θ, a difference of 0.297 °2θ.

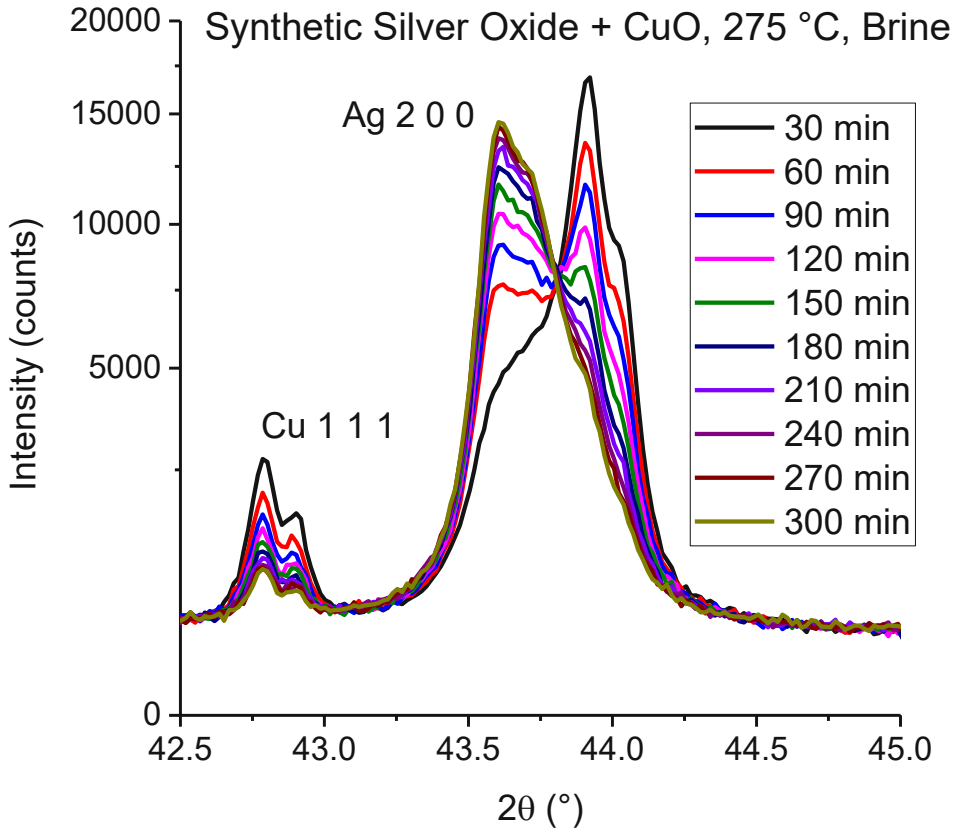

Figure 60: Peak shift observed in the Temperature Variation Series at 275 °C in the first 300 minutes between 42.5 and 45.0 °ϑ

Since this series was measured under focusing conditions of the beam, the angle resolution of the diffraction pattern is enhanced. Therefore, it was possible to closely follow the peak shift during the reaction time. As a result, it is observable that the shift of the silver reflection is continuous. This might be an effect of internal macrostrain affecting a shift of reflections in the diffraction pattern and consequently a change in lattice spacing. Another explanation would be a change in the structural

arrangement as is observable for a phase transition, where one part of the reflections shrink and/or new reflections arise.

Unfortunately, these patterns could not be refined to any significant result, due to issues such as the impurities of the precursors, which complicate the refinement process, and the specimen displacement error, which might be caused by a morphological change of the sample during the reduction and corrosion processes. For this reason, the experiment was repeated using pure precursors to evaluate the relevance of this observation.

Figure 61 shows the repeated experiment using pure precursors, as described in chapter 6.5.1 “10 w% Cu Alloy corroded with Air”. In this sample the copper metal corroded to form oxides, and the silver reflections shifted to smaller angles. For this sample the shift observed was from 44.0546 °2θ at the start of the corrosion to 43.9053 °2θ, which is a shift of 0.1493 °2θ. This was almost identical behaviour as the sample corroded with brine spray, which is not pictured in this chapter for this reason. This indicates that the segregation is independent of the brine, since it was not used for the other experiments investigating the segregation. Furthermore, parallel beam optics were used in this experiment, which solves the problem with the specimen displacement error.

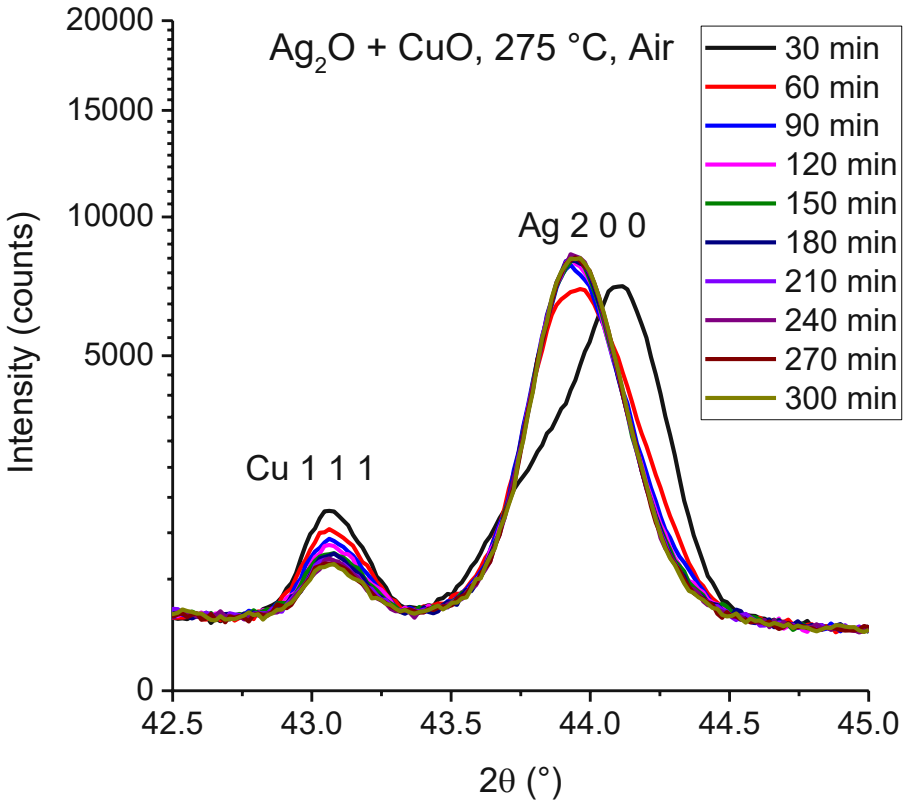

Figure 61: Segregation observed in the 10wCu_Air series prepared using clean precursors and corroded with air

The evaluation of the data of this experiment assumes the segregation is completed after only 90 minutes. This is also observable in the raw diffraction data of Figure 61, where only the silver reflections of the first two measurements differ from the later measurements. However, when repeating this series (chapter 6.5.3) after homogenising the precursor mixture very different results were obtained. The results of this series are pictured in Figure 62.

The main difference between the investigation here and the series pictured in Figure 61 is an additional homogenisation of the precursor mixture. This resulted in the segregation slowing down significantly.

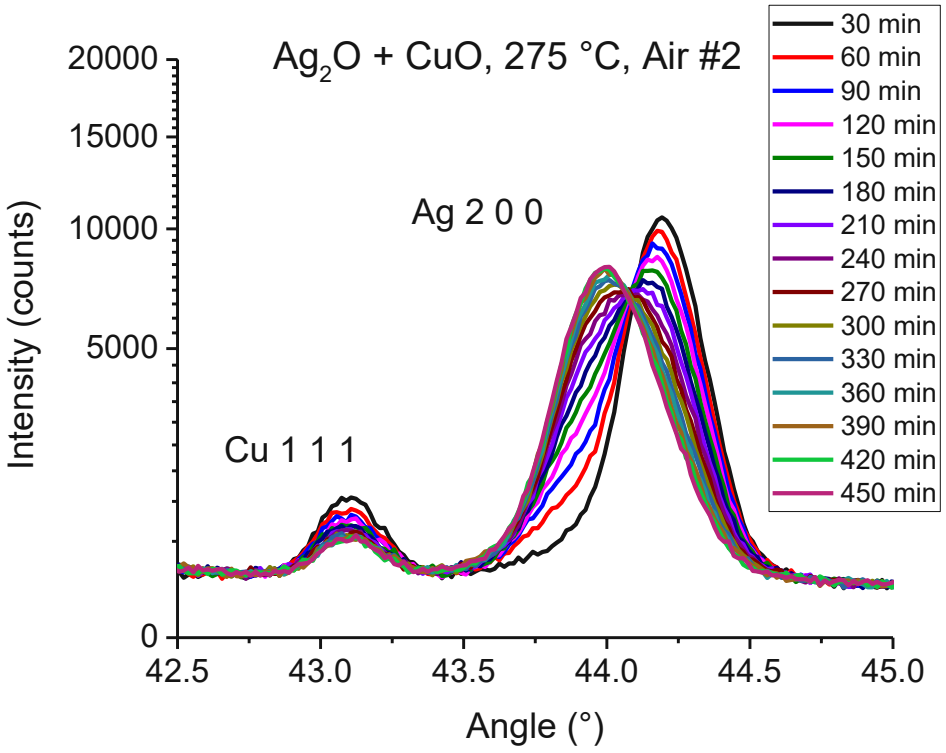

Figure 62: Segregation observed in the 10wCu_LECO series prepared using clean precursors and corroded with air

To further prove that this observed behaviour is a real and reproducible effect, the same precursor mixture was mixed with an internal standard and the experiment was repeated. Additionally, a recrystallisation step after the corrosion was also performed to investigate the reversibility of this transformation. Figure 63 shows the measured PXRD-patterns of this experiment.

In comparison to the 10 w% Cu alloys without the standard, the segregation was about 5 times slower than the original series, requiring 450 minutes instead of 90 minutes to complete. However, it is about the same speed as the second alloy prepared with this composition after homogenising the precursor mixture, where both needed about 450 minutes to complete the segregation. There are also multiple overlapping reflections of the standard with silver, copper, and the copper oxides. One of these overlaps is visible in Figure 62, were the copper and alumina reflections overlap slightly at 43.25 °θ.

Overlaps of this kind can complicate the evaluation of PXRD data immensely, but in this series, these could be effectively refined to a high quality, which separates the different reflections.

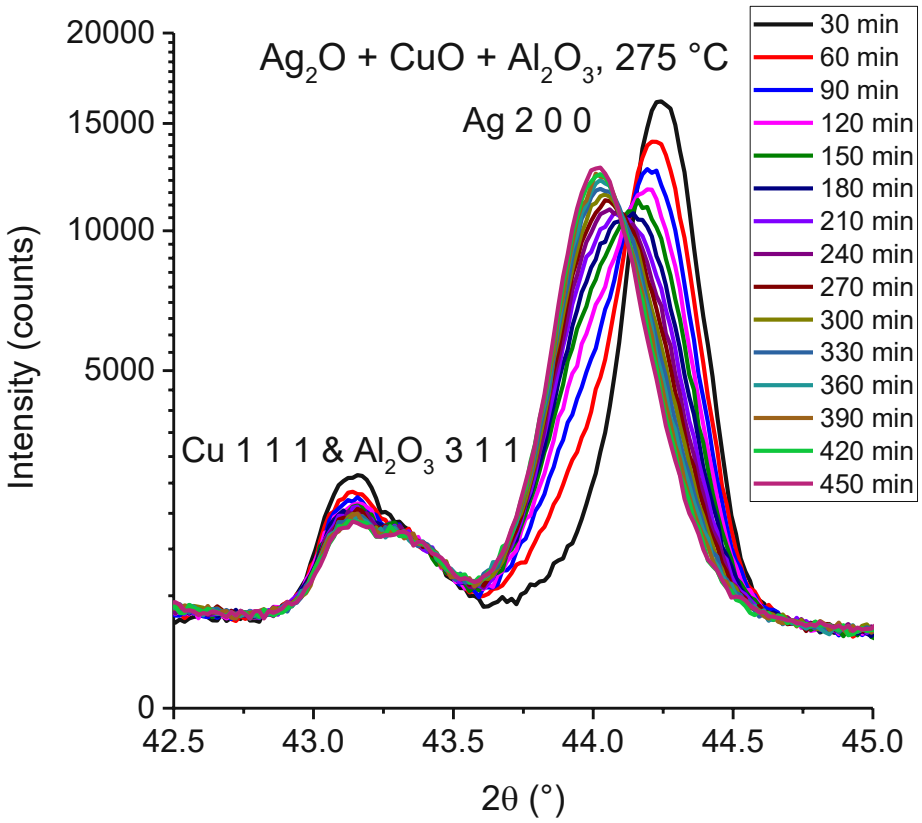

Figure 63: Segregation observed in the 10wCuAl_2O_3 series prepared with an alumina standard and corroded with air

Finally, this experiment was repeated with an alloy using a lower copper content of 1.5 w% with an internal standard. The peak shift observed in this experiment is illustrated in Figure 64. For this composition, the second silver reflection shifts by a much lower distance of 0.0994 °2θ compared to the 10 w% samples, where the same reflection shifts by 0.2606 °2θ. There also is a copper phase present in the 1.5 w% samples with a much lower observed intensity compared to the 10 w% copper samples. This phase was not affected by the oxidation process. This represents a significant difference to the experiments for the samples with higher copper contents. Otherwise, the observed behaviour is identical to the samples with a higher copper content, with copper forming both copper(1)- and copper(2) oxides and no silver corrosion products being formed.

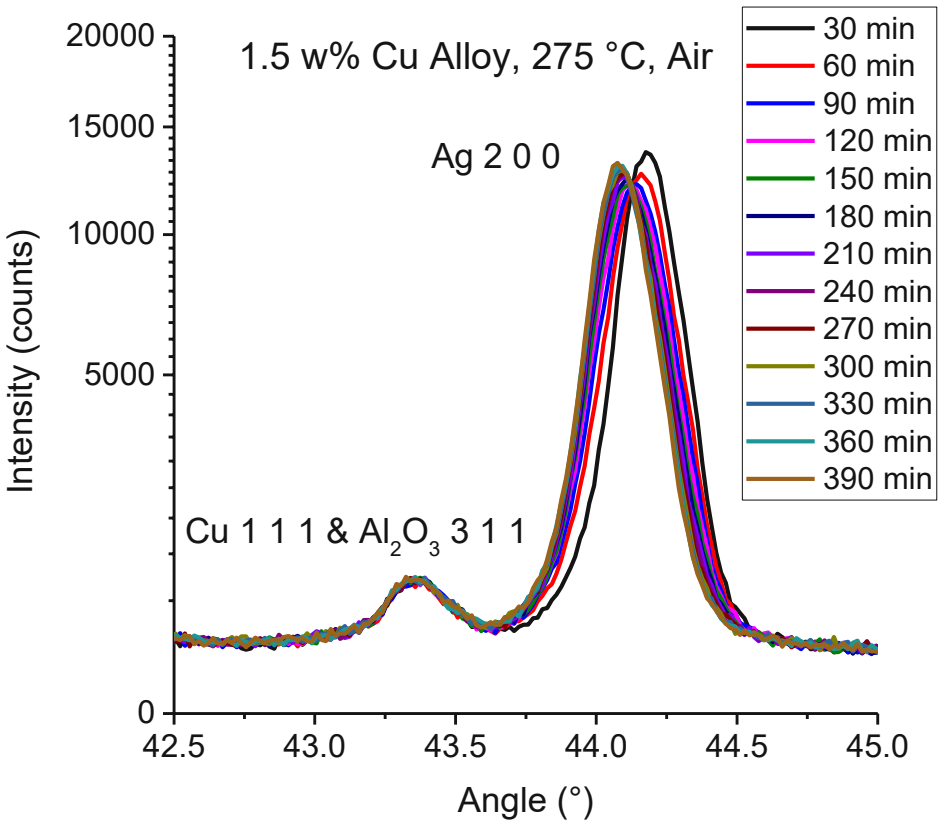

Figure 64: Segregation observed in the 1.5 w% copper sample prepared with an alumina standard and corroded with air

The Rietveld refinement of these measurement series, as well as the one for the 10 w% Cu alloy additionally corroded with brine spray, which is not pictured here separately, yielded precise lattice parameters for the silver phase in the alloy. These refined lattice parameters are drawn in Figure 65 against the reaction time. The lattice parameter of pure silver measured at 275 °C is included as well.

Considering the second 10 w% copper alloy corroded with air, which is drawn as blue triangles in Figure 65, it seems that during oxygen induced segregation the lattice parameter of silver continuously shifts towards a limit and doesn't shift further after reaching it. Vegard's law assumes this limit to be the lattice parameter of pure silver. However, this is not observed. Instead, this limit is above the lattice parameter of pure silver.

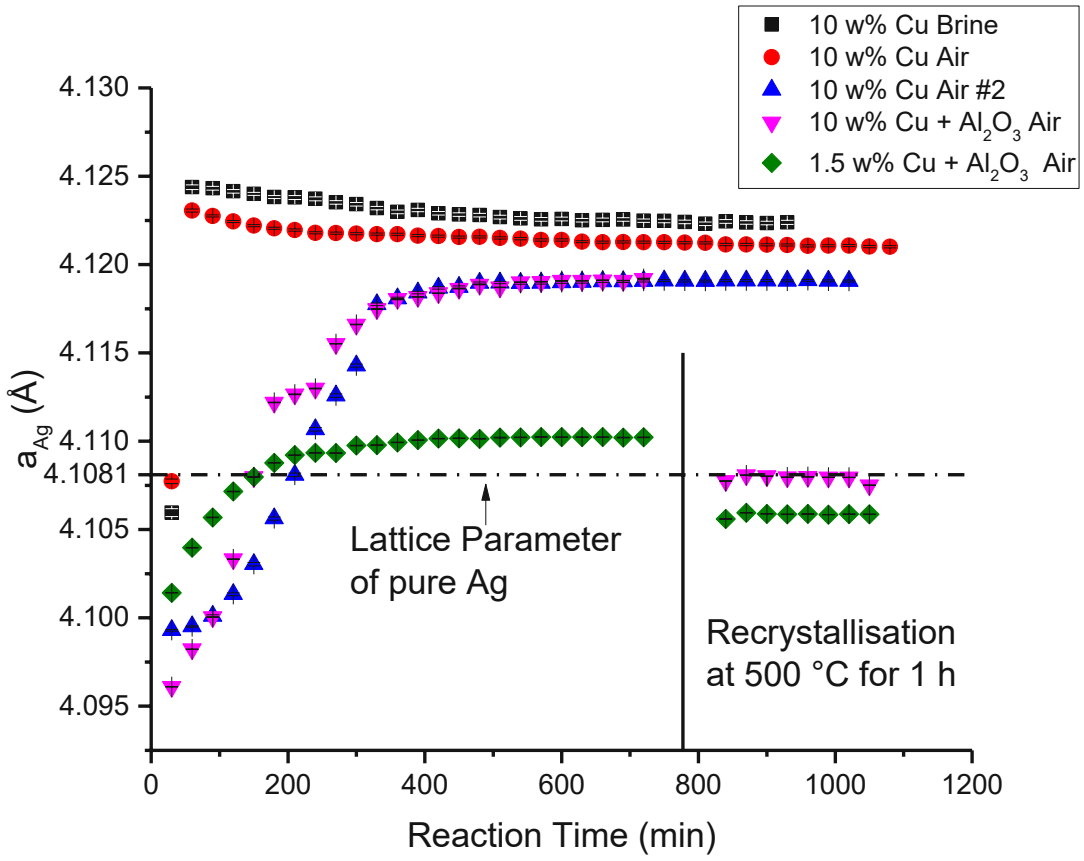

Figure 65: Refined lattice parameters of silver measured at 275 °C against the reaction time of all alloys containing copper that could be refined to a high precision.

Comparing this series to the same alloy but including the internal standard, which is drawn as pink upside-sown triangles in Figure 65, the lattice parameter grows to the same limit. There are differences between the refined parameters in the first 350 minutes of the reaction. These can be explained by the refinement process itself, where the patterns are difficult to refine effectively during this part of the reaction, because the reflections are very broad and lopsided. This influences the determined peak position, and as a result the refined lattice parameter. In this sample a recrystallisation at 500 °C for 60 minutes was performed, which is drawn as a line in Figure 65. After recrystallising the lattice parameter reset to the value of pure silver, which is drawn as a horizontal line in the figure.

On the other hand, the first 10 w% Cu alloys depicted as black squares and red circles, behaved very differently. These series shifted to lattice parameters even larger than what is observed in the other 10 w% copper samples in the first 60 minutes of the reaction. After reaching this maximum, the lattice parameter slowly shrinks. It could not be determined in these experiments if this shrinkage reaches a limit. This process was not done after 18 hours when the measurement of the sample corroded with air was stopped. Why these samples behaved so differently when compared with the same precursor

mixture after homogenisation could not be determined either. More research is required to reach a conclusive explanation.

Finally, the alloy with 1.5 w% copper segregated slowly towards a limit as well. However, this limit is much lower than the one observed with 10 w% copper alloys. In this series the lattice of the segregated species also expanded to be larger than the lattice of pure silver. After the recrystallisation step the lattice parameter reset to a value below the lattice parameter of pure silver. This implies remaining copper in the silver lattice.

7 Summary

To investigate the corrosion phenomena observed on the Vienna Genesis, in-situ powder X-ray diffraction experiments were carried out. To perform these measurements, crystalline silver-copper alloy samples with specific copper contents were required. The alloys were prepared using an in-situ reduction method of an oxide-based precursor mixture. They fulfil the requirements for XRD measurements and offer the possibility of adjusting the composition and adding an internal standard, as well as other impurities of interest.

The morphology of the samples prepared using this route was measured using scanning electron microscopy. This analysis showed that the prepared metal is very porous and has a large surface area. The addition of an internal alumina standard changes the morphology considerably, even if the differences are not immediately obvious from the PXRD patterns.

No silver corrosion products were observed for the described corrosion investigation. Other impurities or corrosive agents need to be investigated to explain the corrosion phenomena observed on the original parchment and artificial samples.

The in-situ X-ray diffraction experiments were analysed using Rietveld refinement methods to gain precise information about the lattice parameter of the silver phase. Experiments using pure silver metal exhibit the lattice parameters documented in literature. Alloying with either 10 w% and 1.5 w% copper lowers the observed lattice parameter, as predicted by Vegard's law.

Silver-copper alloys exhibit a phenomenon known as oxygen induced segregation if treated with oxygen at temperatures above ~200 °C [7]. During this process copper leaves the solid solution in silver and diffuses to the surface, where it reacts with oxygen from the atmosphere to form copper(1)- and copper(2) oxides. This is observable without instrumental equipment in samples treated at above 200 °C because the colour of these samples was darker compared to the samples treated at a lower temperature. This darkening of the metal can be explained by copper located on the surface continuing to react with ambient oxygen even after the experiment concluded to form the aforementioned copper oxides. When this process happens the lattice parameter of the segregated silver species becomes larger than the lattice parameter observed in pure silver. This reaction can be measured with in-situ PXRD methods, where a peak shift of the silver reflections is observable. The characteristics of this shift are similar to those of a phase transition in the X-ray diffraction pattern. Recrystallisation resets the lattice to the expected value of the lattice parameter of pure silver. How much the lattice parameter increases above the predicted value of the lattice parameter of pure silver seems to be dependent on the copper content. In this study the lattice parameter of the segregated silver phase increased much more for 10 w% copper alloys when compared with a 1.5 w% copper alloy.

The oxygen content of the segregated 10 w% copper alloy was measured using thermal decomposition of the alloy in a graphite crucible and detecting the formed CO/CO_2. This analysis showed that the oxygen content of the segregated sample is higher than what would be expected when assuming that the copper oxidised completely to copper(2) oxide. This implies that additional oxygen is bound somewhere in the structure, either on lattice sites or as interstitials. This assumption is supported by the change of the lattice parameter observed during the recrystallisation. Silver oxides are unstable at elevated temperatures, which then decompose into pure silver and oxygen gas. By heating the sample to the recrystallisation temperature of 500 °C the silver(1) oxide decomposes completely to form pure silver metal. However, silver(1) oxide is known to decompose at much lower temperatures than those used in these experiments [8]. More research is needed to validate or disprove this assumption. A conclusive explanation of this process could not be found in this thesis.

8 Conclusion

A method to prepare a crystalline silver-copper alloy powder with adjustable composition was developed. Alloys prepared following this method can be used for in-situ X-ray diffraction experiments. The alloy was calibrated for non-ambient conditions and corrosion experiments in these conditions were performed.

The corrosion of these alloys in the applied conditions did not produce silver corrosion products. Only copper corroded to form oxides and in some cases chlorides. No corrosion similar to the corrosion observed on the Vienna Genesis was found.

Oxygen induced segregation of silver-copper alloys was observed at temperatures above 200 °C. This led to copper leaving the solid solution in silver and diffusing to the surface, where it reacted with oxygen. This is visually apparent in samples treated above 200 °C, which darkened due to copper oxides on the surface. It is also visible in the X-ray diffraction data, where the silver diffractions shift and copper diffractions shrink.

By refining the in-situ data using semi-automated Rietveld refinement, it was found that the segregation induces changes in the crystal structure, with the lattice parameter a of the silver cell increasing to significantly higher values than observed with pure silver metal. Recrystallisation resets the lattice to its expected size and the enlargement of the lattice is dependent on the copper content.

Further research must be performed to fully explain the process happening in the crystal structure of the alloy.

9 Outlook

9.1 Reproducing Corrosion Phenomena Observed on the Vienna Genesis

Now that a sample preparation route has been developed and tested extensively using pure metals, this method could be used to investigate the corrosion phenomena further. By introducing impurities into the precursor mixture changes in these phenomena might be observed. Promising candidates are $CaCO_3$, $NaNO_3$, KNO_3 and acetate, among others.

Furthermore, the solution of sea salt in water used for this experiment was not representative of "real" brine and could be replaced with synthetic brine or brackish water prepared following a norm like DIN 50905. The brine could also be replaced altogether with another corrosive agent. Silver is famously susceptible to tarnish from sulfide compounds, which could also be introduced through the gas stream. Alternatively, the influence of nitrous oxides from the gas stream could also be investigated using this route.

Another important parameter that needs to be adjusted is the reaction temperature. Most of the measurements in this thesis were performed at 275 °C, which is a temperature where high temperature corrosion is the main corrosion effect observed. This temperature was chosen to investigate the observed peak shift, since it was at the time assumed to be related to the corrosion. However, the Vienna Genesis was stored at room temperature and therefore a different corrosion process seems to be relevant. Using the same setup at a lower temperature might already produce different corrosion products.

9.2 Analysis of the segregated silver species

To analyse the segregation process further, better XRD equipment is required. Rietveld refinement offers many parameters that could be refined to explain the segregation process, as well as the structure of the segregated silver species. However, to refine these parameters higher data quality is necessary, which cannot be acquired effectively with the available equipment. Synchrotron measurements might offer the data quality necessary to achieve this. However, aquiring Synchrotron data is unfortunately outside the scope if this master thesis.

Besides this, there are other experiments that could be done to investigate the segregation further. A pure single phase silver alloy could not be prepared effectively. With further experimentation this might be achieved and differences compared to the two-phase alloy might be observed. Higher copper contents might also be attempted, for example in experiments at the other end of the Ag-Cu phase diagram.

Another line of research following these results could be the investigation into preventing the shift from occurring. The increased lattice parameter is likely to influence the mechanical properties of this alloy. Preventing it from occurring therefore might improve the strength and stability of the alloy. This could offer a path to developing new industrial applications of these alloys as solders or conductors, where oxygen induced segregation currently limits the applications of Ag-Cu alloys at elevated temperatures in the presence of oxygen.

10 List of Figures

Figure 1: Scan of the original parchment. Folio 20, page 40, which suffered heavy corrosion damage from the silver ink. [1] 14
Figure 2: Mounted artificial parchment samples after the artificial ageing process. Ordered from left to right in B, C, D in two columns, starting with ST10 in the top left. Every sample was prepared twice. Samples of series C detached during ageing. [1] 16
Figure 3: XRD data of the ST10B sample with identified phases 17
Figure 4: Phase diagram of the Silver-Copper-System. [3] 18
Figure 5: Lattice parameter a of Silver and Copper in a solid solution at different composition compared to Vegard's law 20
Figure 6: Spectrum of X-ray radiation produced in a classic X-ray tube. Source: http://ruby.colorado.edu/~smyth/G30105.html Obtained: 26.7.21 21
Figure 7: Picture of the used XRD setup using the parallel beam mirror 27
Figure 8: Schematic drawing of the non-ambient setup used. 28
Figure 9: High pressure bubbler system used to produce brine spray 29
Figure 10: Empty sample holder for the XRK 900 reaction chamber. 30
Figure 11: Temperature profile of the reduction step in the alloy preparation route 31
Figure 12: Sample holder with Ag_2O + CuO precursor mixture before (left) and after (right) the corrosion experiment. 32
Figure 13: Non-ambient temperature profile of the corrosion measurements described in chapter 4.5.3 33
Figure 14: Corroded Samples of the Temperature Variation series prepared using synthesized Ag_2O and commercial CuO. Corroded using pressurized air and brine. Temperatures start with 25 °C on the left and increase in 50 °C steps. Picture taken 19 months after the original experiment. 36
Figure 15: Corroded Samples of the 10wCu series prepared using commercial Ag2O and CuO. Corroded using pressurized air only (left; 10wCu_Air) and pressurized air and brine (right; 10wCu_NaCl). Picture taken 7 months after the original experiment. 37
Figure 16: Corroded samples of the 10wCu+Al_2O_3 series. One sample was measured under argon as a blind (left) and one corroded with air (right). 38
Figure 17: Corroded sample for the 10wCu_Long series. Picture taken 6 months after the original experiment. 39
Figure 18: Corroded sample 1.5wCu+Al_2O_3_Air 40
Figure 19: Quanta FEG 250 Scanning Electron Microscope 41
Figure 20: SEM sample holder loaded with both samples. Right: pure silver, left: silver + alumina 41
Figure 21: Settings of the "Smart-Batch" used for the semi-automation of Rietveld Refinement 44

Figure 22: XRD-pattern of the prepared silver oxide mixture with matched phases 48
Figure 23: Sample Fit of the calibration of lattice parameters of silver metal with alumina, taken at 225 °C with a GOF of 1.24 49
Figure 24: Refined lattice parameter of pure silver metal against the temperature with a linear fit .. 50
Figure 25: Refined lattice parameter of pure copper metal against the temperature with a linear fit 50
Figure 26: SEM Image of pure Silver directly after the reduction step at 150x magnification. 52
Figure 27: SEM image of pure silver directly after the reduction step at 600x magnification 53
Figure 28: SEM image of pure silver directly after the reduction step at 5000x magnification, centred at a bigger piece. 53
Figure 29: SEM image of pure silver directly after the reduction step at 20000x magnification, centred on a bigger piece. 54
Figure 30: SEM image of pure silver directly after the reduction step at 80000x magnification, centred on a bigger piece. 55
Figure 31: SEM image of pure silver directly after the reduction step at 80000x magnification, centred on a porous area..... 55
Figure 32: SEM image of pure silver directly after the reduction step at 80000x magnification, centred on a porous area..... 56
Figure 33: SEM image of pure silver directly after the reduction step at 320000x magnification, centred on a porous area..... 57
Figure 34: SEM image of pure silver with added alumina, 10 days after the corrosion, at 20000x magnification..... 58
Figure 35: SEM image of pure silver with added alumina, 10 days after the corrosion, at 40000x magnification..... 59
Figure 36: Phase analysis of the temperature variation series after 17 hours or corrosion at 25 °C between 25 and 46 °2θ 61
Figure 37: Phase analysis of the temperature variation series after 17 hours of corrosion at 25 °C between 45 and 75 °2θ 61
Figure 38: Phase analysis of the temperature variation series after 17.5 hours of corrosion at 275 °C between 25 and 46 °2θ. 62
Figure 39: Phase analysis of the temperature variation series after 17.5 hours of corrosion at 275 °C between 45 and 75 °2θ 62
Figure 40: Refined XRD data of the 10wCu_Air corrosion series at the start of corrosion..... 65
Figure 41: Refined XRD data of the 10wCu_Air series after 18 hours of corrosion 65
Figure 42: Refined XRD data of the 10wCu_Air series after 9 hours of corrosion 66
Figure 43: Refined XRD data of the 10wCu_NaCl series at the start of the corrosion..... 67

Figure 44: Refined XRD data of the 10wCu_NaCl series after 15 hours of corrosion 67
Figure 45: Refined XRD data of the 10wCu_NaCl series after 4.5 hours corrosion 68
Figure 46: Refined XRD data of the 10wCu_LECO series at the start of the corrosion 70
Figure 47: Refined XRD data of the 10wCu_LECO series after 17 hours of corrosion 70
Figure 48: Refined XRD data of the 10wCu_LECO series after 9.5 hours of corrosion 71
Figure 49: Refined XRD data of the 10wCuAl_2O_3_Air series before the corrosion, measured under hydrogen 74
Figure 50: Refined XRD data of the 10wCuAl_2O_3_Air series after 12 h of corrosion 74
Figure 51: Refined XRD data of the 10wCuAl_2O_3_Air series after the recrystallisation at 500 °C for 1 hour 75
Figure 52: Refined XRD data of the 10wCuAl_2O_3_Blind series before the corrosion, measured at 275 °C under argon 76
Figure 53: Refined XRD data of the 10wCuAl_2O_3_Blind after 12 hours of corrosion, measured at 275 °C under argon 77
Figure 54: Refined XRD data of the 10wCuAl_2O_3_Blind after recrystallisation at 500 °C for 1 hour, measured at 275 °C under argon 78
Figure 55: Overview of the 10wCu_Long series, measured at 275 °C 79
Figure 56: Zoomed area of the10wCu_Long series depicted in Figure 55. 79
Figure 57: Refined XRD data of the 1.5wCuAl_2O_3_Air series at the start of corrosion 81
Figure 58: Refined XRD data of the 1.5wCuAl_2O_3_Air series after 12 hours of corrosion 81
Figure 59: Refined XRD data of the 1.5wCuAl_2O_3_Air series after recrystallisation at 500 °C for 1 hour 82
Figure 60: Peak shift observed in the Temperature Variation Series at 275 °C in the first 300 minutes between 42.5 and 45.0 °θ 83
Figure 61: Segregation observed in the 10wCu_Air series prepared using clean precursors and corroded with air 84
Figure 62: Segregation observed in the 10wCu_LECO series prepared using clean precursors and corroded with air 85
Figure 63: Segregation observed in the 10wCuAl_2O_3 series prepared with an alumina standard and corroded with air 86
Figure 64: Segregation observed in the 1.5 w% copper sample prepared with an alumina standard and corroded with air 87
Figure 65: Refined lattice parameters of silver measured at 275 °C against the reaction time of all alloys containing copper that could be refined to a high precision. 88

11 Table of Tables

Table 1: Ingredients of the silver inks prepared following historic recipes. 15
Table 2: Nomenclature for the treatment applied before the ageing process. 15
Table 3: Phases present in artificially aged ink on parchment samples 17
Table 4: Overview of measured samples with the composition, measurement parameters and corrosive agents 34
Table 5: List of patterns matched from the ICCD PDF-4+ database 45
Table 6: Observed peak list of the used silver reference pattern 04-001-2617 [21] 45
Table 7: Observed peak list of the used copper reference pattern 00-004-0836 [22] 46
Table 8: Observed peak list of the used copper (2) oxide reference pattern 00-045-0937 [23] 46
Table 9: Observed peak list of the used copper (1) oxide reference pattern 04-007-9767 [24] 46
Table 10: Observed peak list of the used alumina reference pattern 04-007-1400 [25] 47
Table 11: Refined phases for the calibration of the lattice parameters of silver and copper at non-ambient temperatures 49
Table 12: Identified phases in the corrosion experiment at 25 °C of the temperature variation series 60
Table 13: Identified phases in the corrosion experiment at 275 °C of the temperature variation series 61
Table 14: Refined phases of the 10wCu_Air series 66
Table 15: Refined phases of the 10wCu_NaCl series 68
Table 16: Refined Phases of the 10wCu_LECO series 69
Table 17: Results of the oxygen content analysis of the 10 w% copper alloy 72
Table 18: Theoretical composition a 10 w% Cu silver-copper alloy, after the total corrosion of copper metal to copper(2) oxide CuO with silver remaining metallic. 72
Table 19: Refined Phases of the 10wCuAl_2O_3_Air series 73
Table 20: Refined phases for the 10wCu+Al2O3_Blind series 76
Table 21: Refined phases of the 1,5wCuAl_2O_3_Air corrosion series 80

12 References

1. Hofmann, C., *The Vienna Genesis: Material analysis and conservation of a Late Antique illuminated manuscript on purple parchment*. 2020, Vienna: Böhlau Verlag. 348.
2. Malissa, A., *Vorstudien zur Konservierung der Wiener Genesis: Materialanalytische Untersuchungen von Pergament, Tinte und Miniaturmalereien im direkten Vergleich mit thermisch gealterten Pergament- und Silbertintenproben.* Diplomarbeit, 2017, TU Wien.
3. Subramanian, P.R. and J.H. Perepezko, *The Ag-Cu (Silver-Copper) System.* Journal of Phase Equilibria, 1993. **14**(1).
4. Vegard, L., *Die Konstitution der Mischkristalle und die Raumfüllung der Atome.* Zeitschrift für Physik, 1921. **5**(1): p. 17-26.
5. Friedel, J., *LX. Deviations from Vegard's law.* The London, Edinburgh, and Dublin Philosophical Magazine and Journal of Science, 1955. **46**(376): p. 514-516.
6. Linde, R.K., *Lattice Parameters of Metastable Silver-Copper Alloys.* Journal of Applied Physics, 1966. **37**(2): p. 934-934.
7. Kangas, T., et al., *Oxygen induced segregation of copper to Ag/Cu(100) surface.* Surface Science, 2006. **600**(18): p. 4103-4107.
8. Herley, P.J. and E.G. Prout, *The Thermal Decomposition of Silver Oxide.* Journal of the American Chemical Society, 2002. **82**(7): p. 1540-1543.
9. Liu, Y.-c., et al., *Reactive wafer bonding with nanoscale Ag/Cu multilayers.* Scripta Materialia, 2020. **184**: p. 1-5.
10. Anzböck, C., *Röntgenographische Spannungsanalyse an ZRO2 Basierten Elektroden für Metallgestützte Festoxidbrenstoffzellen.* Diplomarbeit, in *X-Ray Center*. 2018, TU Wien: Vienna.
11. Cox, D., *The Rietveld method. (IUCr Monograph on Crystallography, No. 5) edited by R. A. Young.* Journal of Applied Crystallography, 1994. **27**(3): p. 440-441.
12. Rietveld, H., *Line profiles of neutron powder-diffraction peaks for structure refinement.* Acta Crystallographica, 1967. **22**(1): p. 151-152.
13. Degen, T., et al., *The HighScore suite.* Powder Diffraction, 2014. **29**(S2): p. S13-S18.
14. Sonneveld, E.J. and J.W. Visser, *Automatic Collection of Powder Data from Photographs.* J. Appl. Cryst., 1974. **8**.
15. Caglioti, G., A. Paoletti, and F.P. Ricci, *Choice of Collimators for a Crystal Spectrometer for Neutron Diffraction.* Nuclear Instruments, 1958. **3**: p. 223 - 228.
16. PANalytical. *Bragg-Brentano^{HD}*. 3.8.21; Available from: https://www.pharmaceutical-business-review.com/wp-content/uploads/2018/07/763c9616-29f0-4b66-b23f-4a245e694645.pdf.
17. Gilmore, C.J., J.A. Kaduk, and H. Schenk, *International Tables for Crystallography*. Vol. H. 2019.
18. *SRM 676a - Alumina Powder (Quantitative Analysis Powder Diffraction Standard) Certificate*. 3.8.21; Available from: https://www-s.nist.gov/srmors/view_detail.cfm?srm=676A.
19. Panalytical, M., *HighScore Plus Help System Version 4.9*. 2020.
20. Kabekkodu, S.N., J. Faber, and T. Fawcett, *New Powder Diffraction File (PDF-4) in relational database format: advantages and data-mining capabilities.* Acta Crystallographica Section B, 2002. **58**(3 Part 1): p. 333-337.
21. Ellner, M., K. Kolatschek, and B. Predel, *On the partial atomic volume and the partial molar enthalpy of aluminium in some phases with Cu and Cu3Au structures.* Journal of the Less Common Metals, 1991. **170**(1): p. 171-184.
22. Swanson, H. and E. Tatge, *Standard X-ray Diffraction Powder Patterns.* National Bureau of Standards, 1953(539).
23. Brese, N.E., et al., *Low-temperature structures of CuO and AgO and their relationships to those of MgO and PdO.* Journal of Solid State Chemistry, 1990. **89**(1): p. 184-190.
24. Kirfel, A. and K. Eichhorn, *Accurate structure analysis with synchrotron radiation. The electron density in Al2O3 and Cu2O.* Acta Crystallographica Section A, 1990. **46**(4): p. 271-284.

25. Sawada, H., *Residual electron density study of α-aluminum oxide through refinement of experimental atomic scattering factors.* Materials Research Bulletin, 1994. **29**(2): p. 127-133.
26. Merck KGaA, *Certificate on Analysis Ag2O, Lot MKCD6079*. 11.8.21; Available from: https://www.sigmaaldrich.com/AT/en/product/aldrich/226831?context=product.
27. NIST. *Reference Tables*. 4.8.21; Available from: https://www.nist.gov/ncnr/sample-environment/sample-mounting/reference-tables.